FABRICATION AND CHARACTER IZATION OF SPECTRALLY SELECTIVE SOLAR ABSORBER COPPER OXIDE (CuO) NANOCOATINGS FOR PHOTOTHERMAL APPLICATION

By

GIDAY GEBREGZIABHER WELEGERGS

A thesis submitted in a partial fulfilment of the requirements for the degree of

Doctor of Philosophy

in the

DEPARTMENT OF CHEMISTRY

at

UNIVERSITY OF SOUTH AFRICA

Supervisors: -

1. **Professor Malik Maaza**: UNESCO-UNISA Africa Chair in Nano-science and Nano-technology College of Graduate Studies, UNISA, Muckleneuk Ridge, P.O. Box 392, Pretoria, South Africa

2. **Professor Simiso Dube**: University of south Africa, Department of chemistry, P.O. Box 392, Florida compus, South Africa.

3. **Professor Zebib Yenus**: University of Adigrat, Department of physics, P.O.Box 50, Adigrat, Ethiopia.
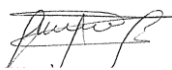
Nov, 2022

DECLARATION

Student number: 65104188

Degree: PhD in Chemistry

I declare that

"FABRICATION AND CHARACTERIZATION OF SPECTRALLY SOLAR SELECTIVE ABSORBER COPPER OXIDE NANOCOATINGS FOR PHOTOTHERMAL APPLICATION"

is my own work, and I confirm that all the sources used have been indicated by a complete references. I further declare that I have acknowledged the code of ethical conduct of the University of south Africa (UNISA)

<u>30/11/2022</u>

Giday Gebregziabher Welegergs   Date

DEDICATION

I would like to dedicate this PhD research work to my late father (**Gebregziabher Welegergs**).

Father your ambition is achieved and I thought you are alive.

ACKNOWLEDGEMENTS

ABSTRACT

Solar-to-thermal energy is considered to be the most direct way of converting solar radiation into usable forms of energy for a wide range of applications, including seawater desalination, heating water, photocatalysis, space heating and cooling, thermophotovoltaics etc. Spectrally solar selective absorber (SSSA) surfaces are the major components in photothermal energy conversions and ideally exhibits a high solar absorptance ($\alpha \geq 0.90$) in the wavelength rage ($300 \leq \lambda \leq 2500nm$) and low emissivity ($\varepsilon \leq 0.10$) in the IR wavelength range ($\lambda > 2500nm$). Copper oxide (CuO, tenorite) is a transitional metal oxide from two elements copper (Cu, ($[Ar]4s^{1}3d^{10}$)), and oxygen (O, $[He]2s^{2}2p^{4}$). The Cu ions are coordinated by four oxygen ions in a monoclinic phase of CuO crystals. Basically, CuO is a p-type semiconductor due to Cu vacancies, and interstitial oxygen within the structure, and it has narrow band gap values of 1.2-1.9 eV that allow it to have a high solar absorptivity in the solar region.

In this investigation, spectrally selective single-layered CuO and Ag@CuO nanocermet coatings deposited on stainless steel (SS) substrate are introduced. The SS has been widely used as a substrate for various range applications due to its thermal and chemical stability, environmental friendliness, and good optical properties. CuO and its plasmonic nanocermet coatings were successfully demonstrated using facile and reproducible green synthesis, electrodeposition, and sputtering methods aimed at high absorptance(α), and low emissivity (ε) values for solar-to-thermal conversion application. In green synthesis, spectrally selective single-layered CuO nanocoatings and Ag@CuO nanocermet coatings were synthesized from copper nitrate trihydrate ($Cu(NO_3)_2.3H_2O$) and silver nitrate ($AgNO_3$) salt precursors using plant extract (*cactus pear*) as stabilizing and reducing agent and then deposited on SS substrates using spin coater at 700, 800, 900, and 1000 rpm. In electrodeposition, the Cu thin films were reduced on the electrode or SS substrate surface from $Cu(NO_3)_2.3H_2O$ electrolyte at 15, 20 and 25 min deposition time at room temperature and then annealed in a furnace, results in the growth of nanostructured CuO. Conversely, the Cu films were deposited using RF sputtering on SS substrate at different thicknesses and then oxidized in alkaline solution at room temperature. The morphological, structural, compositional, chemical states and thickness of the coatings were analysed using scanning electron microscopy (SEM), Atomic microscopy (AFM), X-ray diffraction (XRD), Energy-dispersive X-ray spectroscopy (EDS), X-ray photometer spectroscopy (XPS), and Rutherford backscattering spectroscopy (RBS). The SEM images confirmed the growth of CuO nanorods, nanowalls, and nanoplates (NPs)

from green synthesis, electrodeposition, and sputtering methods, respectively. The Ag@CuO nanocermet coatings also showed a better dispersibility of white plasmonic Ag NPs in the nanorods of CuO matrix. The XRD patterns revealed a well-crystalline nature of the monoclinic phase of CuO, and face centered cubic of Ag metal, the incorporated Ag NPs did not affect the monoclinic phase of CuO. The EDS clearly confirms compositional purity of the coatings. The grain size, surface roughness and crystalline size of the coatings depend on the thickness of the coatings, and were found to increase with coating thickness. The content of the elements in the coatings and the thicknesses of the coatings were determined by RBS. The thickness of the coatings is calculated to be 1416×10^{15} atoms/cm^2 (298.2 nm), 1296×10^{15} atoms/cm^2 (272.8 nm), 1153×10^{15} atoms/cm^2 (242.7 nm) and 998×10^{15} atoms/cm^2 (210.2 nm) at 700, 800, 900, and 1000 rpm, respectively. Raman spectra showed peaks attributed to Raman active (A_g+2B_g) modes which are characteristics of Cu-O stretching vibrations and XPS spectra revealed peaks of Cu2p, O1s, and Ag3d core levels; These peaks are typical characteristics of Cu (II), O(II) and Ag(I), respectively.

The optical properties of CuO nanocoatings, and Ag@CuO nanocermet coatings was characterized as spectrally selective absorbers using UV-Vis-NIR, and IR spectrometers. The vital solar selectivity parameters of solar absorptivity (α) and emittance (ε) were evaluated, respectively from UV-Vis-NIR and IR spectral reflectance in a wavelength range of 300-2500, and 2500-20000 nm. The optimized coatings exhibit a solar absorptance (α = 0.93, 0.92 and 0.97), and thermal emissivity of (ε = 0.23, 0.28, and 0.40) from green synthesis, electrodeposition, and sputtering methods, respectively. The incorporated Ag NPs improved the intrinsic absorption and reflectivity properties of green synthesized CuO nanocoatings from (α/ε = 0.90/0.31) to (α/ε = 0.93/0.23) at 700 rpm. This is due to the concentrated free electrons which contribute a plasma resonance frequency and its particle sizes are comparable to or smaller than the wavelength of incident light. The optical bandgap energy (*Eg*) of CuO coatings was estimated from reflectance spectra using Kubelka-Munk (K-M) function and found in the range of 1.65-1.27 eV. The lower band gap values are attributed to higher solar absorption above the band gap energy. Hence, the CuO nanocoatings and Ag@CuO nanocermet coatings are capable of a potential candidate(s) for SSSA surfaces in solar to thermal energy conversion systems.

i. LIST OF PUBLISHED, AND UNDER REVIEW ARTICLES

[1] **G.G.Welegergs**, H.G.Gebretnisae, M.G.Tsegay, T.G. Kebede, A. Bhardwaj, S. Mathur, Z.Y.Nuru, S.Dube, M.Maaza, Electrodeposition of nanostructured copper oxide (CuO) coatings as spectrally solar selective absorber: Structural, optical and electrical properties, infrared and technology, 133(2023) 104820.

[2] **G.G.Welegergs**, H.G.Gebretnisae, M.G.Tsegay, C.Mtshali, N.Mongwaketsi, Z.Y.Nuru, S. Dube, M.Maaza, Single layered biosynthesised copper Oxide (CuO) nanocoatings as solar selective absorber, Applied sciences, 13(**2023**), 1867-1881.

[3] **G.G.Welegergs**, H.G.Gebretnisae, M.G.Tsegay, T.G. Kebede, A. Bhardwaj, S. Mathur, Z.Y.Nuru, S.Dube, M.Maaza, Spectrally selective single-layered Ag@CuO nanocermet coatings for photothermal Applications: Green synthesis method, Optical materials 135 (**2023**) 113247.

[4] **G.G.Welegergs**, H.G.Gebretnisae, M.G.Tsegay, Z.Y.Nuru, S.Dube, M.Maaza. Thickness dependant morphological, structural, and optical properties of CuO nanocoatings as solar selective absorber, Infrared Physics and Technology, 113(**2021**) 103619.

[5] **G.G.Welegergs**, R Akoba, J Sacky, Z.Y Nuru. Structural, and optical properties of copper oxide (CuO) nanocoatings as solar selective absorber, Material Today proceeding, 36(**2020)** 509-513.

Comments on my contribution

I am responsible for conducting of the experiments, analyzing the experimental results, writing, and submitting of the above PhD dissertation research articles for publication in pear-reviewed journals.

ii. Articles not included in this PhD dissertation

[1] H.G. Gebretinsae, M.g.Tsegay, **G.G Welegergs**, M. Maaza, Z.Y. Nuru**,** Effect of rotational speed on the structural, morphological, and optical properties of biosynthesized Nickel Oxide thin films for selective solar absorber nanocoatings, Energies, *15*(**2022**) 8960.

[2] M.G. Tsegay, H.G. Gebretinsae, **G.G. Welegergs**, M. Maaza and Z. Nuru. Novel green synthesized Cr_2O_3 for selective solar absorber: Investigation of structural, morphological, chemical, and optical properties, Solar Energy, 236(**2022**) 308-319.

[3] **G.G. Welegergs**, N.Numan, S.Dube, Z.Nuru, N. Botha, K. Cloete, Sh. Azizi1, I. Madiba, M.Akbari, R. Morad, M. G.Tsegay, H.G. Gebretinsae, Ch. Mtshali1, Z.Khumalo, F. Ezemal, A. Krief, A.Gibaud, M. Henini, M.P. Seopela, M. Chaker, M. Maaza, Bio-engineered nanostructured CuS via natural Sativum Annilin based sulfurization at room temperature, **Nature scientific report** (Revised)**.**

[4] Nandipha L. Botha, **G.G Welegergs,** Karen J. Cloete, Mahmood Akbari, Razieh Morad, Chester Kotsedi, Nolubabalo Matinisi, Remy Bucher, Malik Maaza, Physical properties of computationally informed phyto-engineered 2-D nanoscaled hydronium jarosite, **Nature scientific report (Revised & Accepted**).

iii. Conference papaers

[5] **G.G. Welegergs,** H. Gebretinsae, N. Matinise, Z.Y. Nuru, M Maaza, Electrochemical properties of green synthesised Zinc Oxide (ZnO) nanoparticles, springer, 5(**2020**) 1-7.

[6] R Akoba, **G.G Welegergs**, M Luleka, J Sackey, Effect of Etchant Concentration on the Optical Properties and Surface Topography of MoO3 Selective Solar Absorber, MRS Advances, 5(**2020**) 133–1143.

[7] RashidahAkoba, **Giday G. Welegergs**, De W.Selwyn, Nagla Numan, Juliet Sackey, Zebib Y.Nuru, Nanostructured black moly surfaces for solar thermal absorbers by wet chemical etching, Materials Today proceedings, 36(**2021**) 251-255.

[8] Henok Gebretinsae, **Giday Welegergs**, N. Matinise, M. Maaza and Z. Y. Nuru, Electrochemical study of Nickel Oxide (NiO) nanoparticles from cactus plant extract, MRS Advances, 5(**2020**), 1095–1102.

LIST OF SYMBOLS, CONSTANTS, AND ABBREVIATION

α	Solar absorptance
ε	Thermal Emittance
λ	Wavelength
h	Plank's constant, 6.626×10^{-34} Js
k	Boltzmann Constant, 1.382×10^{-23} J/k
C	Speed of Light 3.0×10^8 m/s
$R(\lambda)$	Reflectance
$T(\lambda)$	Transmittance
I_b	Intensity of black body radiation
I_s	Intensity of solar irradiance
T	Temperature
AM	Air Mass
ARL	Anti-reflection layer
CB	Conduction Band
CSP	Concentrated Solar power
DMD	Dielectric Metal Dielectric
DC	Direct Current
DC	Direct Current
Eg	Band-gap energy
EQE	External quantum efficiency
ETC	Evacuated tubular Collectors
EDTA	Ethylene Diaminete Triacetic Acid
EDS	Energy Dispersive X-Ray Spectroscopy
EM	Electromagnetic Radiation
FCC	Face centered cubic
FWHM	Full width at half maximum
HTF	Heat Transfer Fluid
FEDs	Field Emission Displays
IR	Fourier-Transform Infrared Spectroscopy

GHG	Green-House Gases
IR	Infrared
LED	Light Emitting Diodes
LIBs	Lithium Ion Batteries
LSPR	Localized Surface Plasmonic resonance
MO	Metal Oxide
NPs	Nanoparticles
OLEDs	Organic Light Emitted Diodes
PTC	Parabolic Trough Collector
PVD	Physical Vapor Deposition
QC	Quantum Confinement
RF	Radio Frequency
RPM	Rotational per minutes
RS	Rotational speed
RT	Room Temperature
TMOs	Transition Metal Oxides
SCCM	Standard cubic centimetres per minute
SEM	Scanning Electron Microscopy
SPPs	Surface Plasmon Polarizations
SS	Stainless-Steel
SSSA	Spectrally selective solar absorbers
UV-Vis-NIR	Ultraviolet-Visible-Near Infrared
VB	Valence-Band
XPS	X-Ray photoelectron spectroscopy
XRD	X-Ray-Diffraction

LIST OF TABLES

LIST OF FIGURES

TABLE CONTENTS

THESIS STRUCTURE

➢ This thesis is divided into **four chapters**. The **first chapter** presents the general concept about solar energy and spectrally solar selective coatings. In addition, the problem and aims of the study will be briefly stated in this chapter.

➢ The **second chapter**: introduces the literature review on solar energy, electromagnetic radiations, mechanism of photothermal conversions, properties of spectrally selective surfaces, solar collectors, introduction to CuO, synthesis approaches, fundamental properties, and applications of CuO.

➢ **Chapter three**: The methodologies for spectral solar selective CuO coatings (or green synthesis, sputtering, and electrodeposition methods), and the main characterization techniques employed are briefly illustrated in this chapter.

➢ **Chapter four**: Result and discussion for the obtained all of CuO nanocoatings and Ag@CuO nanocermet coatings are briefly addressed. In this chapter the morphological, structural, and optical properties of the optimized coatings prepared via green synthesis, electrochemical, and RF sputtering methods are briefly analysed.

CHAPTER ONE

BACKGROUND OF THE STUDY

1.1 Introduction

The progress of human civilization, energy demands and environmental concerns due to greenhouse gases (GHG) have aroused much interest in clean, and sustainable energy sources to replace the non-renewable use of fossil fuel-based energies namely coal, gas, oil, etc. Among the known renewable energies such as wind, biomass, and hydro energy, solar energy is becoming indispensable as it is a source of clean energy, bountiful, inexhaustible, and also considered as a possible solution to the environment pollutions and energy crisis because of its carbon-neutral energy source, and pollution-free nature [1-4]. Solar energy is widely utilized for various potential applications, such as photocatalysis, solar vapour generation, photovoltaic, photothermal and solar-driven energy conversion fields. In comparison to solar-to-thermal conversion, photovoltaic conversion of solar radiation into electricity is a well-proven technology with a low cost. However, due to its high conversion efficiencies and good storage functionality, solar-to-thermal systems are regarded as a very promising route [4-8].

Solar-to-thermal energy conversion is considered as a direct method of harnessing and converting solar radiation into thermal and then to thermophotovoltaics for various potential applications, such as seawater desalination, heating water, refrigeration, industrial processing, power generation etc., [9-11]. Spectrally solar selective absorber (SSSA) surfaces which are the major components in photothermal conversion efficiency, exhibit a high absorptances ($\alpha \geq 0.90$) in solar spectrum wavelength ($300 \leq \lambda \leq 2500$ nm), while retaining low emissivity ($\varepsilon \leq 0.10$) in the IR wavelength ($\lambda \geq 2500$ nm) to enhance the conversion efficiency and they are thermally stable at their operational temperatures. Based on the working temperature, the solar selective absorber (SSA) coatings can be categorized as low (T < 100 ºC), medium (100 ºC < T < 400 ºC), and high (T > 400 ºC) temperature for photothermal applications [12-18]. So far different designs of solar selective coatings, such as intrinsic (e.g, V_2O_5, and Al_2O_3) [19-21], semiconductors (e.g, $Si_{0.8}Ge_{0.2}$, and Cu_2O) [22, 23], metal-dielectric composites (e.g, $W-Al_2O_3$, $Mo-SiO_2$ and $Ni-NiO$) [10, 24, 25], dielectric-metal-dielectric (AlxOy/Pt/AlxOy and $Cr_2O_3/Cr/Cr_2O_3$) [26, 27], multilayers (Al/NbMoN/NbMoON/SiO₂, and WAlN/WAlON/Al_2O_3) [15, 28, 29], and textured surface (e.g, CuO and MoO) [30, 31] have been widely investigated to improve the conversion efficiencies for various potential applications. Among them, semiconductor coatings have been intensively used for

photothermal energy conversion because they have good intrinsic, and/or selectivity properties as well as transparency for photons below their optical bandgap energy but absorb energy above the bandgap [32-35].

Copper oxide (CuO, tenorite) is one of the stable oxide forms of Cu ([Ar]$4s^1 3d^{10}$) metal. In a crystal, CuO has a monoclinic phase structure, and the Cu ion is coordinated by four oxygen ions. CuO with large surface area exhibits superior physical and chemical properties and has been broadly studied because of its practical applications in various fields, such as biology, chemistry, medicine, physics, and electronics [36-38]. Moreover, CuO basically is a p-type semiconductor with narrow band-gap energy of 1.2–1.9 eV that allows to absorb UV-Vis-NIR irradiation effectively and also a good infrared (IR) mirror to suppress the reemission loss in the long wavelength IR region for photothermal. CuO films have been investigated and reported for photothermal energy applications as solar selective absorber (SSA) using different physical and chemical methods [17, 18, 39]. S. Karthick *et.al* [40], demonstrated CuO nanocoating as SSA on Cu substrate using NaOH, and NH_4OH and reported an absorptance of ($\alpha = 0.90$) and emissivity ($\varepsilon = 0.07$). He *et.al* [41] reported Ag@CuO nanocomposite film as novel SSA via step sol-gel and achieved ($\alpha = 0.917$, $\varepsilon = 0.05$). Barshilia *et.al* [42] fabricated CuO thin films on silicon (Si) substrates using reactive sputtering at high temperatures, and reported a high absorptance ($\alpha = 0.95$), and emissivity ($\varepsilon = 0.52$).

Recently, green synthesis method has demonstrated several advantages over the physical and chemical procedures due to its inevitability to develop clean, environmentally friendly, cost-effective, and effective synthesis techniques [43-46]. In this investigation, spectrally selective single-layered CuO nanocoatings and its plasmonic nanocermet (Ag@CuO) coatings were synthesized via green synthesis using plant extract (*cactus pear*), copper nitrate trihydrate ($Cu(NO_3)_2$, and sliver nitrate ($AgNO_3$) salt precursors, and then spin-coated on SS substrates at different rotational speeds (RS). Moreover, CuO nanocoatings are fabricated using facile, cost-effective, and scalability of electrochemical and sputtering deposition techniques for improved SSA surfaces. In the electrochemical method, the copper (Cu) thin films were deposited on the electrode surface or SS substrates from an electrolyte ($Cu(NO_3)_2.3H_2O$) solution using a three-electrode configuration at room temperature and then annealed for CuO formation. Conversely, in the sputtering process, the Cu films were deposited on SS substrates using RF sputtering and then oxidized into CuO in alkaline solution at room temperature. Optical, and non-optical characterization techniques were applied to study the surface morphologies, structural and optical properties of the prepared coatings.

1.2 Problem of the study

Currently, the world relies upon fossil fuel-based materials like coal, gases, oil, petroleum etc, to produce most its energy and meet demands. However, the consumption of fossil fuel-based energy sources is generating green-house gases (GHGs), which are a major factor for global warming. Due to the scarcity of fossil fuel, environmental concerns, increasing the need of clean and sustainable energy, and the growing of global energy crisis driven by the strong economic development, the world shifted towards alternative renewable energy technologies. So far, significant efforts have been devoted to the development of renewable energy technologies, which have led to utilization of solar energy, wind energy, biomass energy, and other renewable energy sources. Of the renewable energy sources, sunlight is abundant, easily accessible, eco-friendly, and considered as a potential solution to energy crisis as well as environmental challenges to propel sustainable development of human society. This reliable, and abundant energy source is harnessed and then converted into usable energy forms by using solar technologies such as photovoltaics and photothermal [1, 2, 47, 48].

The photothermal conversion technology which converts directly solar radiation into thermal (heat), and then to thermophotovoltaic for concentrated solar system (CSP) applications, becomes mature and cost-effective. The solar-to-thermal devices are very promising routes for the low and medium-temperature applications such as domestic water heating at medium temperatures (T ≤ 400 ℃), and strongly depend on electrical and optical properties of the solar collector surfaces to harvest the incident solar radiation [47, 49, 50]. So far, spectrally selective CuO thin films have been achieved by using different coating techniques such as spraying, spin coatings, sol-gel, electrophoretic depositions, chemical oxidation, D.C. magnetron sputtering, and chemical vapour deposition (CVD) on different metallic substrates for photothermal applications. However, these physical and chemical methods may need high energy and produce chemical by-products to the environment [30, 51-57].

Recently, green synthesis of nanomaterials demonstrated to have several advantages over physical and chemical procedures due to being clean, environmentally friendly, cost-effective and utilizing effective synthesis techniques [43, 46]. In this research work, spectrally selective single-layered CuO nanocoatings and Ag@CuO nanocermet coatings were synthesized via green synthesis and then deposited on SS substrates by spin coating. Moreover, CuO nanocoatings aimed at high absorptivity were also fabricated via electrochemical and sputtering deposition techniques on SS substrate because of its

simplicity, low-temperature processing, high quality, and accurate deposition rate, and viability of commercial production [58].

1.3 Aims of the study

➢ The main aim of this research work is to develop an improved spectrally selective single-layered copper oxide (CuO) based nanocoatings using cost-effective, and reproducible methods (i.e green synthesis, electrochemical, and sputtering deposition) aimed at high solar absorptance (α), and low emissivity (ε) values in the solar spectrum and infrared (IR) region as solar selective absorbers, respectively.

1.4 Specific objectives

The following specific objectives were performed to achieve the above aims;

➢ To prepare plant material extracts which are used as chelating, stabilizing and/or reducing agents for synthesis of nanoparticles and nanocomposites.

➢ To synthesis of CuO nanoparticles and Ag@CuO nanocomposites using *plant* extracts, copper nitrate trihydrate ($Cu(NO_3)_2.3H_2O$) and sliver nitrate ($AgNO_3$) salt precursors.

➢ To deposit the green synthesized CuO NPs and Ag/CuO nanocomposites on stainless steel (SS) substrates via spin coater at different rotational speed (RS) of the spin-coater.

➢ To deposit Cu thin films on SS substrates at different deposition time via electrochemical deposition from $Cu(NO_3)_2.3H_2O$ electrolyte-solution at room temperature.

➢ To oxidise the deposited SS/Cu thin film into SS/CuO via thermal oxidation.

➢ To deposit Cu thin films using RF sputtering on SS substrates at room temperature.

➢ To oxidise the deposited SS/Cu thin film into SS/CuO in alkaline solution at room temperature.

➢ To characterise the obtained all coatings using different optical and non-optical characterization techniques.

➢ To analyse the effect of film thickness on the morphological, structural and optical properties of all the coatings.

CHAPTER TWO

LITERATURE REVIEW

2.1 Solar energy

The global energy demands for a clean and sustainable environment and environmental concerns due to greenhouse gases (GHGs) have aroused much interest in renewable sources of energy to replace those non-renewable or fossil fuel-based energy sources like coal, gases, oil, petroleum etc. There is a variety of renewable resources energy including wind energy, solar, hydro, biomass, nuclear, geothermal energy and so on. Of those, solar energy is a bountiful, clean, environmentally friendly, accessible, and carbon-neutral energy source. The total power of solar energy is 3.8×10^{23} MW, out of which 4×10^{14} kW is incident on the earth surface in the form of electromagnetic radiations per day almost 5000 times the current annual energy consumption. Fig. 2.1 illustrates the solar energy distribution in our planet. Even if Africa has large average solar energy distribution compared to other continents, the United States, Germany, Spain, Italy, and Japan are at the forefront of photothermal energy utilization [1, 2, 59, 60].
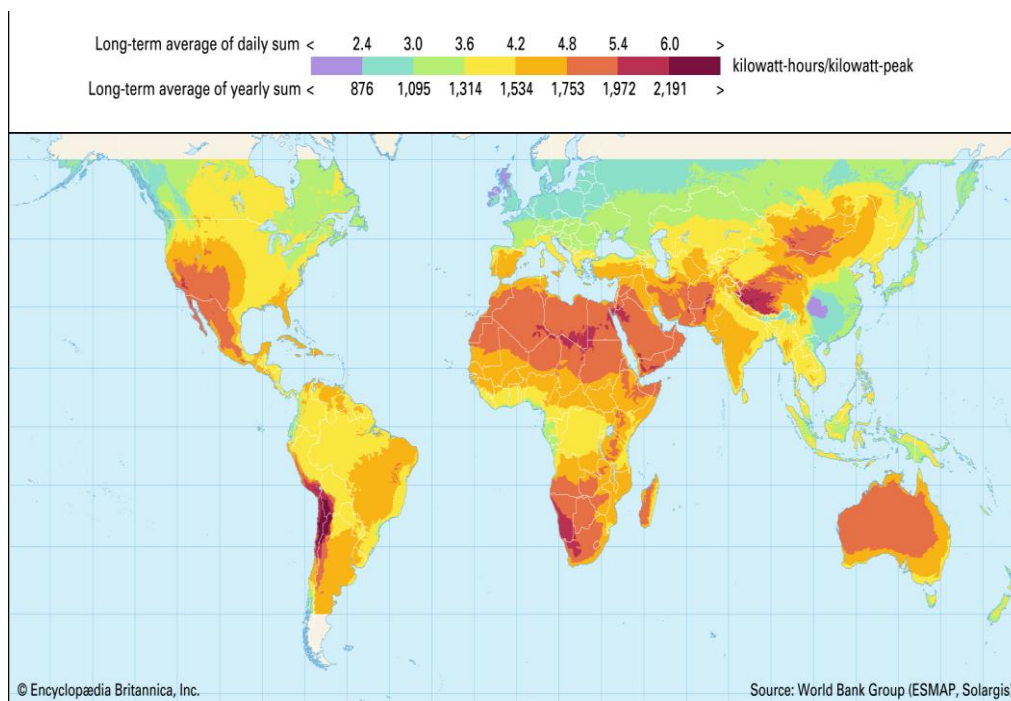
Figure 2.1 Solar energy distribution potential [60].

The incident light can be harnessed using passive and active solar system approaches. Structure, design, and position to use solar energy are the primary characteristics of passive

solar systems. The active solar techniques use mechanical and electrical equipment to utilize the solar energy into usable energy forms, such as thermal or electricity [61, 62]. The versatile solar energy source can be transformed into different types of usable energy forms such as chemical (fuels), electrical and thermal energies by using active systems of photochemical [63], photovoltaic [7] and photothermal [8] processes, respectively. The conversion of the incident light to electricity via photovoltaics is a well-proven technology compared to photothermal conversions. However, solar to thermal conversion process is a promising route to harvest, and convert the sun light into thermal, and then to electricity via thermophotovoltaic systems for concentrating solar power (CSP), and has proven for broad applications such as domestic water heating, and cooking, environmental purification, desalination sea water, space heating, and cooling, industrial processing, catalytic production of fuels and chemicals, and electricity generation [5, 6, 62].

2.1.1 Electromagnetic radiation

In 1865, James Clerk Maxwell projected the theory of electromagnetic and predicted light as electromagnetic radiations which is the cause of magnetic and electric phenomena. Electromagnetic radiation propagates as electrical and magnetic waves and travels in packets of radiant energy called photons. The vibrations of magnetic and electric charges created an electromagnetic wave that have both an electric-field and magnetic-field. In electromagnetic waves, both fields are perpendicular to each other [55, 64]. Electromagnetic radiations are classified according to the wavelengths or frequencies of their oscillations within the electromagnetic spectrum, for example, in order of decreasing wavelength (λ) or increasing frequency from gamma rays (~ 10^{-12} μm/10^{20}Hz) to long radio waves (~10^{10} μm/10^8 Hz) includes, gamma rays, X-rays, ultraviolet (UV), visible-light, IR radiations, micro, and radio waves [55, 64] as shown in Fig.2.1.1.
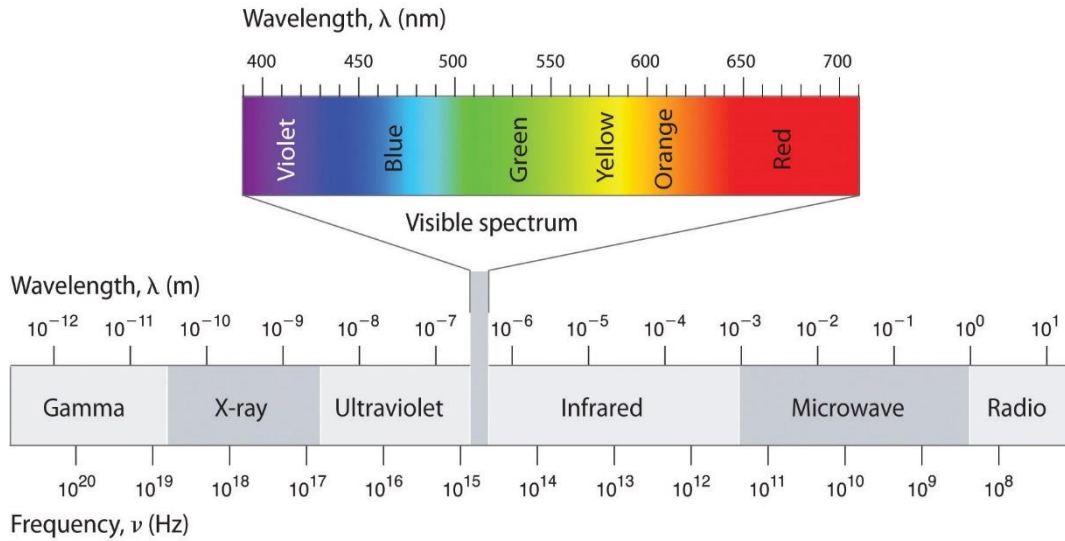
Figure 2.1.1: Electromagnetic spectrum

The electromagnetic radiation emitted by the sun is called solar radiation, and it falls in the ranges of 0.3~2.5μm wavelength, and radiations emitted from absorbers above 200 ℃ temperature spreads in the far IR region which extends in the range of 2.5~50μm wavelengths. The electromagnetic solar and thermal radiations are important for photothermal applications [17].

2.1.1.1 Solar radiation

When sunlight reaches on the absorber surface, some light is reflected and the rest enters into the medium and can be absorbed and/or transmitted. When a surface of a matter is subjected to electromagnetic radiation, absorption, reflection, and transmission phenomena occur as the total radiation shown in Fig.2.1.1.1. Absorption can occur when the energy of an incident light is equal or greater than the bandgap energy of the absorber material [65].
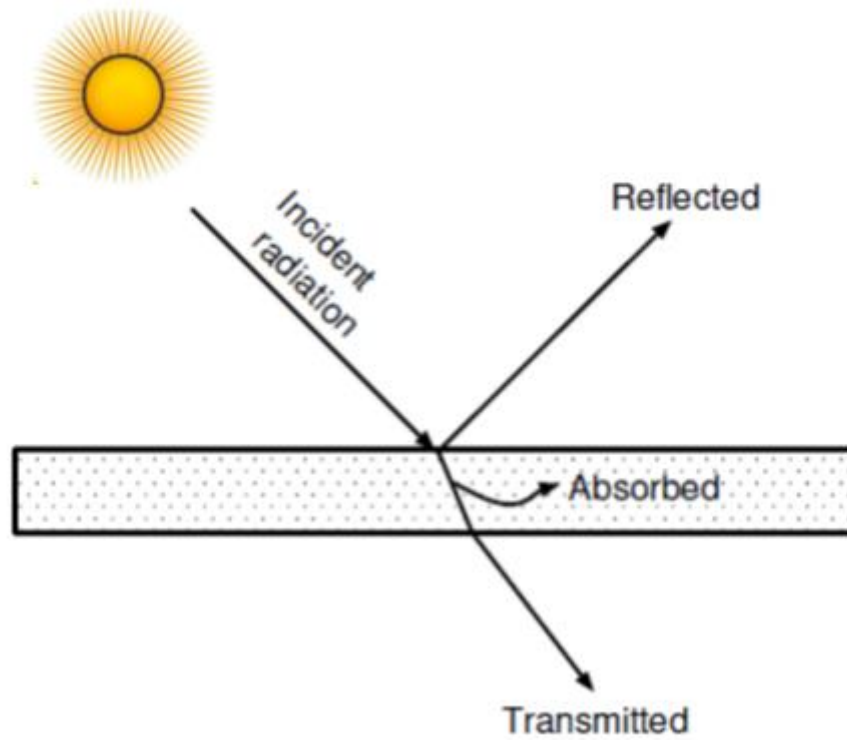
Figure 2.1.1.1: Electromagnetic wave interaction with solar absorber surface

The amount of light reflected from the absorber surface is analysed by the reflectance (R), and it is the ratio of light reflected (I_R) to incident light (I_0). According to energy conservation in Fig.2.1.1.1, the sum of transmission (τ), reflection (R), and absorption (A) of the incident light is equal to unity (1) in a given wavelength, as expressed in eq. (2.1.1.1) [65, 66].

$$\alpha(\lambda) + R(\lambda) + \tau(\lambda) = 1 \qquad (2.1.1.1)$$

For non-transparent absorbers, the τ is zero (τ(λ) = 0), and the total energy is expressed in terms of the absorptance α(λ), and total reflectance, R(λ), as follows;

$$\alpha(\lambda) + R(\lambda) = 1 \qquad (2.1.1.2)$$

$$\alpha(\lambda) = 1 - R(\lambda) \qquad (2.1.1.3)$$

The solar absorptance (α) is one of the parameters that characterizes the performance of the absorber material and is defined as the ratio of the solar radiation absorbed by the absorber to the incident radiation [33, 65].

$$\alpha_{(\lambda,\theta)} = \frac{G_\lambda I_{sol}(\lambda)}{G_\lambda(\lambda)} \qquad (2.1.1.4)$$

where $G_\lambda I_{sol}(\lambda)$ and $G\lambda(\lambda)$ are, respectively the absorbed and incident radiations. Using Eqs. (2.1.1.3) and (2.1.1.4), the solar absorptance (α), represents the ability of the absorber of coating to absorb incident light in the solar spectrum (AM 1.5), and integrating from 0.3–2.5µm wavelengths as follows eq. (2.1.1.5).

$$\alpha(\lambda) = \frac{\int_{0.3\mu m}^{2.5\mu m}(1-R(\lambda))I_{sol}(\lambda)d(\lambda)}{\int_{0.3\mu m}^{2.5\mu m} I_{sol}(\lambda)d\lambda} \qquad (2.1.1.5)$$

where I_{sol} is the density of incident sunlight at AM 1.5 [65, 66].

2.1.1.2 Thermal radiation

The infrared emissivity (ε) is another criteria to determine the performance of solar absorber coatings in the far infrared compared to the ideal blackbody. A perfect blackbody is one that absorb all the electromagnetic radiation falling on the surface of the absorber, no radiation is reflected and appears perfectly black. Therefore, a blackbody is a perfect absorber surface, at the same time a perfect emitter. Planck's radiation law governs blackbody radiations.

$$E_{b\lambda} = \frac{8\pi hc}{\lambda^5 exp\left(\frac{hc}{\lambda KT}-1\right)} \qquad (2.1.1.6)$$

where $E_{b\lambda}$ is the spectral radiance, T is the temperature, h is Planck constant (6.63×10^{-34} Js), c is the speed of light (3.0×10^8 m/s), k is Boltzmann's constant (1.38×10^{-23} J/K) [65, 67]. The total emitted energy by the blackbody at a given temperature can be obtained by integrating Planck's spectrum and proportional to the fourth (4) power of its temperature (T) according to Stephan-Boltzmann law, as expressed in eq. (2.1.1.7).

$$E_b = \int_0^{20} E_{b\lambda}(\lambda,T)\,d\lambda = \sigma T^4 \qquad (2.1.1.7)$$

where σ is Stefan-Boltzmann constant (5.67051×10^{-8} W/m^{2}K^4). The thermal emissivity(ε) of an object in IR region is the ratio of radiation emitted by the heated absorber surface at a temperature (T) to emitted radiations by a blackbody ($E_b\lambda$), and can be expressed as [65, 67, 68].

$$\varepsilon(\lambda, T) = \frac{\varepsilon(\lambda,T)}{\varepsilon I_b(\lambda,T)} \qquad (2.1.1.8)$$

where $\varepsilon(\lambda, T)$, and $\varepsilon I_b(\lambda,T)$ are radiation emitted by the object and by a perfect blackbody, respectively. In thermal equilibrium (i.e, at a constant temperature (T)), for an opaque substance, the spectral thermal emissivity (λ) is equal to the solar absorptance (α) at every wavelength (λ) known as Kirchhoff's Law (see eq. 2.1.1.9).

$$\varepsilon(\lambda,T) = \alpha(\lambda,T) = 1 - R(\lambda,T) \qquad (2.1.1.9)$$

and combining eqs. (2.1.1.8), and (2.1.1.9) the total thermal emissivity at T can be calculated by [65, 66].

$$\varepsilon(\lambda,T) = \frac{\int_{2.5\mu m}^{25\mu m}(1-R(\lambda))I_b(\lambda,T)d(\lambda)}{\int_{2.5\mu m}^{20\mu m} I_b(\lambda,T)d\lambda} \qquad (2.1.1.10)$$

where I_b is emitted radiation by blackbody at a given (λ, T).

The photothermal conversion efficiency (η) of spectrally selective coatings at working temperature (T) can be calculating by combining the solar absorptance (α), and thermal emissivity (ε) using eq.(2.1.1.11).

$$\eta = \alpha - \frac{\varepsilon(T)\sigma(T^4 - T_c^4)}{CI} \qquad (2.1.1.11)$$

where σ is Stefan Boltzmann constant (5.67×10^{-8} Wm^{-2}K^{-4}), C is concentration factors (e.g parabolic C=15 to 40) and I is intensity of solar radiation [67, 69].

2.2 Mechanisms of photothermal conversion

Photothermal conversion is a process of converting the incident solar radiation into heat and then to electricity via thermophotovoltaic technologies. The conversion of the incident light into usable energy forms is based on the optical and electrical properties the absorber material. The optical property such as the absorption coefficients, absorption of sunlight, heat transfer, and heat loss play important roles in the optimization of solar radiation to thermal energy [5, 6, 33, 70]. Absorption of light can cause several phenomenal to occur such as excitation of electrons, vibration, and rotation of bonds as well as ionization of atoms or molecules. The photothermal process is created via thermal effects which is caused by photo-excitement phenomena in the absorber surface to enhance the conversion performance of incident light to thermal energy [34, 71]. According to Gao *et.al* [72], the solar-to-thermal energy conversion mechanism is categorised and depends on their light absorption wavelengths as plasmonic localized heating in noble metals, nonradiative relaxations in semiconductors, and thermal vibrations in organic molecules (e.g in carbon-based compounds, conjugated polymers etc.) as shown in Fig.2.2 (a-c).

The electromagnetic radiation absorption of plasmonic noble metal (like Ag, Au etc.,) NPs is governed by the surface plasmonic resonance effects and strongly depends on the structure, size, and shape of the absorber nanoparticles. Optical absorption primarily activated by intra-band transitions when the free conduction electrons are excited within the conduction band, and this absorption is called free carrier absorption as shown in Fig.2.2 (a). The noble metals exhibit intense bright colors caused by wavelength extinctions due to the localized surface plasmonic resonance (LSPR) effects, three successive processes namely, nearfield magnification, hot electrons, and photo-thermal conversions occurred in a plasmonic noble metal. The photothermal effect in noble metals occurs by the illumination of noble metallic NPs, and results in electronic oscillation at unoccupied states by the electron (e$^-$) excitation

from occupied state, which creates hot electrons. These hot electrons are cooled fast due to electron-phonon scattering with in the noble metal lattices, and then, heat is distributed through phonon-phonon relaxations into the environment [72, 73].

The optical absorption in inorganic semiconductor materials reveals strong variation near the band-gap energy. Practically, when photons have higher energy than the band-gap energy of semiconducting materials under illumination leads to an electron-hole (e^--h^+) pairs generation by exciting of electron (e^-) to the CB from the VB as illustrated in Fig.2.2(b). Eventually, the excited electron (e^-) is returned to the low-level states by transferring thermal energy or heat to impurities/ defects by radiative relief in the form of photons or nonradiative relaxations in the form of phonons (or heat) to surface bonds of the semiconductor absorber. When energy is transferred to the surface bonds in the heat form, it causes local heating depending on the optical absorption strength and surface recombination properties [34, 74].

Many carbon-based organic molecules such as carbon black, amorphous carbon, and graphite have the ability to absorb broad-band light and convert solar energy to heat via lattice vibrations within a material. The common optical transitions of n-π^*, π-π^*, and n-δ^* are generally weaker than δ-δ bonds due to the electrons being less bonded and thus, these electrons (e^-) can be excited with a lower photo-energy of the sun in the solar spectrum. The energy difference between the highest occupied molecular orbitals (HOMO), and that of lowest unoccupied molecular orbitals (LUMO) is decreasing with increasing number of π bonds. When a material is illuminated, an electron (e^-) is excited from the HOMO to LUMO orbital as shown in Fig.2.2(c). Eventually, the excited electron (e^-) is relaxed by electron-phonon coupling, and subsequently, the absorbed energy is transferred from the excited electron (e^-) to vibrational modes throughout the atomic lattices which leads to increase the temperature of the absorber [33, 34, 74].
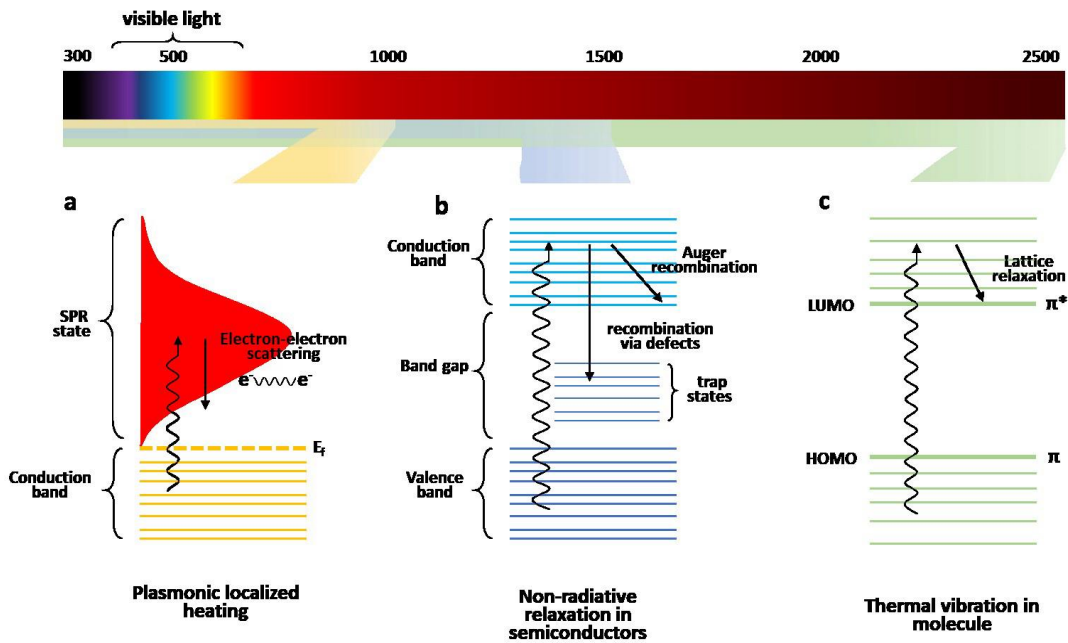
Figure 2.2: Photoexcitation phenomena in photothermal conversion a) in plasmonic metals, b) in semiconductor metal oxides, c) Carbon-based organic molecules [33].

2.3 Properties of spectral solar selective absorber surfaces

In nature, there is no intrinsically perfect absorber material which can be used in SSA coatings. The spectrally solar selective absorbers (SSSA) are a key component in photothermal energy conversion, and also the material types, structure, fabrication procedures etc., determine the optical performance of the absorber surface [13-18, 65]. Solar radiation has a broad spectral range, but its energy is primarily concentrated in the range of UV-Vis-NIR region; Meanwhile, the thermal radiation of the absorber is distributed in the wavelength of far IR region. The SSA coating is said to be ideal spectral selective absorbing if it absorbs all solar radiation in the UV-Vis-NIR ranges while reflecting all thermal radiation in the IR ranges. Ideally, SSSA has low reflectance (≈0) in the solar spectrum (0.3–2.5 μm), and high reflectance (≈1) in the infrared region (>2.5 μm). The solar and thermal spectrum of heated bodies do not overlap to any substantial extent. As the temperature of the blackbody is increasing, the maxima radiation increases and location of the corresponding peak density can shift towards shorter wavelength. The wavelength at which the transition occurs is referred to as the cut-off wavelength and depends on the material type and operational temperatures. For example, at higher temperature, the transition waves will shift towards shorter wavelengths while at lower temperature towards longer wavelengths [6, 15, 51-54, 75-78]. Clearly, Fig.2.3 below illustrates the relation of the solar region (AM, 1.5, blue), ideal

12

reflectance spectrum (black), perfect blackbody radiations (at 100, 200, 300°C) and actual solar selective absorber (red).
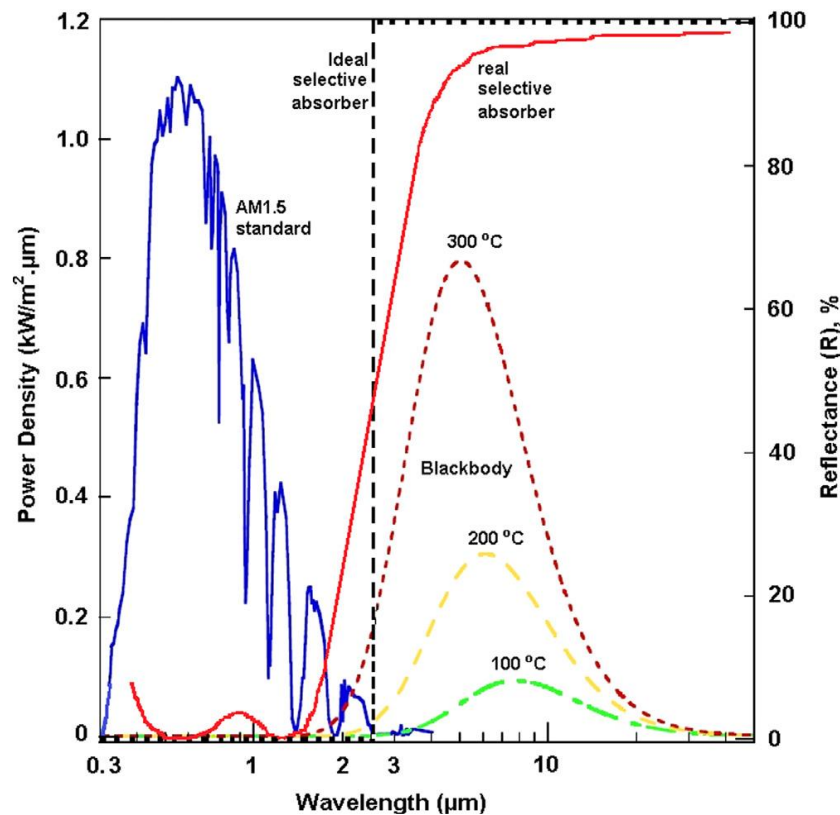
Figure 2.3: Spectral illustration of an ideal and real SSSA, the sun light at AM1.5, and blackbody at different temperature (T) [67].

2.4 Design of spectral solar selective absorber coatings

The solar selective absorber (SSA) coatings are primarily used to improve the ability of solar thermal collectors, particularly in photothermal applications to harvest solar radiation. The first investigations of SSA coatings were projected by Tabor [79], Gier, and Dunkle [61], and Shaffer [80] in 1955. Different physical mechanisms and design principles are employed to improve the absorbing efficiency of the coatings. The absorber types, structures, fabrication processes, and other criteria determine the optical response and performance of the absorber coatings at its operational temperature. The spectral selectivity, good chemical and structural stabilities, ability to prevent oxidation/reduction, humidity, and corrosion can determine the desired properties the absorber surface should possess. Based on designs, and principles, the SSSA coatings are categorised into six (6) namely, intrinsic, semiconductors, metal-dielectric composites, metal-dielectric, multilayers, and textured surfaces [2, 68], as illustrated in Fig.2.4.

13

2.4.1 Intrinsic absorbers

The intrinsic or mass absorber coatings inherit spectral selectivity as a property and are homogeneous materials (see Fig 2.4(a)), structurally more stable but optically have lower efficiency when compared to other types of SSA coatings [65]. The intrinsic absorbers are mostly found in transition metals and are characterized by large number of orbitals for absorption of solar radiation. Semiconductors such as tungsten (W) metal [55], ZrB_2, HfC [81, 82], V_2O_5 [83], Fe_3O_4 [84], etc, are examples of intrinsic materials. They are not ideal for solar applications without modifications and thus the property of the intrinsic material should be tailored with some other materials to satisfy the needs of solar selectivity properties [65, 85].

2.4.2 Semiconductor absorbers

Semiconductor absorber materials have promising prospects due to their invulnerability to photo-bleaching, degradation, and large extinction coefficients in NIR region. Semiconductor materials show an intrinsic property because they are transparent for photons with lower band gap (Eg) energy but absorb energy above the bandgap. Bandgap energy (Eg) governs the light absorption in semiconductor absorbers. Semiconductors with energy band-gaps (Eg) in the range of 0.5 eV (2.5µm) to 1.26 eV (1.0 µm) can absorb sunlight with short wave radiation [11, 32]. The common semiconductor materials are germanium Ge (0.7 eV), silicon Si (1.1 eV), and lead sulfide PbS (0.4 eV) have good potential as absorbers in photothermal applications [86, 87]. Xiao *et.al* [88] took advantage of narrow band gap of copper oxides (CuO, Cu_2O) semiconductors for solar absorptions. The disadvantage of the semiconductor absorber is that it has a higher refractive index (n) in the solar region which causes large reflection of photons and thus, the antireflection coating (ARC) is deposited onto semiconductor to improve its performance or of high porosity are needed to reduce the reflectance losses as illustrated in Fig 2.4 (b). A single layer ARC of Al_2O_3 [89], Si_3N_4, TiO_2 [90] etc., can deposit on semiconductors to reduce its reflectivity. Barrera *et.al* [91] fabricated CuO/SiO_2 thin film via sol-gel method comprised of tetraethoxysilane (TEOS), and copper propionate ($Cu(C_3H_5O_2)_2$) solutions on SS substrate using dipping process. The final film was thermally oxidized at 450 °C for 4 h in air, they reported 92% of solar absorptance (α), and 20% of emissivity (ε).

2.4.3 Cermet absorbers

A cermet (combination of ceramics and metals) coating is a composite absorber in which fine metal nanoparticles are incorporated into a porous ceramic-based layer as shown in Fig 2.4(c). By scattering solar radiation between the metal nanoparticles and the dielectric, the metal in cermets can be modified through the ceramic matrix for high optical response. The multilayers and ceramic coatings are similar in that dielectric material is used in both structures for solar absorptions, while metal nanoparticles can serve as infrared reflectors. The cermet coatings strongly absorb the incident radiation in the wavelength of solar region and are transparent in the IR wavelengths because of inter-band transitions in the metal and plasmonic effect of the fine particles. The surface plasmonic resonance (SPR) phenomenon due to quantum confinements (QCs) effect of the metal NPs in cermet coatings can trap more sunlight. In general, coating thickness, particle concentrations, size, orientation, and shape determine the solar selectivity of the cermet coatings [68, 70, 92]. Different dielectric materials like Cr_2O_3, Al_2O_3, etc., as dielectric, and Cr, Ni, W, Al, Au, Ag etc.,) as the metallic NPs have been investigated for cermet composite coatings [92, 93]. Such kind of cermets, like W-Al_2O_3 [94], Ag-Al_2O_3 [95], Mo-Al_2O_3 [96], and Ni-NiO [97] have been reported for SSA coatings. The advantage of DMD structure is that small material is required to fabricate the coatings, which reduce usable costs [17, 98].
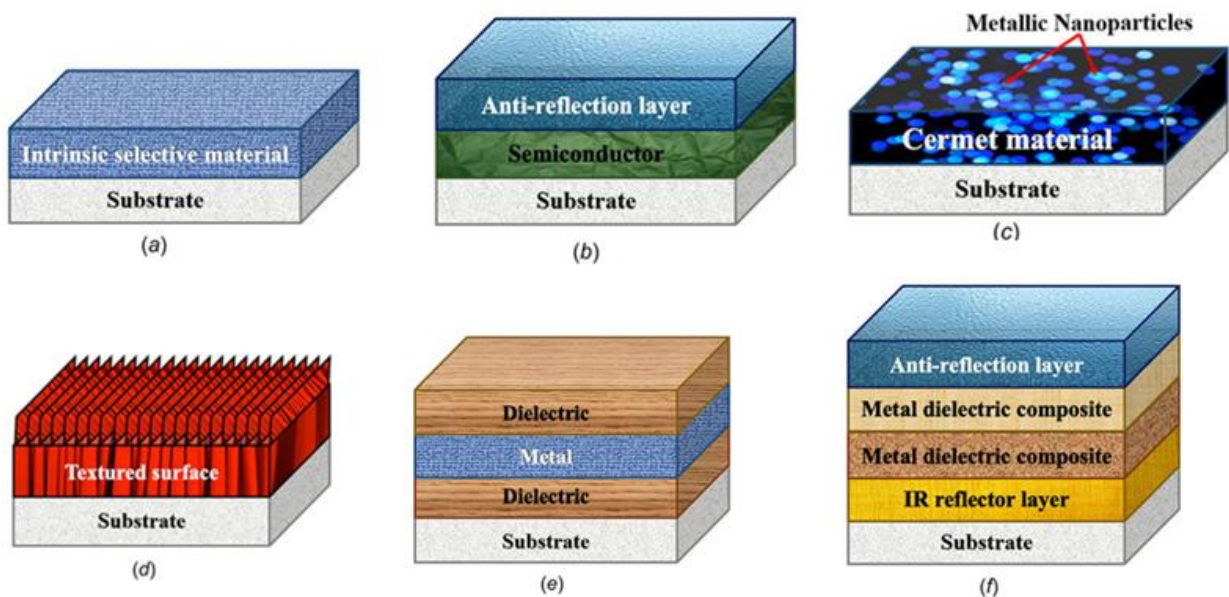
Figure 2.4: Types of SSA coatings for solar energy absorption [60].

2.4.4 Multilayer absorbers

The semiconductor and intrinsic absorbers are not appropriate in high temperatures used for photothermal applications. Multilayer coatings reveal high solar absorption, low emissivity, and good stability at high temperatures. A multilayer coating consists of antireflection layer (ARL), dielectric, and semi-transparent metallic layers shown in Fig 2.4(f). Multilayer films can improve the solar selectivity properties of the absorber with dielectric layer as the main absorber and metal layers as IR reflectors. The bottom metallic layer (e.g. Cr, W, Ag, Cu, Ni) exhibits a high reflectance property in the IR wavelength and less reflectance in the visual region. The top antireflection layer (e.g Al_2O_3), reduced the visual reflectance. To improve solar absorption of multilayer absorbers the metal volume fractions and refractive indexes of each layer typically increase from surface of the absorber to substrate [11, 92, 98]. In recent years, the transition metals and their nitrides/oxynitrides/oxides coatings such as TiAlSiN/TiAlSiON/SiO$_2$ [99], Mo/AlCrON(H)/AlCrNO(L)/AlCrOx [100], HfMoN(H)/HfMoN(L)/HfON/Al$_2$O$_3$ [101], TiAlCrN/TiAlN/AlSiN [102] have been reported for high temperatures photothermal applications.

2.4.5 Dielectric-metal-dielectric (DMD) absorbers

Multiple reflections are used in dielectric-metal-dielectric (DMD) absorbers to absorb the sunlight efficiently (see Fig 2.4(e)). Nanocrystalline dielectric materials such as Cr_2O_3, MgO, Al_2O_3, and others are suitable absorbers in DMD coatings because of their great temperature stability. Moreover, based on the high melting point and their resistance against chemical oxidations at higher temperatures, metals like Cr, Al, etc., are suitable candidates for DMD absorber layer. Different DMD absorbers such as HfOx/Mo/HfO$_2$ [103], AlxOy/Al/AlxOy [103] etc., have reported for high photothermal applications. The advantage of DMD coating is the lower coat required to fabricate the coating structure. The issue in developing such layers is to find tuneable composition that bridged the gap between metal and dielectric optical characteristics and maximizes solar absorptions while reducing thermal emissivity [68, 70].

2.4.6 Textured surface absorbers

Textured surface coatings are emerging coatings both in the micro, and nanomanufacturing technology. Though the optical performance of other coatings reported in literature are superior, the oxidation, intra and interlayer reactions, substrate diffusion, and

thermomechanical stress between the layers at high temperature fails. To overcome the aforementioned gap, materials with high intrinsic absorption, and unaffected selective property, surface texturing appear as an alternative approach (see Fig 2.4(d). Textured surface structure with porous grooves, dendrite micro and nanostructure are capable of capturing solar energy and are the main way to improve solar absorptance materials. Such structure can help to trap more short wave photons via multi-reflection inside the structures, while smooth absorber surfaces for longer waves can achieve low emissivity [68, 70, 85, 104]. Moon *et.al* [105] demonstrated a multi-scaled silicon (Si) germanium (Ge) absorber surface through a spark erosion process with an absorptivity(α) of 0.9 and emissivity(ε) of 0.3. Sergeant *et.al* [106] proposed a design of V-groove grating coatings, which has $\alpha > 0.94$ and $\varepsilon < 0.06$ at 720 K.

2.5 Solar thermal collectors

A unique heat exchanger known as a solar collector is used to harvest the sun light and convert it into thermal energy. Solar collectors are the major component in the system and are designed to harvest and convert the incident solar radiation into heat and then to electricity to satisfy some energy demands. Solar energy can be harnessed using passive and active approaches. Design and structural aspects of solar systems can be named as the passive techniques. The solar energy uses mechanical and electrical equipment to convert the sunlight into heat and/or electricity using active solar approaches [56, 65, 107].

Solar thermal collectors are heat exchangers that convert solar radiation into thermal energy and stores it for later use. Transferring of solar energy into heat transfer fluids (HTFs) via absorber plates is the core mechanism in solar-to-thermal conversion. A solar thermal collector can absorb the incident light, and heat is then transferred to working fluids (i.e, water, air, or oil), and the heat in the working fluids can be used directly for various applications such as domestic and commercial applications. Many solar thermal collectors are available for photothermal energy conversion, and basically, solar thermal collectors are categorised as concentrating and non-concentrating collectors. Non-concentrating solar collectors are generally used in residential areas and commercial buildings for hot water and space heating, while concentrating collectors are typically used in solar power plants [108-110]. Fig. 2.5 illustrates the concentrating, and non-concentrating types of solar collectors.
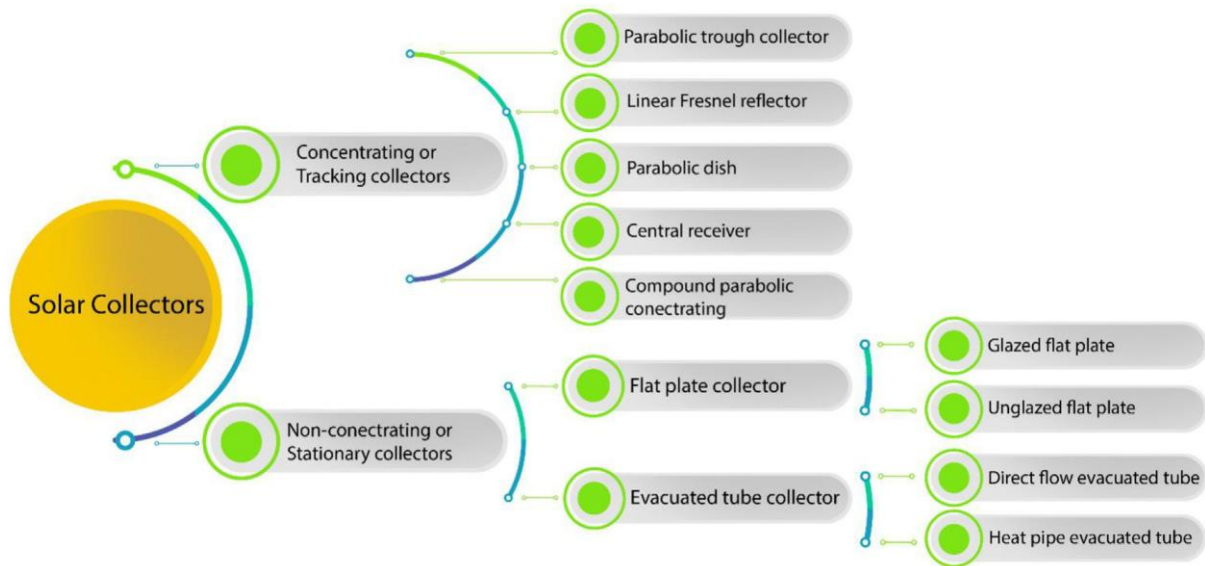
Figure 2.5: Different types of solar collectors [68].

2.5.1 Non-concentrating solar collectors

Non-concentrating solar collectors are mainly designed for domestic purpose, tertiary sectors, and some industrial processes which require energy delivery at low, and medium temperatures. Though a broad variety of non-concentrating collectors are available, flat plate collector (FPC) and evacuated tube collectors (ETC) are the two main types of non-concentrating solar thermal collectors [68, 108].

2.5.1.1 Flat-plate solar collector

Flat-plate collectors (FPCs) are the most investigated technology and are low-cost and do not require more skill to operate. The FPC consists of a glazing transparent cover, absorber plates, insulation layers, heat transfer fluid (HTF), and other auxiliaries as illustrated in Fig.2.5.1.1. Glazing transparent cover is made of single or multiple sheets of transparent material with high transmittance in the short wavelength radiations and low transmittance of in the long wavelength radiations. Moreover, the transparent cover prevents the absorber plates from adverse weather conditions. The absorber plate is generally coated with blackened surfaces able to absorb the incident sunlight but transparent to long-wavelength thermal radiations. The absorber plates can be covered with a selective layer to maximize the solar absorptions. The heat is then transferred to working fluids in the absorber tubes. To reduce heat losses, the absorber plates are well-insulated on all sides. Due to high solar radiations and lower heat losses, conventional flat-plate solar thermal collectors work efficiently in warm climate seasons [109, 111-113].

18
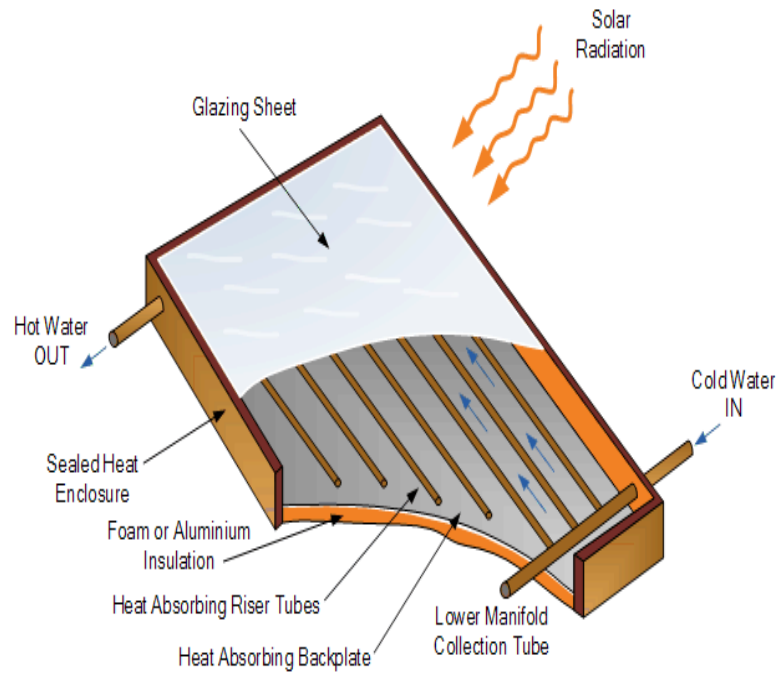
Figure 2.5.1.1: Illustrative of a flat-plate collector [112]

2.5.1.2 Evacuated tube solar collectors

The evacuated tubular collector (ETC) consist of row of parallel transparent tube glasses with absorber plates to absorb the incident radiation in the solar region and a heat transfer tube to collect the absorbed energy in each glass tube, as shown in Fig.2.5.1.2. The absorber plate is responsible for collecting the incoming solar radiation, and also reduces the heat loss in the infrared radiation. It is purposely painted with a dark color to maximize absorption. The heat from the absorber plates is transferred to the HTF, which is then transported to manifold mainstream fluids. The manifold is insulated to prevent heat loss and the air between the outer and inner glass tubes is evacuated to prevent convective heat loss. This leads to a better photothermal conversion, and it is commonly employed in medium-temperature applications. ETC is reported to be less expensive, easier to transport and performs better than FPC [108, 111, 112].
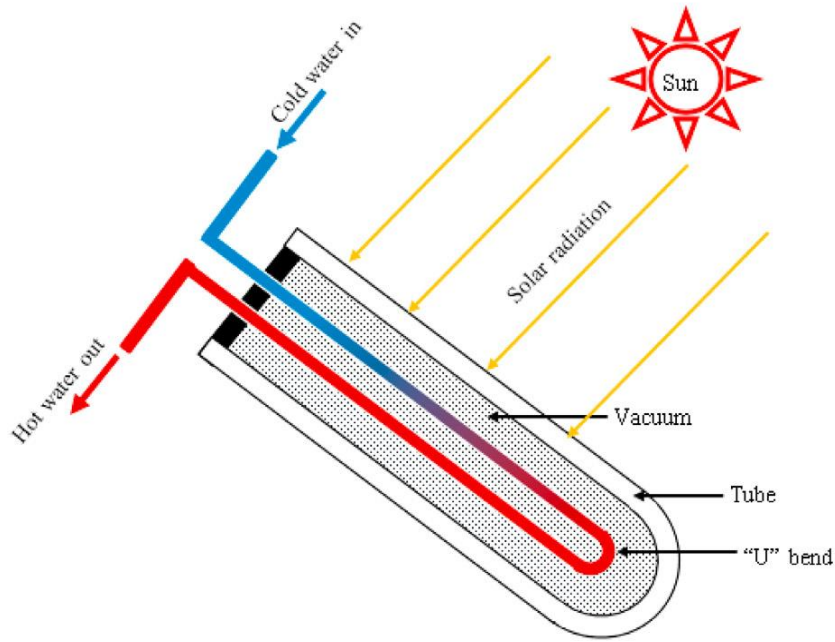
Figure 2.5.1.2: Illustrative of evacuated tube collectors [112].

2.5.2 Concentrating solar collectors

Concentrating solar power (CSP) is one of the matured solar thermal technologies that has shown significant potential for the future and is presently being deployed around the world. Concentrating thermal collectors reflect the incident solar beam radiation onto a small surface using reflective and/or refractive absorber surfaces. The CSP plants generate electricity, but it uses sunlight as a source of energy. Concentrators, receivers, storage/transporter media system (gas, molten salt, air, etc.), and conversion devices are the four main components of a CSP system. In CSP system, the incident solar radiation is concentrated by mirrors and focused the solar radiation on the receiver surface for processing heating and/or power generations (see Fig. 2.5.2 (i)). The absorber is usually deposited with a selective coating onto the receiver tube, where HTFs are heated to have higher absorptivity in solar spectra and lower thermal emissivity in the far IR spectrum. The HTF by the absorber is driven via a series of heat exchangers to generate superheated steam. The steam is then utilized to power a generator, such as gas or steam turbine engine. The main advantage of concentrating solar thermal collectors is conversion of sunlight into high temperature as compared to non-concentrating collectors; however it concentrated only beam radiations, not diffuse radiations [65, 112, 114].
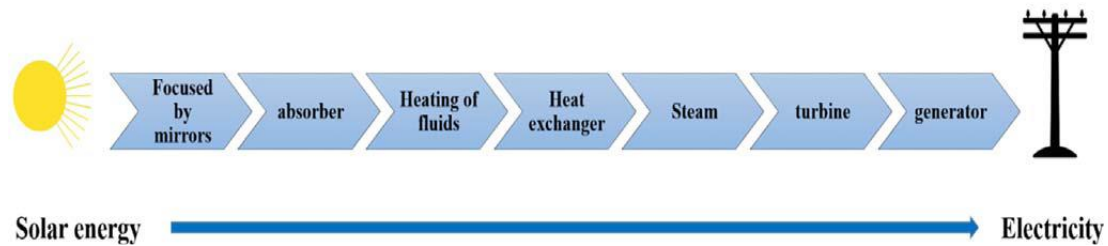
Figure 2.5.2(i): Schematic mechanism to generate electricity from sun light in CSP systems [65].

CSP technologies are classified into four solar collector types based on how they focus solar radiation and technology used to collect solar energies: parabolic trough collectors, solar tower collectors, parabolic dish collectors, and Linear-Fresnel reflectors [65] as illustrated in Fig. 2.5.2(ii). In parabolic trough collector (PTC) technology, there are a series of curved mirrors to concentrate solar radiation onto receiver tubes located in the curved trough's focal lines (see Fig. 2.5.2(ii) (a)). The concentrator is made of polished metal sheets properly bent or it is composed of concave mirrors. Through this system, the solar energy is reflected on the receiver tubes, bringing it to higher temperature of approximately 400 °C, and heating the HTF e.g, oil, that flows via the receiver tube along the trough solar collectors. The superheated steam in HTF powers a turbine, which drives a generator to generate electricity, and the water is cooled and condensed before returning to the heat exchangers/HTF. Parabolic trough technologies can be used in an existing coal-fired power plant or combined-cycle systems [92, 108, 115].
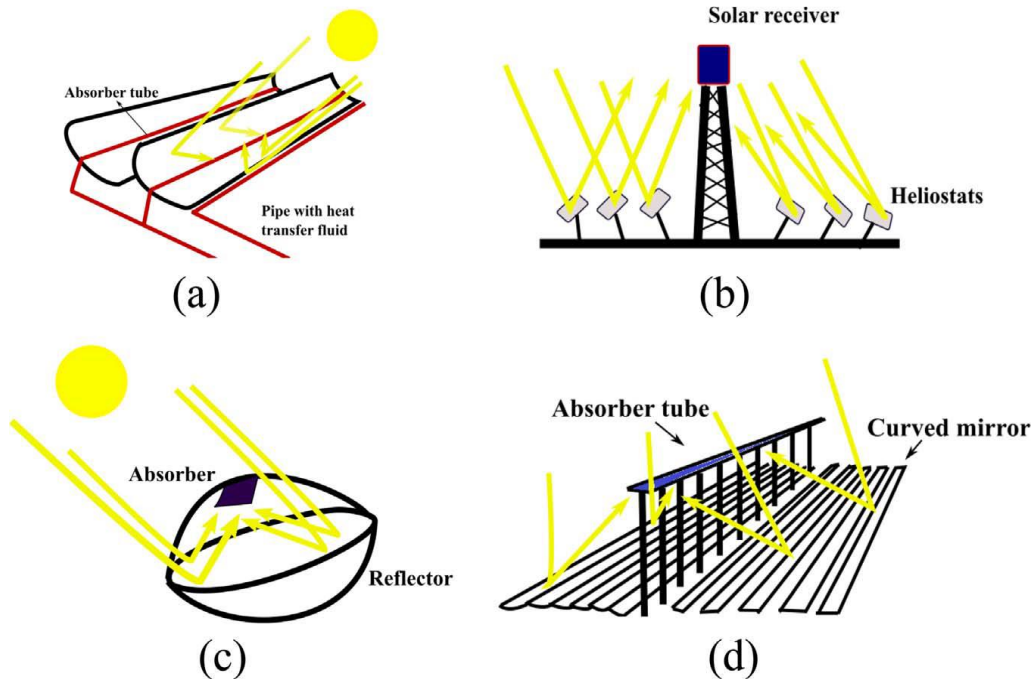
Figure 2.5.2(ii): Illustrative of four concentrated power systems a) parabolic b) solar tower c) concentrated dish, and d) Fresnel reflectors [65].

The sunlight rays are tracked by large mirrored collectors known as heliostats in solar power tower collectors. Each heliostat is independently oriented to directly reflect incoming sun light onto the central receiving units and concentrate the solar energy flux by focusing the sunlight on the receivers, which is located on top of a towers (see Fig. 2.5.2(ii)(b)) and this transfer energy to a working thermic fluid at higher temperatures (>1500 ^{o}C) for power generation. The HTF, which is molten salts or water/steam, that flows into the receiver, is heated by concentrated sun light and then used to generate electricity in generators and turbines. An advantage of heliostat field collectors (HFCs) is a large amount of solar radiation concentrated on a single receiver (200–1000kW/m^2), which minimizes heat losses as well as simplifies the heat transport, and storage requirements [92, 115].

On the other hand, the parabolic dish reflector system consists of a parabolic concentrator that reflects sun light onto a receiver placed at the focal point of the dish (See Fig. 2.5.2(ii) (c)). These concentrators are mounted on a structure and tracks the sun radiation with a two-axis tracking system. The fluid or gas (air) in the receiver is heated (750 ◦C), when the focused beam is incident on the receivers. Typically, the collected heat is used by a heat engine mounted on the receiver. For power conversion, Stirling and Brayton cycle engines are currently preferred and various options exist for the HTF thermal energy storage and power cycle [92, 108, 115].

Finally, linear Fresnel collectors uses linear or slightly curved mirrors placed on tracker on the ground arranged to reflect the rays onto a receiver above the mirrors. A Linear Fresnel reflector consists of mirror strips as a Fresnel lens, which concentrates sunlight onto a fixed receiver placed on a linear tower (See Fig. 2.5.2(ii) (d)). The reflector segments are horizontally aligned, following the sunlight, so that the transceiver can be hit by the sun's rays without having to move [92, 116].

2.6 Mechanism of heat transfer in solar thermal energy

Solar energy harvesting systems such as thermoelectric generators and thermophotovoltaics are widely used in solar water heating and concentrated power systems (CPS). In solar-to-thermal conversion the solar collectors are types of heat exchangers that absorbs the incoming sun light and cause to an increase of the internal energy of the absorber. The harvested heat is transferred through heat conduction, convection, and radiation from one body fluid to another. Heat conduction occurs when heat flows from a higher to a lower temperature bodies as a result of collisions between neighbouring particles in the medium and the heat convection occurs when a mass of fluid moves from a heated source to a cooler part. Finally, the heat radiation is electromagnetic radiation and no medium, as well as mass exchange, is required during the process. In electromagnetic radiation the absorber surface on the receiver tube involves maximization of solar absorption with reducing heat losses to ensure high photothermal conversion efficiency [33, 50, 117, 118].

The absorber on the receiver surface captures solar radiation and confines it, reducing heat losses to the environment. The incident light on the absorber surface is converted into a heat flux and transported to the thermal (heat engine) system, where it is converted into the desired output (heat, electricity, etc.). Radiative and convective heat losses heat at the absorber surfaces reduce the photothermal conversion efficiency and thus the absorber is generally deposited with spectrally selective coatings onto receiver tubes, where HTFs are heated to have strong solar absorptance in solar spectrums, and low emissivity in the IR regions. The heat transfer or photothermal conversion system is illustrated in Fig 2.6 below. The solar thermal conversion efficiency (η) of SSA coatings at operating temperature can be determined using eq.(2.1.1.11) [15, 67, 75, 119, 120].
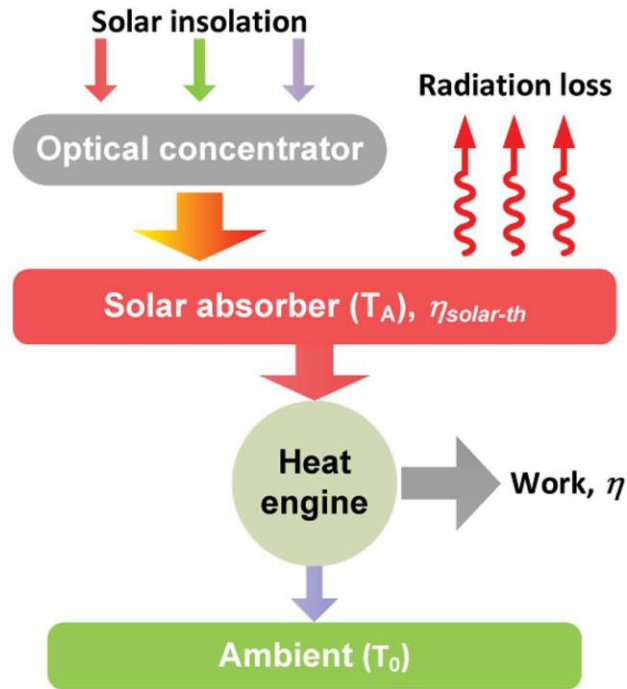
Figure 2.6 Schematic diagram of heat transfer or photothermal conversion system [67, 121].

2.7 Thin films for solar collectors

In the last decades, the need for synthesis of nanomaterials for various industrial applications has resulted in an increase of innovative thin film-based solar energy collecting, conversions, and storage for improved efficiency. So far different solar collector thin films have been fabricated using different methods for various potential applications including photovoltaic, photothermal, fuel cells, supercapacitor and rechargeable batteries [122-125]. Hottel and Unger [55] demonstrated CuO coatings as solar collector thin film on flat plate collectors using spraying a dilute solution of Cu $(NO_3)_2.6H_2O$ onto an aluminum (Al) sheet, and then converted the $Cu(NO_3)_2.6H_2O$ to black CuO by heating it above 170 $^\circ$C. Mohammed *et.al* [125] demonstrated a few-layers of graphene nanoflakes films by vacuum kinetic spray at room temperature for supercapacitors and revealed a high areal capacitance with small series resistance. Xiao Sun *et.al* [126] reported that solution-processed CuO thin films as a light emitted diodes (LEDs) and revealed an external quantum efficiency (EQE) of 5.37% with a maximum brightness over 70,000 cd/m^2.

2.7.1 Deposition of thin films

Synthesis methods and deposition techniques control the microstructural, morphological, electrical and optical properties of the thin films [127-129]. Thin film deposition techniques are categorised as either purely physical techniques (vacuum thermal evaporations, electron beam evaporations, arc evaporations, ion plating evaporations, sputtering techniques, etc.) or purely chemical (sol-gel techniques, chemical bath depositions, spray pyrolysis, electroplating, chemical vapour depositions (CVD), plasma enhanced depositions, atomic layer deposition, and so on) [127, 128, 130]. Fig. 2.7.1 illustrates thin film processing methods.
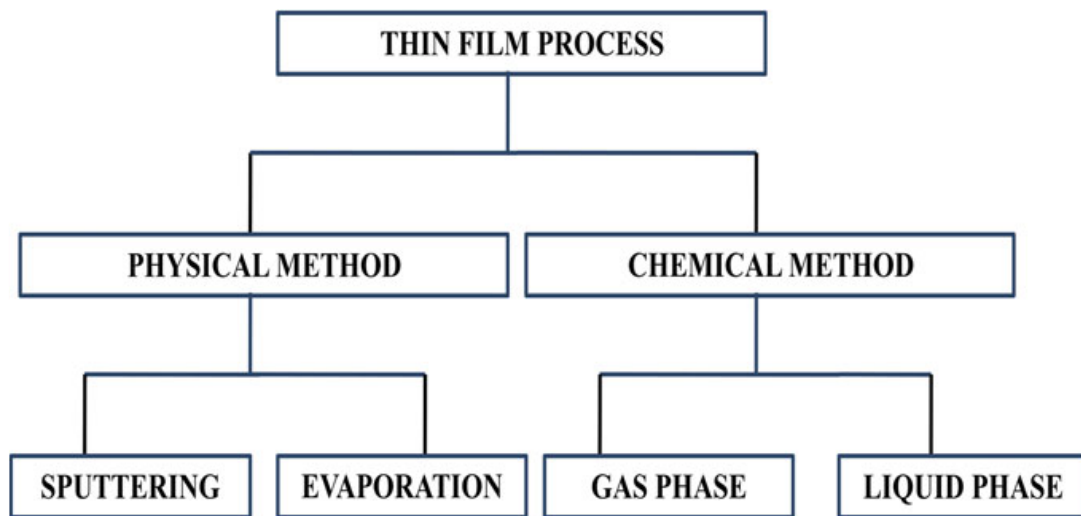
Figure 2.6.1: Diagram of film deposition methods

2.7.1.1 Sputtering deposition

Sputter deposition is a PVD technique for uniform deposition films or coatings on substrates. Atoms are ejected or eroded from the target materials by plasma bombardment and then condensate on a substrate. In essence, plasma is formed by combining inert or reactive gases with energetic ions that knock out atoms or molecules from the raw material or target and deposit these atoms or molecules as a uniform thin film on the surface of the substrate. The sputter plasma can be inert, consisting of argon (Ar) ions and the target; alternatively, the sputter plasma can be reactive, containing, for example, oxygen, and thus an oxide film can be produced by sputtering from a metallic target. Based on the power used and sputtering systems, sputtering can be direct current (DC), radio frequency (RF), magnetron, and ion-beam sputtering. Typically, the chamber is first evacuated, and then the sputter gas is introduced. The RF or DC voltage is applied between the target(s) and substrates to establish a plasma. An inert gas such as argon (Ar) is usually used as the sputter gas, but reactive gases

such as oxygen can also be mixed with the sputter gas. When reactive gases are introduced, the deposition involves chemical reactions [128, 131]. If a metal is sputtered with oxygen, deposition of a metal oxide(MO) film may occur includes, including zinc oxide (ZnO) [132], tungsten oxide (WO)[12] depending on the type of the target metal. The setup of sputtering deposition is illustrated in Fig. 2.7.1.1.
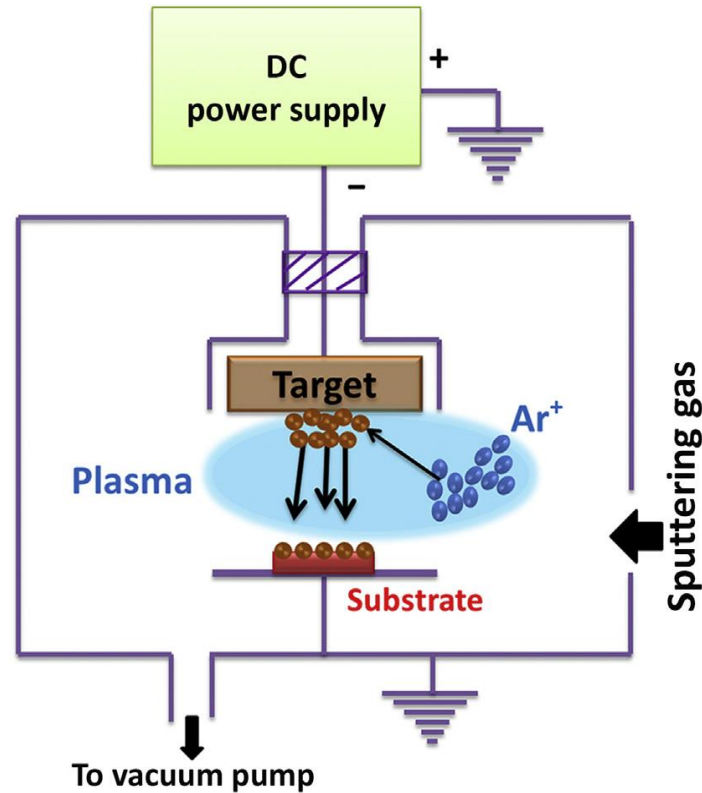
Figure 2.7.1.1: Schematic illustration of sputtering deposition

Co-sputtering is a method where multiple targets are used simultaneously to allow the deposition of a variety of mixed materials for example oxynitrides, metal/metal oxide composites etc. Many industrial applications have been developed by sputtering deposition such as metal films, semiconductor films, and antirejection coatings etc. SSA coatings have also been extensively studied using sputtering [61, 133]. Zhang *et.al* [134] demonstrated W/AlN, Mo/AlN, and SS/AlN cermets using direct current (DC) sputtering in the presence of Ar and N_2 gases. S. K.Kumar *et.al* [135] reported a nanostructure CuO thin film on Cu substrates in the mixture of oxygen (O) to Argon (Ar) gases ratio via DC sputtering for photothermal applications and achieved absorptance(α) value of 0.71, and emissivity(ε) of 0.07.

2.7.1.2 Electrochemical deposition

Electrochemistry deals with the interconversion of chemical and electrical energy for electrochemical energy conversion and storage technologies. Electrochemical methods are known as electroplating, and widely used for the preparation of metals, semiconductors, or metal oxide (MO) thin films on the conductive substrate due to its simplicity, room-temperature processing and industrial viability. It has also advantages because the growth orientations, morphological, structure and size of the thin film products can be easily controlled by the deposition parameter such as voltage, working electrode, electrolyte solution, temperature, electrode configuration etc.) [136-138]. Typically, an electrodeposition set-up can be either a two or three-electrode configuration system. The two-electrode configuration consists of the working-electrode (WE), as well as counter, while reference-electrode is included in the case of the three-electrode configurations. Fig.2.7.1.2 illustrates the three-electrode configuration setup of electrochemical deposition. The working electrode (WR) can be defined as the electrode where the electrochemical reaction being investigated, while counter electrode (CE) is an electrode which provides a potential to working electrode (WE) in the electrochemical reaction and made of an inert material like platinum (Pt) metal. The reference electrode (RE) has a well-known electrode potential and serves as a reference point in the electrochemical reaction for potential control and measurement [137, 139, 140].
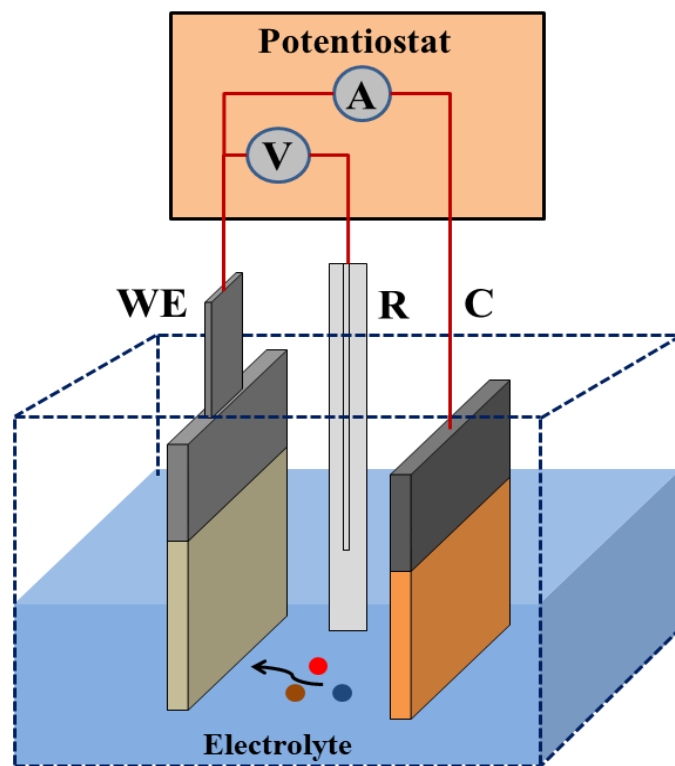
Figure 2.7.1.2: Schematic of the electrodeposition set up

In electrochemical technique, electrolyte concentration, reaction temperature, deposition potential and time are play a vital role in the deposition of thin films. Typically, when a potential is applied across the system, the direct current (DC) source supplies current in one direction and electrical transfer occurs in the electrolyte solution via electrically charged particles known as ions. When a potential is applied, positive ions (cations) travel towards the negative electrode (cathode) and are deposited on the working electrode (WE) surface, while negative ions (anions) travel toward the positive electrode (anode). So far, different CuO thin films for various applications have been fabricated via electrochemical techniques with desirable morphological surfaces [137, 141] such as nano-whisker, nano-dendrite [142], nanodisks [143] nanoribbons [142], and nanorods [144]. Das and Srivastava [143] fabricated nanodisks-like structure of CuO via electrochemical method from copper-succinate $(Cu(C_3H_5O_2)_2)$ electrolyte solution at diverse applied currents. Mancier *et.al* [142] prepared CuO nanopowder via sono-electrodeposition by utilizing mechanical energies to enhanced a specific chemical reactions.

2.7.1.3 Spin coating deposition

Spin coating is the simplest technique that is used to fabricate rapid and uniform thin films on flat a substrate by centrifugal force. The spin coater is the apparatus used in spin coating for

deposition of films on a substrate. The substrate is held in place by a rotatable fixture (often using vacuum), and the solution is dispensed onto the center of a wafer in the deposition stage and then rotated at high speed until the excess solution spins off the substrate and the desired thickness of the film remains. The applied solvent is removed partially during the deposition process and evaporated at elevated temperatures. The thickness of the film is determined by the rotational speed, evaporation rate, surface tension, solution density, surface wettability and viscosity of the solution. A typical spin coating process consists of four basic steps of deposition, acceleration, flow domination, and evaporation. In the deposition step, the solution to be coated is applied onto a substrate for deposition. The amount of applied solution relies on the viscosity of the solution and the size of the substrate. In the acceleration step, the solution is spread across the substrate by centrifugal force. The rotational or spinning speed is set at a specific value for the desired film thickness [145-147].
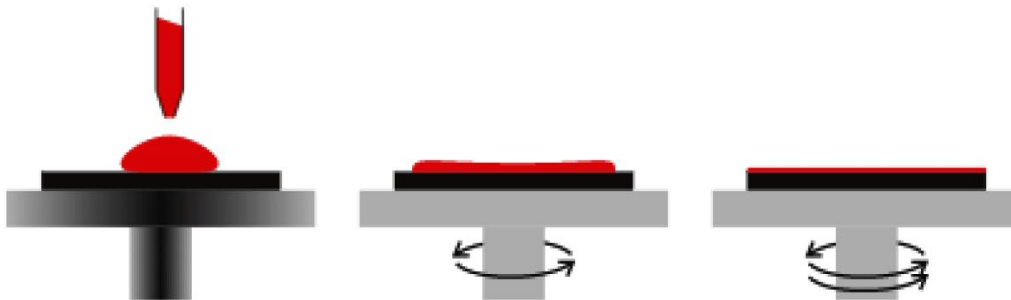
Figure 2.7.1.3: Illustrates process of spin coating

.

 Eskandari *et.al*[148] used copper acetate tetrahydrated ($Cu(C_4H_3O_2)_2.4H_2O$) precursor to prepare cuprous oxide (Cu_2O) via sol-gel methods, and then spin-coated for hydrophobic properties. He *et.al* [149] fabricated superhydrophobic ZnO nanorods via electrochemical and spin-coated on zinc foil, and the maximum contact angle achieved was 167°.

2.8 Introduction to copper oxide

Nanoscale transition metal oxide (TMO) thin films are the unquestionable prerequisites for the development of a wide range of novel smart, and functional materials. Preparation and characterization of nanosized metal oxides (MOs) have gained immense attention for both scientific research and practical applications due to their unique physical and chemical properties. MOs properties are in a wide range of characteristics inherent to metals, semiconductors, and insulators [138, 150]. Among the TMOs, oxides of copper (Cu) metal have provoked attention due its large surface area, optical properties, non-toxicity, and abundance in nature, good thermal conductivity and catalytic activity. Copper (Cu) metal is a universal element with $[Ar]4s^13d^{10}$ electron configuration, and it has high electrical and thermal conductivities [36-38]. Cupric oxide (CuO) and cuprous oxides (Cu_2O, cuprite) are stable oxides of Cu metal. Although the properties are contrasting, both oxides have an important application in modern technologies due to their low bandgap, high absorption, nontoxicity, and low-cost [151-154]. CuO (tenorite) is a transitional metal oxide from two elements copper (Cu, ($[Ar]4s^13d^{10}$)) and oxygen (O, $[He]2s^22p^4$) which are block d and block p elements, respectively. The Cu ions are coordinated by four oxygen ions in a monoclinic phase of CuO crystals. Basically, CuO is a p-type semiconductor due to Cu vacancies and interstitial oxygen within the structure, and it has narrow band gap values of 1.2-1.9 eV. CuO has the advantages of ease of synthesis, low cost, environmental friendliness, chemical stability, natural abundance, and good electrical conductivity. CuO with large surface area exhibits superior physical and chemical properties and has been widely studied using different approaches in various fields, such as biology, chemistry, medicine, and physics and [155, 156].

2.8.1 Synthesis strategies of CuO nanostructures

Innovative and convenient synthesis techniques play an important role in understanding the fundamental importance and practical applications of nanomaterials. So far, considerable efforts have been made to design, synthesise and fabricate MOs to modify the morphology, particle size, size distributions, crystal structure, as well as elemental and/or chemical composition reaction parameters, which in turn provide promising development in various smart materials and novel functional. Numerous synthetic strategies have been developed to synthesises various nanostructured CuO with diverse particle sizes, surface morphology and controllable dimensions [157, 158]. CuO nanostructures with different dimensions like zero,

(0D), two-dimensional (2D), and three-dimensional (3D) as well as diverse surface morphologies such as nanospheres [159], nanoflowers [160], nanowires [161], nanoplates [162], nanorods [163], etc., have synthesized using methods (Fig. 2.10.1).
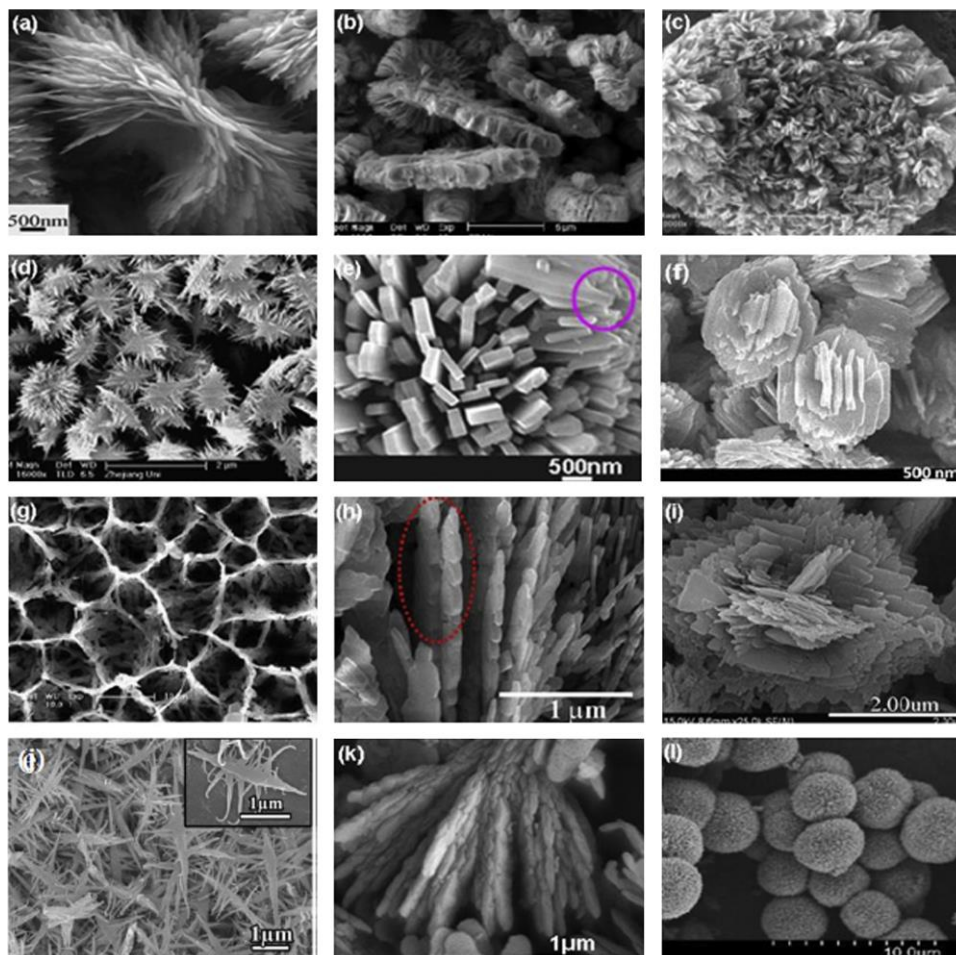
Figure 2.8.1: SEM images of CuO nanostructures (a) butterfly-like[164] , (b) gear wheel bundles [165], (c) nanoflowers [160], (d) dendrite-like[166], (e) nanobat-like [167], (f) layered hexagonal [168], (g) honeycomb and leaf-like [160], (i) peachstone-like [169], (j) shrimp-like [170], (k) sheaf-like [171], and (l) urchin-like spheres [159].

Generally, synthesis strategies of CuO are categorized into three approaches, namely physical (such as arc discharge, electron beam, ion implantation, vapour phase synthesis, etc,) chemical (such as, co-precipitation, chemical oxidation/reduction, pyrolysis, sol-gel, hydrothermal, solvothermal etc.), and biological (such as, plant extracts, microorganisms, biomolecules etc.,) approaches. Conventional physical, and chemical procedures have been extensively studied and used in scientific research and industrial areas, while biological methods involve a complicated process and, thus, have not been largely used [51, 52, 172-177].

2.8.1.1 Physical approach

Physical methods use mechanical forces or high vacuum to break the particles or use a beam of atoms to form nanoparticles. Physical vapour deposition (PVD), and sputtering are the commonly used physical methods to prepare nanoparticles. PVD involves converting a solid bulk material into a gaseous phase and then cooling it under vacuum conditions to re-deposit particles with nanoscale dimensions. Similarly, sputtering uses high-energy ion sources to knock molecules or atoms from the target atom and subsequently deposit on a substrate. Copper oxides have been synthesized via different physical methods such as PVD, sputtering, and arc evaporation. Generally, physical procedures are highly useful in producing ultra-thin and highly pure nanoparticles, nanostructure particles, and nanoalloys [178-181].

Physical Approach
- Sputtering
- Thermal evaporation
- Arc discharge
- Electron beam
- Ion implantation
- Pulsed laser
- Physical vapor deposition

Chemical Approach
- Thermal oxidation
- Thermal decomposition
- Sol-gel processing
- Pyrolysis
- Hydrothermal
- Solvothermal
- Chemical precipitation

Green Approach
- Plant extracts
- Microorganisms
- Biomolecules
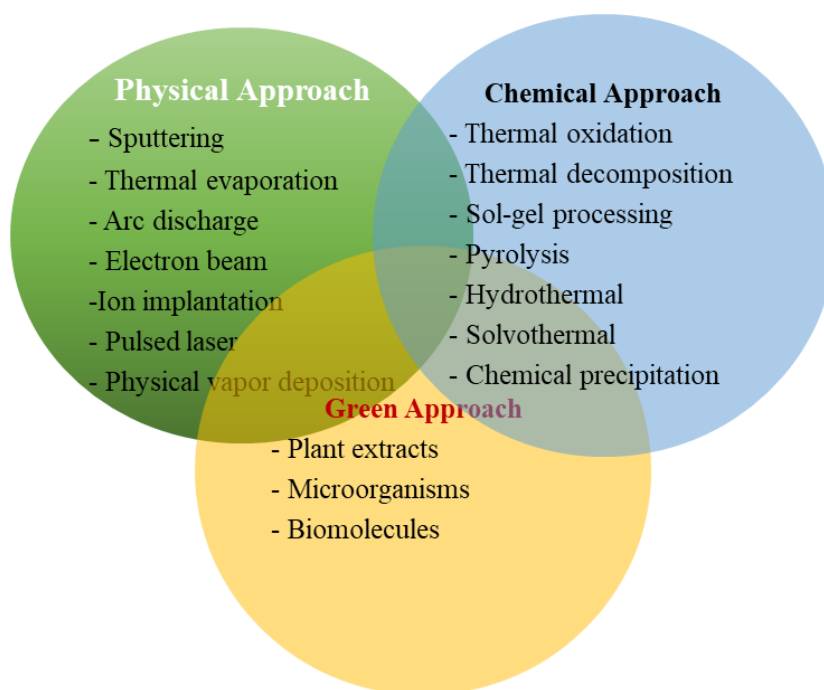
Figure 2.8.1.1: Synthesis approaches of CuO nanomaterials

2.8.1.2 Chemical approach

Chemical approaches are other conventional techniques and involve formation of ions through a series of chemical reactions for the preparation of nanoparticles. Nanostructured copper oxides (CuOs) have been reported via different chemical procedures such as chemical precipitation, hydrothermal [182], chemical vapor deposition (CVD) [183], microwave [184], chemical precipitation and mechanochemical [185]. Copper oxides are generally synthesised from copper salt precursors in the presence of organic and/or inorganic reducing/oxidizing

agents. Copper sulfate hexahydrate ($CuSO_4.6H_2O$), copper nitrate trihydrate ($Cu(NO_3)_2.H_2O$) copper acetate tetrahydrated ($Cu(C_4H_3O_2)_2.4H_2O$) and copper chloride ($CuCl_2$) are the common precursors for the preparation of CuO nanoparticles. Chawla *et.al* [185] fabricated spidle-like CuO nanostructure via facile chemical precipitation method from $Cu(C_4H_3O_2)_2.4H_2O$ and $Cu(NO_3)_2)$ precursors with a grain size of 60 and 32 nm, respectively. Table 2.8 summarizes the surface morphology, synthesis methods, and applications of CuO nanoparticles.

Table 2.8 Summary of surface morphology, synthesis methods, and applications of CuO

Morphology	Reactant materials	Additives	Synthesis method	Application	Ref.
Nanoplatelets	Cu_xS & NaOH Cu foil	H_2O_2	Hydrothermal	Electrochemical Solar energy	[160, 186]
Microspheres	$Cu(CH_3COO)_2 \cdot 3H_2O$		Hydrothermal	LIBs	[187]
NanoLeaf, shuttle, flower	$Cu(CH_3COO)_2 \cdot 3H_2O$ NH_3		Hydrothermal	LIBs	[188]
Dendritelike structures	$CuCl_2.2H2O$ CH3COOH		Kirkendalle effect-based approach	LIBs	[189]
Nanoleaves	$(CuSO_4 \cdot 5H_2O)$ NaOH		Aqouse solution	Glucose Sensor	[190]
Nanowires	CuO		Sputtering	Ethanol gas Sensor	[191]
Microspheres	$Cu(NO_3)_2 \cdot 3H_2O$ & $CO(NH_2)_2$		Hydrothermal & calcination	Sensor	[192]
Nanofibers	$Cu(CH_3COO)_2 \cdot H_2O$ & syringe		electrospinning	Solar cells	[193]
Nanorod	copper foil & NaOH		Chemical oxidation	Solar cells	[194]
Nanowires	Cu foil		Thermal oxidation	Photodetector	[188]
Nanowires	Cu foil		Thermal oxidation	Catalysts	[195]
Nanowires	$CuSO_4 \cdot 5H2O$ CTAB		Chemical precipitation	Photocatalysts	[196]
Nanowires	Cu foil & NaOH	$(NH_4)_2S_2O_8$	solution route	Photocatalysts	[175]
Nanowires	Cu foil		Thermal oxidation	Field emission displays (FEDs)	[197]
Nanocabbages	CU foil, NaOH		Aqouse solution	Superhydrophobic	[198]
Nanoparticle	$Cu(CH_3COO)_2$	urea	Microwave	Photothermal	[199]
Nanospheres	$Cu(CH_3COO)_2$ & NaOH	EDTA	Microwave	Solar absorbance	[200]
Nanoscrolls and nanotubes	Cu substrate NaOH	$(NH_4)_2S_2O_8$	Chemical oxidation	Superhydrophobic	[201]
Nanosperical	Cu foil		Sputtering	Photothermal	[39]

2.8.1.3 Biological approach

Physical and chemical synthesis methods are the most used procedures to prepare CuO nanoparticles for various applications but they remain expensive and involve the usage of high energy and/ or toxic chemicals. These disadvantages have led to the emergence of green chemistry or biological methods based on the use of biocompatible and environment-friendly materials such as plant materials, enzymes, and microorganisms (bacterial, fungal, and other microbial routes). In the biological synthesis methods, the extract of living organisms act as reducing/oxidizing, stabilizing, and capping agents for the synthesis of the nanoparticles [45, 142]. Among the available biological synthesis methods, plant-mediated synthesis is simple and an easy process to synthesize nanoparticles at large scale compared to microorganisms (e.g bacteria, yeast, and/or fungi) mediated synthesis. Plant material such as leaves, stems, flowers, and roots have a significant biochemical components such as phenolics, flavonoids, quinols, alkaloids, terpenoids, chlorophyll pigments and others which act as reducing, stabilizing, and capping agents to facilitate the formation of the nanoparticles [45, 46]. Huang *et.al* [202] explained that the existence of functional molecules such as, –C–O–,-C-O-H, -C-N-C, –C=C-, –C=O– etc, derived from plant material helps in the biosynthesis of the nanoparticles. To date, different plant families have been used such as solanum *lycopersicum* [203], *Stereum hirsutum* [204], *Tabernae montana* [205], *Rheum L* [206], *Aloe vera* [207], *Piper betle* [208], *Theobroma cacao* [209] etc., to synthesis CuO nanoparticles.

The Opuntia ficus indica commonly known as *cactus pear* belongs to the family of *Cactaceae* (see Fig.2.8.1.3). The distribution of this plant material in Tigray, northern Ethiopia is so large, and this tremendous existence of the plat material (*cactus pear*), and its rich phytochemistry attracted the researcher to study its extracts as a reducing/oxidizing and stabilizing agents for the preparation of CuO nanoparticles and Ag@CuO nanocomposites as SSA for solar-to-thermal application [46]. Generally, CuO nanoparticles are commonly synthesised from Cu (II) precursors or Cu substrates by using different methods with or without additives of reagents as summarized in Table 2.8.

Figure 2.8.1.3: Cactus pear plant

2.8.2 Fundamental properties of CuO

Understanding of the fundamental properties of CuO nanostructure is crucial to their synthesis and applications and a key to the rational design of CuO nanostructure-based functional devices. In this section, the fundamental properties of CuO nanostructures including crystal structure, optical property, spectral selectivity and vibrational properties are addressed.

2.8.2.1 Crystal structure and phase transitions of CuO

The structural phase of CuO was reported in 1933 by Tunnel and then developed using X ray method in 1970 [150, 210]. CuO has a black color and crystallizes a monoclinic phase structure with C^6_{2h} groups. The copper (Cu) atom is coordinated with four (4) oxygen (O) atoms at the corner of square planar configurations, which forms chains by shared edges [211] as illustrated in Fig. 2.8.2.1 below.
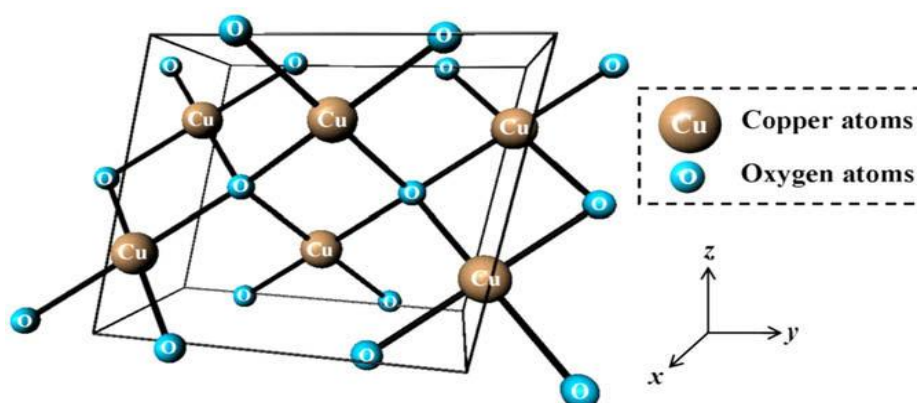
Figure 2.8.2.1 Monoclinic structure of CuO unit cell [212].

The Cu-O, O-O, and Cu-Cu bond length are 1.96, 2.62, and 2.90 ˚A, respectively and the lattice parameters are a = 4.6837 ˚A, b=3.4226˚A, c=5.1288 ˚A, x=99.54 ℃ and y=z=90º [138, 150]. X-ray diffraction (XRD) is the most common characterization technique to analyze the crystal structures and phases CuO. From XRD patterns, the particle size, lattice constants and lattice strain can be calculated from the Debye-Sherrer formula. According to Aparna *et.al* [211], elastic strains of CuO was analyzed from XRD patterns and revealed a high strain with smaller than 20 nm of CuO was observed. Table 2.8.2.1 summarizes some basic crystallography and physics constants of CuO.

Table 2.8.2.1 Crystallographic and some physics constants of CuO

Space group	C2/c(No 15)
Unit cell	a = 4.6837 ˚A
	b = 3.4226 ˚A
	c = 5.1288 ˚A
	β = 99.54º
	$\alpha = \gamma$ = 90º
Cell content	4CuO
Stable phase	Monoclinic
Bandgap energy(Eg)	1.26-1.90 eV
Density	6.515 g cm^{-3}
Distances	
Cu–O	1.96 ˚A
O–O	2.62 ˚A
Cu–Cu	2.90 ˚A
Melting point	1201˚C
Refractive index	1.4
Dielectric constant	18.1
Hole mobility	0.1-10 cm^2/vs

2.8.2.2 Optical properties

The optical property of CuO in the solar spectrum are dominated by absorption thresholds, which is determined by its band gap energy. CuO has lower band-gap value, which allows to absorb the incident light in the visible region strongly. The electronic bandgap is the difference between the top of the conduction band (CB) and that of the valence-band (VB) derived from the Cu 3d orbital. Compared with bulk CuO, the bandgap of nanostructured CuO is blue-shifted with lower band gaps (from 1.2 to 2.1 eV). Therefore, CuO absorbs strongly throughout the visible spectrum, with slight transparency for bigger band gap nanostructured samples which absorb in the UV region [138, 157]. In addition to the variation of the band gaps, the optical properties of nanostructured CuO is related to quantum dots (QDs) effects. The QDs occur due to the unique quantum confinement effects. When a photon energy is equal to or greater than the band gap of the absorber material or QDs, it excites an electron (e$^-$) from the VB to CB, simultaneously creating a positive hole (h$^+$) in its position. This leads to an electron-hole (e$^-$-h$^+$) pair called as an exciton. In a QDs, the average size of the exciton (the Bohr radius) is smaller than the size of the quantum dot, providing confinement energies as the exciton is squeezed into the materials. Notably, the optical bandgap of semiconductors can be calculated from the reflectance spectra by using Tauc's relations (2.8) [138, 211, 213].

$$(\alpha h v) = A(h v - E_g)^n \qquad (2.8)$$

where, A is constant, Eg is the optical bandgap of the material, hv is photon energy, α is the absorption coefficient and n is type of transition band. The absorption coefficient (α) is calculated using $\alpha d = \ln(1/T)$ relation, where T is the transmissivity and d is the length of the waves in centimetre [214]. Yang *et.al* [215] reported different shapes of nanostructure CuO by controlling the reaction parameters. The UV–visible absorbance spectra, and band-gap energy for each nanostructured CuO is reported in Fig.2.8.2.2. The calculated band gaps of flower, boat, plate, and ellipsoid-like structures of CuO were found to be 1.425, 1.429, 1.447, and 1.371 eV, respectively.
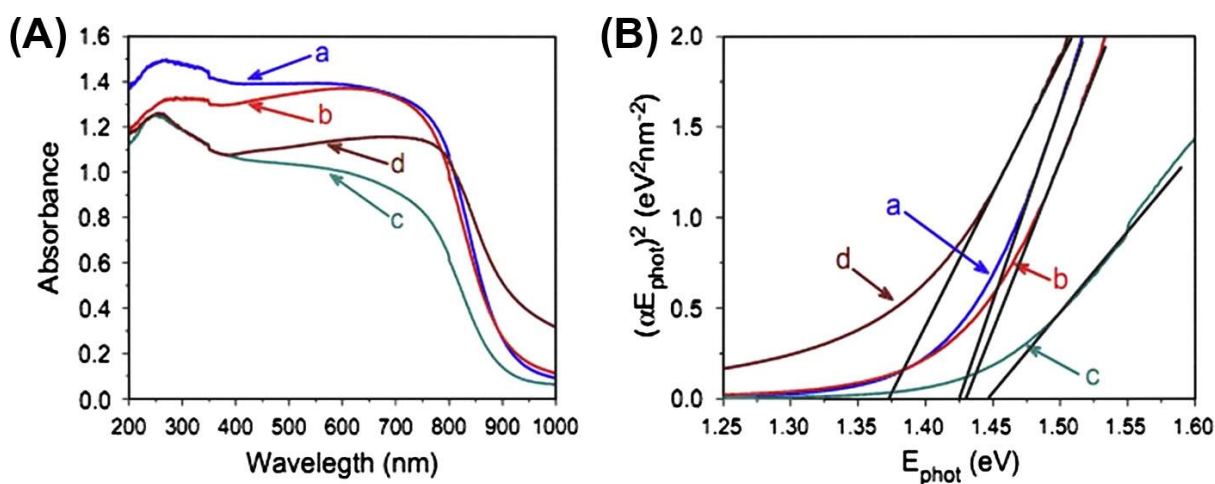
Figure 2.8.2.2: A) UV–Vis-NIR absorbance of (a) flower, (b) boat, (c) plate, and (d) ellipsoid-like structure of CuO, B) band gap values of CuO nanostructures [215].

In addition to absorption property of CuO by absorption techniques, photoluminescence (PL) spectroscopy is an important technique to study the electronic transitions including the band edge transitions. Several PL bands are reported for CuO which expands from UV to near IR region, however, most the peaks are in 400 to 600nm wavelength ranges. Deep level emissions in CuO is typically composed of green emissions (605nm), and near-yellow emissions (680nm). The green emission is attributed to the oxygen (O) vacancy or Cu-O antisite defects, and the yellow or red emissions relating to the interstitial defects of Cu metal ions in Cu-O [211]. Vila *et.al* [36] reported that PL bands appeared at 1.33, 1.23, and 1.11 eV in CuO nanoparticles and concluded that the emissions with higher energy were attributed to near band edge transitions in CuO while the other two emissions are from oxygen (O) vacancy, and oxygen on Cu antisite defects. The CuO have three emission bands at 305, 505, and 606 nm (see Fig.2.8.2.2.1(a)). The PL peak at 305nm is assigned to the band edge emission of nanostructured CuO. The peaks positioned at 489, 505, and 525nm are due to the defects in CuO. The bands extended from 585 to 625 nm are attributed to CuO deep-level

defects. The PL peak at 685 nm is caused by a CuO interstitial defect, whereas the peak at 714 nm is caused by electron-hole recombination (e^{-}-h^{+}) at O vacancies [216-218].
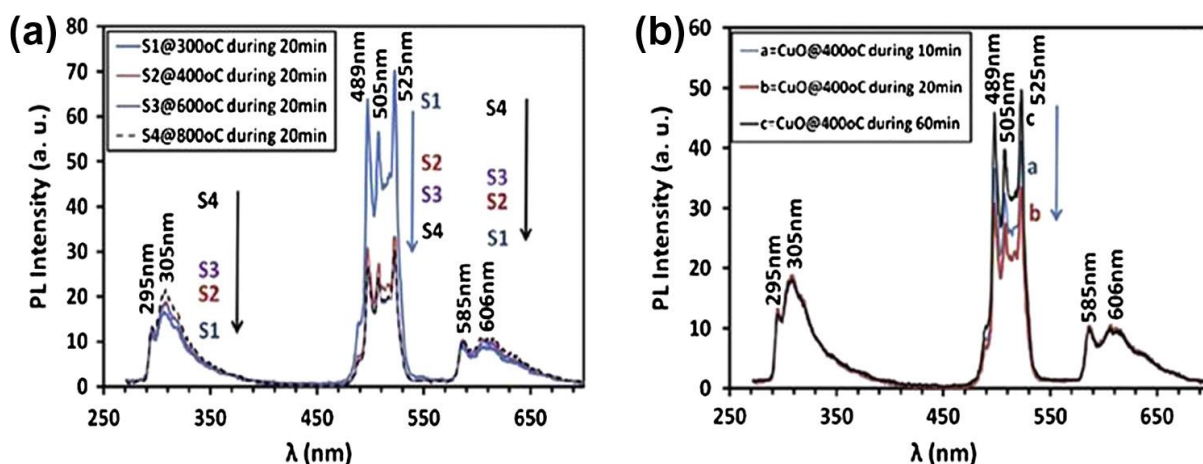
Figure 2.8.2.2.1: The PL spectra of CuO prepared via thermal decomposition [216]

Raman spectroscopy (RS) is also extensively employed to analyze the optical and vibrational properties of nanomaterials like CuO because of its sensitivity to the atomic arrangement and lattice vibration of the material. CuO with a monoclinic structural phase belongs to the C^{6}_{2h} symmetry with two molecules per primitive cells and has twelve optical phonon modes (i.e $4A_u + 5B_u + A_g + 2B_g$) in Raman spectrum; of these only three ($A_g + 2B_g$) are Raman active modes. For example, as shown in Fig.2.8.2.2.2, three Raman active peaks are observed at 288, 330, and 621 cm^{-1}. The peak at 288 cm^{-1} was allocated to the Ag mode, while the peaks at 330 and 621 cm^{-1} were assigned to the Bg mode [219-221].
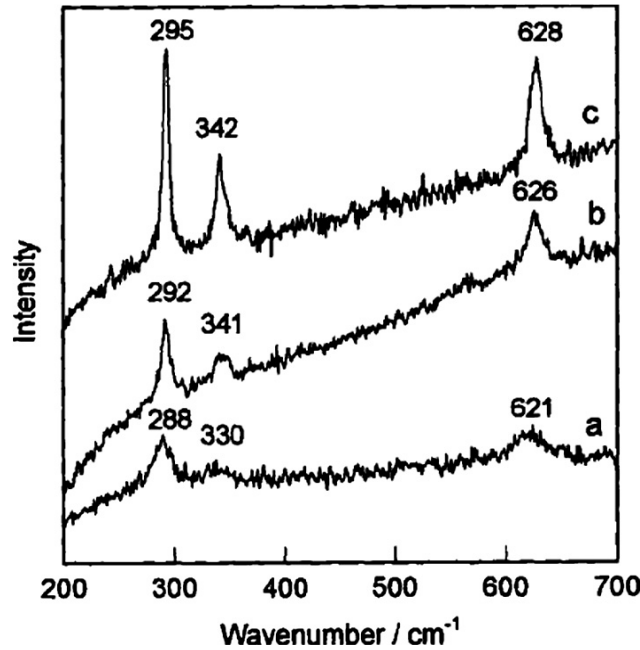
Figure 2.8.2.2: Raman spectra of CuO with a grain siz**e** of 10 nm (a), 30 nm (b) >100 nm (c) [221].

2.8.2.3 Vibrational properties

Raman, infrared (IR), and PL spectroscopy were used to investigate the lattice dynamics of CuO materials and provide on the nature of the electron-phonon interactions and also revealed details about spin-phonons interactions and electron-phonons scatterings. Debbichi *et.al* [222] described the vibrational property of Cu-O by using Raman spectroscopy and clearly identified the existing vibrational modes in CuO. Shih *et.al* [223] demonstrated size effect of spin-phonons coupling in nanostructure CuO and concluded that the spin-phonons mode varies with the size of nanowire CuO due to the strengthened coupling. The infrared modes are related with the relative motion of both Cu and O atoms which consists of O-Cu-O stretching vibrations and bending modes [224].

2.8.2.4 Spectral selectivity of CuO for solar to thermal energy

Metal oxide (MO) semiconductors have good intrinsic properties and/or selectivity due to their transparency for photons with energy below their optical band gap, but absorbed for energy above the optical bandgap energy. In principle, solar absorber surfaces are expected to have a very low band gap to achieve light absorption in the solar spectrum region. Practically the excited electrons return to the ground state after the absorber surface absorbs incident light through radiative or non-radiative transitions to produce thermal energy or heat [32-34]. As aforementioned, CuO is a p-type semiconductor with lower bandgap values of 1.2–1.9 eV that allows to have high broadband absorption in solar radiation. CuO is a good solar

selective absorber (SSA) material due to its intrinsic as well as selectivity properties, which helps to absorb the incoming radiation in the UV-Vis-NIR region, and high reflectance in the far IR region [6, 51, 56, 77, 78, 138, 172]. Spectrally selective CuO as SSA has been studied by using different coating techniques [51-54]. S.Karthick *et.al* [40] reported that CuO nanocoatings on Cu substrates as SSA using NaOH, and NH_4OH aqueous solution and achieved absorptance (α) of 0.90 and emissivity(ε) of 0.07 in 0.3-2.0 µm wavelengths range. S.Kumar *et.al* [225] demonstrated nanostructure CuO thin films selective solar absorber via sputtering, and reported (α=0.71) and (ε=0.07). X. Zhang *et.al* [226] also prepared CuO thin films via chemical oxidation as selective solar absorber on Cu substrate in alkaline solution (KOH and K_2S_2O8). He *et.al* [41] reported Ag@CuO nanocomposite film as a novel SSA via the one step sol-gel method and achieved a solar absorptivity of α=0.85 and emissivity of ε=0.05, and solar absorptivity was improved to 0.917, after the antireflection was added while the emissivity remained unaltered**.**

2.8.3 Application of copper oxide

Different transition metal oxides (MOs) have attracted much attention in the fundamentals, applied researches, and applications in the field of biology, chemistry, medicine, physics, and electronics. Due to the large surface area to volume ratio of the NPs provide novel functions in various practical applications. Among the transition MOs, CuO films with large surface area-to-volume ratio exhibits superior physical and chemical properties and have been widely studied because of their potential applications in various fields [15, 175-177, 227]. This section focused on the recent developments in the different CuO nanostructures as building blocks for applications in a wide range of fields, include Lithium-ion batteries (LIBs), supercapacitors, sensors, solar cells, field emissions, photocatalysis, photothermal and biomedical.

2.8.3.1 Application in Lithium-ion batteries (LIBs)

The surging demand for LIBs with capability to deliver increased energy aroused great interest in developing novel negative electrodes with high rate performance and good cycling stabilities. Transition MOs with environmentally friendly and high theoretical capacity have been a potential candidate(s) for LIBs. Among transition MOs, CuO is considered as a promising material for developing negative electrodes for LIBs due to its low-cost, easy preparation, chemical stability, environmental friendliness and high theoretic capacity [138, 228]. Fig.2.8.3.1 illustrates LIB and electrochemical processes during charge-discharge.
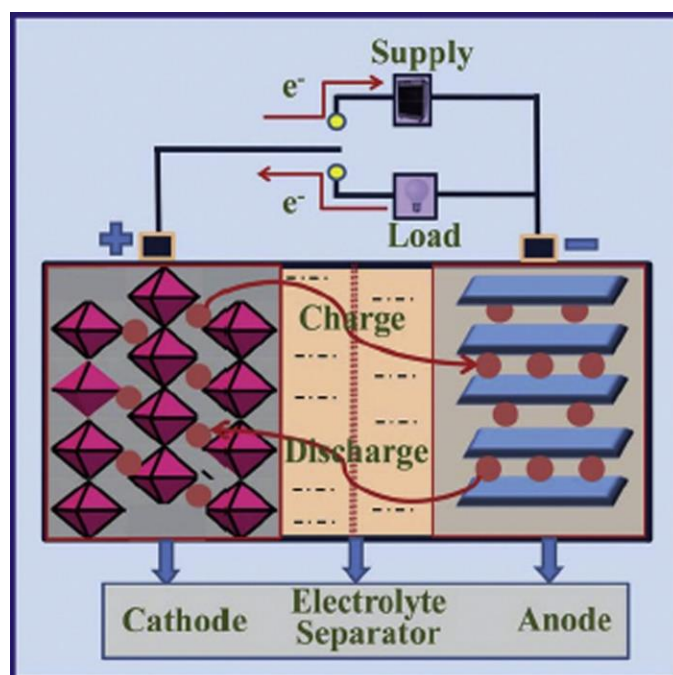
Figure 2.8.3.1: Illustration of LIB and electrochemical processes [228].

For example, F. Wang *et.al* [229] demonstrated that CuO dumbbell and sphere-like structures can be synthesized via chemical solution methods and annealing treatment approaches. The morphological surface of the samples is affected by the reaction temperature, and the dumbbell and sphere-like structure of CuO are used for LIBs, evidencing good rate capabilities of 569 mAh/g and 467 mAh/g at 5 $^{\circ}$C and high cycling stability of 680 and 601 mAh/g for dumbbell, and sphere-like structure of CuO over 400 cycles at 2°C, respectively. Yang *et.al* [230], reported the fabrication of CuO nanoflakes on Cu foam substrates for LIB-negative electrodes, showing excellent rate performances and stable reversible capacities. L. Feng *et.al* [231] reported CuO@Ag core-shell structured nanocomposites by simple chemical reduction method. Ag shell was coated onto the surface of CuO to improve the cycle stability of CuO, and the results confirm that CuO@Ag nanocomposite revealed the best electrochemical response. The specific capacity of Ag@CuO composite reached 420 mAh/g which is higher than 138 mAh/g of CuO at current density of 0.2C. Anjian *et.al* [232] successfully synthesized hollow porous CuO@C nanorods by coordination reaction of $[Cu(NH_3)_4]^{2+}$ with benzenetri-carboxylic acid (H$_3$BTC) under ultrasound irradiation and calcining at a temperature of 250 $^{\circ}$C in air. The specific capacities of CuO@C were 505

44

mAh/g which is higher than of 250 mAh/g, and 192.3 mAh/g at a current density of 100 mA/g calcined at 300 and 350 °C in air, respectively.

2.8.3.2 Application in solar cells and light-emitting diodes

The need for clean, renewable and environment-friendly energy sources has increased interest in the development of solar conversion applications. Copper oxide (CuO) coatings are potential candidates for developing various optical devices, including solar cells and light emitting diodes (LEDs). As aforementioned CuO is an intrinsic p-type semiconductor and produced with low cost for efficient photovoltaic applications, especially for perovskite solar cells (PSCs). Inorganic materials like CuO are explored to be good candidates as hole transport layers (HTLs) due to their intrinsic properties. Compared to organic HTL, inorganic p-type materials generally possess good chemical stabilities, high hole mobility, and ease of preparation for solar cell applications [224, 233]. Fig.2.8.3.2(a,b) illustrates typical device structures of solar cells and LEDs, respectively. Bian *et.al* [234] demonstrated solution processed CuO thin films as HTL in the inverted planar PSCs and concluded that CuO thin films showed higher performance than organic device with PEDOT:PSS layer. Sun *et.al* [235] proposed CuO as HTL in inverted planar (p-i-n) PSCs, and achieved a power conversion efficiency (PCE) of 17.1% with open circuit voltage (Voc) of 0.99 V, short circuit current densities (Jsc) of 23.2 mA/cm^2 and a fill factors (FF) of 0.74.
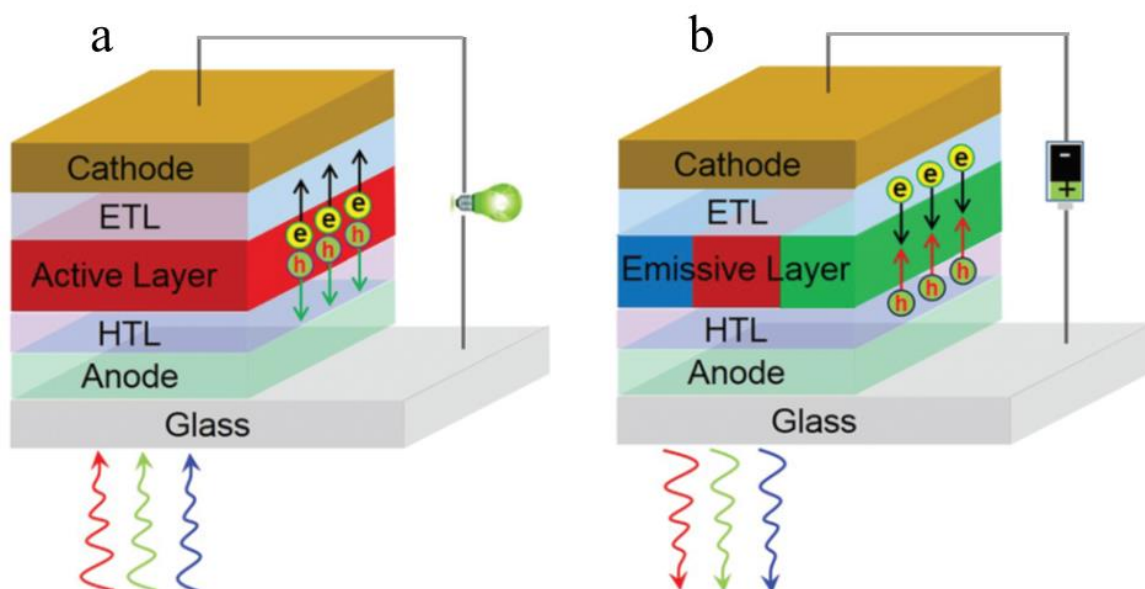
Figure 2.8.3.2 Typical device structures of (a) solar cells, and (b) LEDs.

LEDs are devices that produce non-coherent and narrow-spectrum light when voltage is applied. The charge generation layers are typically studied for tandem LEDs using small

molecule organic layers or organic light-emitted diodes (OLEDs). OLEDs are characterized by low drive voltages, brightness, full-colour emissions, and easy of processing of thin-film devices. The energy level alignment between HOMO level of HTL and LUMO level of ETL is an essential component for efficient charge generation. Compared to organic molecules, metal oxides (MOs) HTLs have the advantages such as good air stability, high carrier mobilities and solution processabilities. The OLEDs involve an injection of charges from the anode and cathode into emissive layer(EL), transport of charge carriers via the emissive layers (ELs), exothermic recombination of HTLs, and ETLs to generate excited states of electrons known as excitons, followed by their deactivations of emissions of fluorescence [236-238] as seen in Fig.2.8.3.2 (b). Xiao Sun *et.al* [126] solution-processed CuO thin films are introduced as HIL for LEDs. The optimized CuO-based LEDs revealed external quantum efficiencies (EQEs) of 5.37% with a maximum brightness over 70,000 cd/m^2. Zheng, and Zhen [239] fabricated CuO/Cu as buffer layer in OLED by inserting it between ITO and HTL. The CuOx/Cu limits the current operating densities while brightness and efficiencies are improved. The maximum brightness of the device was over 14 000 cd/m^2 at 3 cd/A current efficiency.

2.8.3.3 Application in supercapacitors

One type of supercapacitor that has received a lot of attention as an efficient energy storage device is the pseudo-capacitor, which involves the passage of charges across a double layer, resulting in faradaic current passing via supercapacitor cells. Copper oxide (CuO) is established as technologically important for high-energy supercapacitors to meet the rising demands for efficient electrochemical energy storage systems due to its favourable pseudocapacitive characteristics [211, 240]. Zhang *et.al* [241] reported the electrochemical property of CuO NPs with different morphological surfaces synthesised via chemical precipitations as electrode material in supercapacitors and reported higher specific capacitances of CuO NPs at a current density of 10 mA/cm^2.
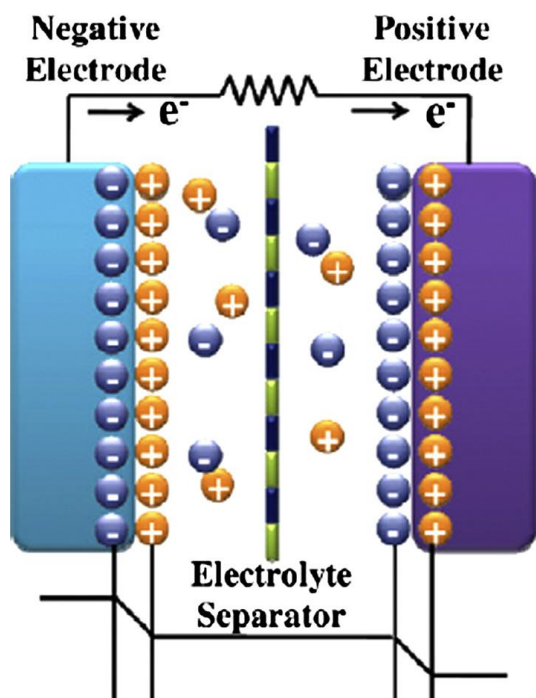
Figure 2.8.3.3; Schematic diagram of the pseudo-capacitor [242]

Zhang *et.al* [49] synthesised cauliflower-like, nanobelt-like, and feather-like CuO NPs through chemical deposition. They reported that morphological surfaces of nanostructure CuO can influence the electrochemical properties and the cauliflower-like structure of CuO showed higher specific capacitances (115.3 Fg^{-1}). J. Sackey *et.al* [243] reported the electrochemical performance of CuO NPs via biosynthesis method and the obtained CuO nanoparticles exhibited maximum specific capacitance values of 39.45 mF/cm^2 at a scan rate of 20 mV/s. This confirmed that plant material-mediated CuO nanoparticles is promising for electrochemical energy storage applications.

2.8.3.4 Application in photocatalysis

Organic dyes and heavy metals are commonly used in industrial processes and are components of industrial wastewater. Degradation and removal have been a source of concern around the world due to the potential toxicities and visibilities in surface water areas. Photocatalysis has been recognized as a green energy conversion technology to degrade many organic dye pollutants by using light absorber semiconductors. CuO is a promising photocatalyst used in various chemical processes for the degradation of contaminated organic dyes under visible light irradiations due to its narrow bandgap and environmental friendliness. Hydrogen peroxide (H_2O_2) is frequently added to enhance the photo-catalytic property of CuO for the degradation of dye pollutants due to its electronic structures is

characterized by a filled valence bond (VB) and an empty conduction bond (CB), which plays a significant role in the photo-catalytic process [244, 245]. When the photocatalyst CuO absorbs photons higher energy electron (e^-) in the VB can excite to the CB, with simultaneous creation of holes (h^+) in the VB. The electron-hole (e^--h^+) pairs induced by light excitation will accelerate surface redox reactions for the structural destruction of toxic pollutants. The e^--h^+ pairs can be captured by hydrogen peroxide (H_2O_2), leading to radical oxidant formations ($\cdot OH$, $\cdot OOH$, and $\cdot O^{-2}$), and these oxidant radicals react with the organic dye (R) to produce intermediates. These intermediates include radicals and radical cations to achieve complete mineralizations with the formations of CO_2, H_2O [138, 246] as illustrated in Fig.2.8.3.4.
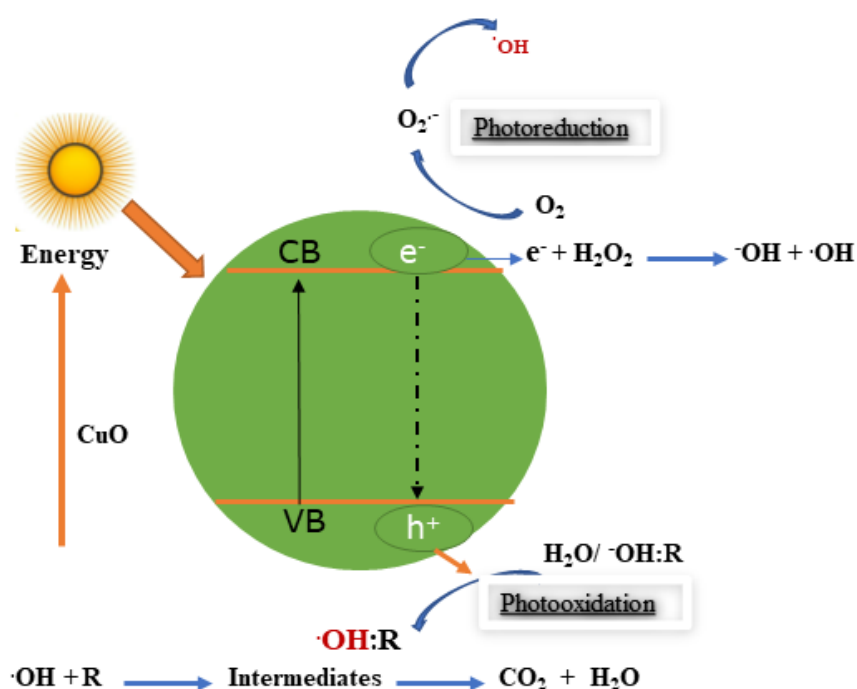
Figure 2.8.3.4: Schematic illustration of photocatalysis process [244]

Sun *et.al* [247] reported that 3D structure of CuO spindles exhibits higher photocatalyst degradation of Rhodamine B (RhB) than 2D structured CuO plates and the degradation efficiencies was 72.5%, and 51.9% for CuO spindles, and CuO plates, respectively. Yao *et.al* [248] observed that CuO exhibits high photocatalysis towards oxalic acid solution which is a pollutant in industrial wastewater and is a powerful reducing agent [224, 249]. Nillohit M *et.al* [250] also reported hierarchical CuO thin films on FTO by using deposition and thermal oxidation methods for photocatalysis of organic dyes such as Methylene Blue (MB), Rhodamine (RhB), and Congo Red (CR). In the presence of visible light irradiation, very feeble mineralization or high degradation was observed, and the intensity of the absorption

for RhB (λmax ~ 554 nm), CR (λmax ~ 500 nm), MB (λmax ~660 nm) was found to decrease with time.

2.8.3.5 Application in photothermal energy

The photo-thermal conversion process is an important pathway to convert the incident solar radiation into heat and then to electricity via thermophotovoltaic technologies [5, 6] and has proven its performance in the production of clean, secured, environment friendly and low-cost energy. The harvested thermal energy has a potential application for domestic heating water, refrigeration, space heating and cooling, catalytic production of fuels and chemicals, seawater desalination, distillation, industrial process, environmental purification, and thermal power generation [4, 9, 33, 172, 251]. So far, CuO thin films as a spectrally selective absorber for solar-to-thermal conversion has been achieved by using different techniques such as spraying, spin coating, sol-gel, thermal oxidization, chemical conversion method, electrophoretic-deposition, chemical oxidation, D.C. Magnetron sputtering, cathodic arc deposition, and chemical vapour deposition (CVD) on different metallic [30, 51-57]. Hottel and Unger [55] reported CuO coatings as SSA on flat plate collectors by spraying a dilute solution of $Cu(NO_3)_2.6H_2O$ onto an aluminium (Al) sheet and then converted to black CuO by heating it above 170 ^{o}C and revealed α=0.93 and ε=0.11. Table 2.8.3.5 summarises CuO-based SSA coatings reported for solar-to-thermal conversion.

Table 2.8.3.5 Summarise reports of CuO based coatings for photothermal applications

Reference(s)	Year	Coating type	Concepts	Optical response	
				α-value	ε-value
G. Toquer *et.al* [252]	2019	CuO	The tandem CuO nanofilm is deposited onto silicon wafer via electrophoretic-deposition (EPD) by varying the EPD parameters to control surface morphology and thickness of the obtained CuO film in order to optimize the final optical property.	97%	>14%
S. Murugesan *et.al* [30]	2014	CuO	Nanostructured CuO thin films (nanofibers, and nanoneedles) with one dimensional (1D) were prepared via chemical oxidation on Cu substrate by varying NaOH concentration in the reaction medium.	86-90%	6-8%
G. Xu *et.al* [51]	2011	CuO	CuO thin films as SSA were conveniently prepared on Cu substrate by immersed in chemical solutions and the coatings surface was changed from square-like to porous belt-like structures with the of reaction time.	94%	16%
P. Amezaga *et.al* [253]	2020	CuO-Co$_2$O$_4$ /Al$_x$O$_y$	CuO-Co$_2$O$_4$ based thin films were synthesized on SS substrate as SSA coatings via aerosol-assisted CVD techniques at different deposition temperatures.	92%	14%
S.Kim *et.al* [172]	2017	CuO	CuO nanostructured as SSA was prepared on Cu substrate by dipped into the alkali-solution composed of NaOH, NaClO$_2$, Na$_3$PO$_4$.12H$_2$O and water at 95 ºC by varying the reaction stages.	87-95 %	11-14%
C. Barshilia *et.al* [42]	2019	CuO	CuO films were deposited using reactive magnetron sputtering on glass, Cu, and Si substrates. Both sputtering time and oxygen flow rate showed a significant effect on the optical property of the films	95%	52%
A.Ma´rquez *et.al* [254]	2004	CuO	CuO coatings produced by using a dc cathodic arc technique. During the deposition, the substrates were exposed into different discharge potential.	93%	16%
Barrera *et.al* [91]	2008	CuO-SiO$_2$	CuO-silica composite films were fabricated by sol-gel method using ethanolic solution of tetraethoxysilane/ tetraethyl orthosilicate (TEOS) and copper-propionate solution on SS substrate using dipping process and then the final film was annealed at 450 ºC in air for 4 hrs.	92%	20%
G. Toquer *et.al* [255]	2017	CuO nanoparticles	CuO NPs were investigated by using cathodic electrophoretic deposition (EPD) for photothermal absorber.	80%	12%
He *et.al* [41]	2016	Ag@CuO/Al$_2$O$_3$	Ag–CuO nanocomposite film as a novel SSA via the one step sol-gel method from copper acetate, and copper nitrates.	91%	5%

2.8.3.6 Application in sensors

Semiconducting MO nanomaterials have been reported widely for sensor applications owing to their semiconducting nature and active surface. Among these oxides, CuO as a p-type semiconductor offers great potential for optical, gas, and biosensors [138, 256]. CuO coatings have been confirmed to be highly sensitive towards various gases, including ethanol (C_2H_5OH), carbon monoxide (CO), and Hydrogen sulfide (H_2S) [224, 257, 258]. H_2S is one of the hazardous and toxic gas explained by the smell of rotten eggs. Naturally, it is produced in natural gas, crude petroleum, foods, and also by the bacterial breakdown of animal and human wastes. The health effects of H_2S gas depend on the duration of exposure and its concentration. Low H_2S concentrations can cause various serious health problems, including eye and throat damage, poor memory, dizziness, and loss of balance and reasoning [259]. Y.E. Greish *et.al* [259] fabricated CuO NPs embedded in a glycerol ionic liquid-doped chitosan to prepare organic-inorganic nanocomposites (CSIL-CuO) and tested against H_2S gas with reference to time at different H_2S gas concentrations and reaction temperature. The fabricated sensor membrane exhibited a fast response (i.e, 14 s), and good sensitivities (15 ppm) towards H_2S gas at 40 °C of temperature.

Moreover, semiconductor CuO coating also shows significant sensitivity for the detection of toxic organic molecules. Glucose is one organic molecule used in the human body to generate energy. However, high levels of glucose in the blood is linked to a number of diseases. Because of their electrochemical activity and transfer electrons at lower over-potentials, CuO can detect glucose concentrations. Non-enzymatic detection of glucose by CuO-based sensors has proven to be more advantageous than enzymatic detection by enzymatic sensors [260-262]. Sahoo *et.al* [263] fabricated nanoribbons CuO for glucose detection via hydrothermal, and microwave methods and concluded that the faceted CuO were more efficient for nonenzymatic glucose sensing compared to non-faceted CuO. S. Kima *et.al* [264] also demonstrated CuO rose-like nanostructures for glucose chemical sensing applications via hydrothermal at low temperatures and showed a very high sensitivity of 4.640 μA mM^{-1} cm^{-2}.

2.8.3.7 Application in biomedicals

Recently, the field of nanoscience research has exponentially increased for a wide range of applications such as biosensing, diagnosis, imaging, and therapies. Metal oxide (MO) NPs such as CuO have gained attention mostly from the scientific communities in many biomedical applications. Copper (Cu) is an essential trace element for humans, plants, as well

as animals and is needed in a minimal amount for humans. CuO nanoparticles have been efficiently used for sensing and in many biomedical applications [264-266]. Goyal *et.al* [267] also studied the antimicrobial properties of CuO nanoparticles depend on the surface and size of nanoparticles. He confirmed that small CuO nanoparticles with a large surface area have better antibacterial activities than the larger ones. CuO nanoparticles also exhibited antimicrobial activity against B. subtilis bacteria. Kalilur *et.al* [268] biosynthesized CuO nanoparticles to evaluate the antioxidant activities as well as cytotoxicity against four cancer cells (human breast, cervical, epithelioma, lung) and concluded that biosynthesized exhibited higher antioxidant and cytotoxicity than those produced via chemical method. G. Sharmila *et.al* [269] demonstrated biosynthesis of CuO nanoparticles using *Bauhinia tomentosa* leaf extracts for antimicrobial activities. The biosynthesized nanoparticles exhibited an excellent antibacterial activity against gram negative of *E. coli* (22 mm)*, and P. aeruginosa* (17 mm).

CHAPTER THREE

SYNTHESIS METHODOLOGIES AND CHARACTERIZATION TECHNIQUES

3.1 Synthesis methodologies

The development of synthetic methods is widely recognized as a critical component in understanding and applying nanoscale materials. It allows to modulate different parameters such as morphology, particle size, size distributions and composition [157, 158]. In this investigation the green synthesis, eletrodeposition and sputhering techniques were employed to prepare different CuO nanostructure surfaces and its plasmonic nanocomposites.

3.1.1   Green synthesis method

Green synthesis refers to the synthesis of different nanoparticles using bioactive agents such as plant materials, microorganisms and various biowastes. In the biological synthesis methods, the extract of living organisms act as reducing/oxidizing, stabilizing, and capping agents for the synthesis of the nanoparticles [45, 142]. Herein, CuO nanoparticles and Ag@CuO nanocomposites were synthesised using green synthesis (i.e., *Cactus* extracts) and spin-coated on a stainless steel (SS) substrate for solar-to-thermal energy conversion.

3.1.1.1 Materials and chemicals

Methanol (CH_3OH, 99.8%, Sigma Andrich, Saint Louis, USA), Isopropanol ($H_3CCHOHCH_3$, 96%, Sigma Andrich, Cologne, Germany), trichloroethylene ($C_2H_2Cl_2$, 99.5%, Saint Louis, USA), Copper nitrate trihydrate ($Cu(NO_3)_2.3H_2O$, 99.99%, Sigma Andrich, Cologne, Germany, Germany), Silver nitrate ($AgNO_3$, 99.99%, Sigma Andrich, Cologne, Germany), Potassium peroxydisulphate ($K_2S_2O_8$, 99.8% Sigma Andrich, Darmstadt, Germany), Potassium hydroxide (KOH, 99.95% Sigma Andrich, Darmstadt, Germany), Copper target, (Cu, 99.99%, Sigma Andrich, Saint Louis, USA), Stainless steel (SS) (1.5cm ×1.5cm ×1mm, Saint Sigma Andrich, Saint Louis, USA) substrates, Electronic balance (E-Metter, Zurich, Switzerland), Ultrasonic-bath (1510C-MTH, Mexico, Mexico), Hot-plate (Coring, PC-420D, Vietnam), Spin-coater (WS-400-6NPP-Lite, PA, USA), Oven (Thermo-scientific, PR305225M, Twinsburg, USA) and Radio frequency (RF) sputtering (VST Sputtering Machine, Telavi, Israel) were used for preparing the samples. All reagents were analytical grade and were used without further purification. All solutions were prepared with high-purity of de-ionized (DI) water.

3.1.1.2 Plant preparation and extraction

The *cactus* pear (Opuntia ficus indica) was freshly collected from eastern Tigray, Ethiopia. Initially the *cactus pear* was washed using tap water and then deionized water to remove dust and contaminants present on the surface. Small pieces of *cactus* pear were dried in an oven at 60 °C for 12 h, and then ground using an electric blender. In this procedure, 10 g of the cactus powder was added to 200 mL de-ionized water, and the mixture solution was heated at 80 °C for an hour under a constant magnetic stirrer. The solution was cooled, filtered using Whatman (№ 1) paper, and then kept in a refrigerator at 5 °C until further use.

3.1.1.3 Green synthesis of copper oxide (CuO) nanoparticles

For green synthesis of CuO nanoparticles, cactus pear extract was used as a chelating and stabilizing agent [45]. In a typical procedure, 100 mL of cactus pear extract was mixed with 300 ml of 5 mM cupric nitrate trihydrate ($Cu(NO_3)_2.3H_2O$) solution and the reaction mixture was heated at 100 °C for 7-8 h under vigorous stirring until a brownish black color precipitate was formed. The obtained product was centrifuged at 4000 rpm for 30 minutes and thoroughly washed reputedly with de-ionized water, and then dried at 100 °C in the oven for 1 h. Finally, the dried sample was thermally oxidized at 420 °C in a furnace and stored in a tight container at room temperature for further use.

3.1.1.4 Deposition of thin films

The green synthesized CuO nanoparticles were deposited on SS substrate using a spin coater. Prior to the deposition, the SS substrates were cleaned by sonicating while dipped in acetone, isopropanol, and deionized water for 15 minutes each and then dried under nitrogen flow. The suspension solution was prepared by adding of 0.25 g of CuO in 1.5 mL of distilled water and stirred for 1 h. In the spin-coating procedure, a vacuumed spin-coater was used to deposit the prepared CuO suspension solution on SS substrates, and then 50 μL of suspension was spin-coated at 700, 800, 900, and 1000 rpm for 15 seconds; subsequently, the deposited CuO coatings were dried in a vacuum oven at 80 °C for 2h. Fig.3.1.1.4 illustrates the overall green synthesis and deposition procedure of CuO nanocoating on SS for SSA applications.
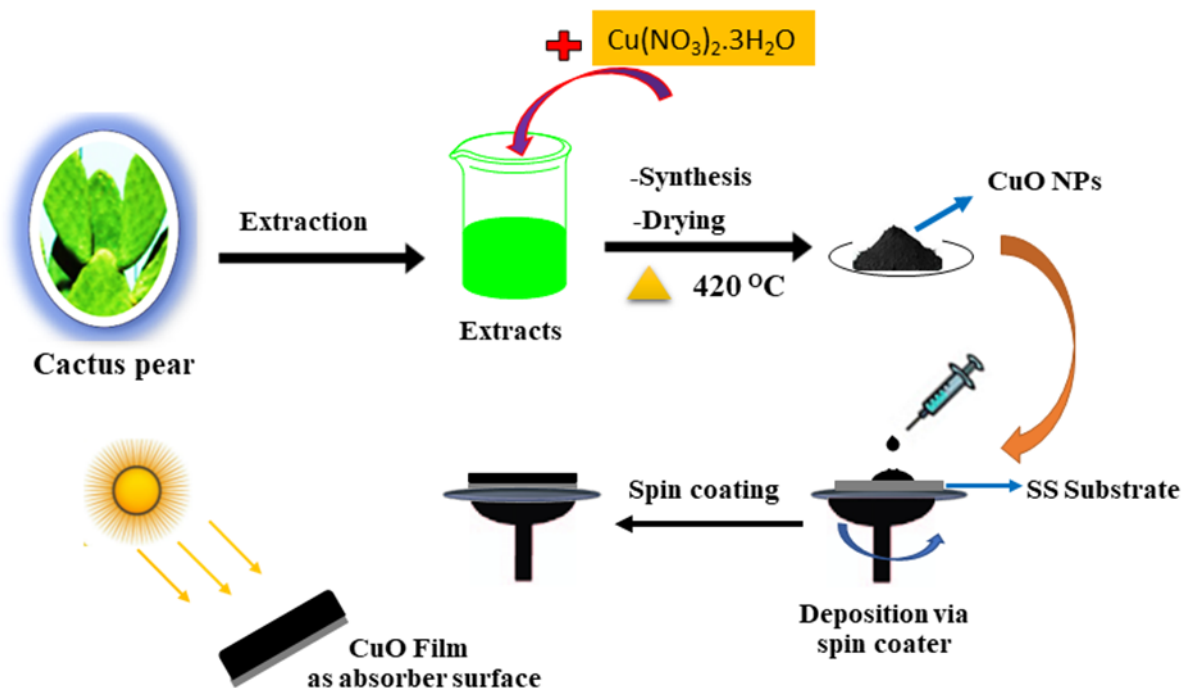
Figure 3.1.1.4 Schematic illustration of green synthesis, and deposition process of CuO nanocoating as absorber surface

3.1.1.5 Green synthesis of Ag@CuO nanocermet

In green synthesis of Ag@CuO nanocomposites, 10 mL of cactus pear extract was mixed with 40 mL of 1 mM AgNO₃ aqueous solution and stirred for 10 min until a dark brown color was observed, which indicated that the reduction of Ag^+ to Ag^0 or the formation Ag nanoparticles in a mixture [270]. Subsequently, 0.5gm of CuO nanoparticles in 2 mL dispersion solution was added into the reaction mixture and then kept under vigorous stirring for 2 h at room temperature. The suspension mixture solution was centrifuged at 4000 rpm for 30 minutes and washed repeatedly using deionized water to remove impurities. Finally, the obtained solid powder was dried in a vacuum oven at 60 °C for 2 h.

3.1.1.6 Deposition of Ag@CuO thin films

The green synthesized Ag@CuO nanocermet were deposited on SS substrate using a spin-coater technique. Before the deposition, the SS substrates were cleaned by sonicating while dipped in acetone, isopropanol and distilled water for 15 minutes each. The cleaned SS substrates were dried under nitrogen flow and then used for Ag@CuO nanocermet deposition. The suspension solution was prepared by adding 0.25g of Ag@CuO nanocomposite to 1.5 mL of deionized water and stirred for 1h. In the spin-coating procedure, a vacuumed spin-coater was used to deposit the prepared Ag@CuO suspension solution on

55

SS substrates. Then, 50 µL of suspension was spin-coated at 700, 800, 900, and 1000 rpm for 15 seconds. Subsequently, the deposited Ag@CuO nanocermet coatings were dried in vacuum oven at 80 °C for 2h. Fig.3.1.5 illustrates the green synthesis and deposition process of Ag@CuO nanocermet as solar absorber.
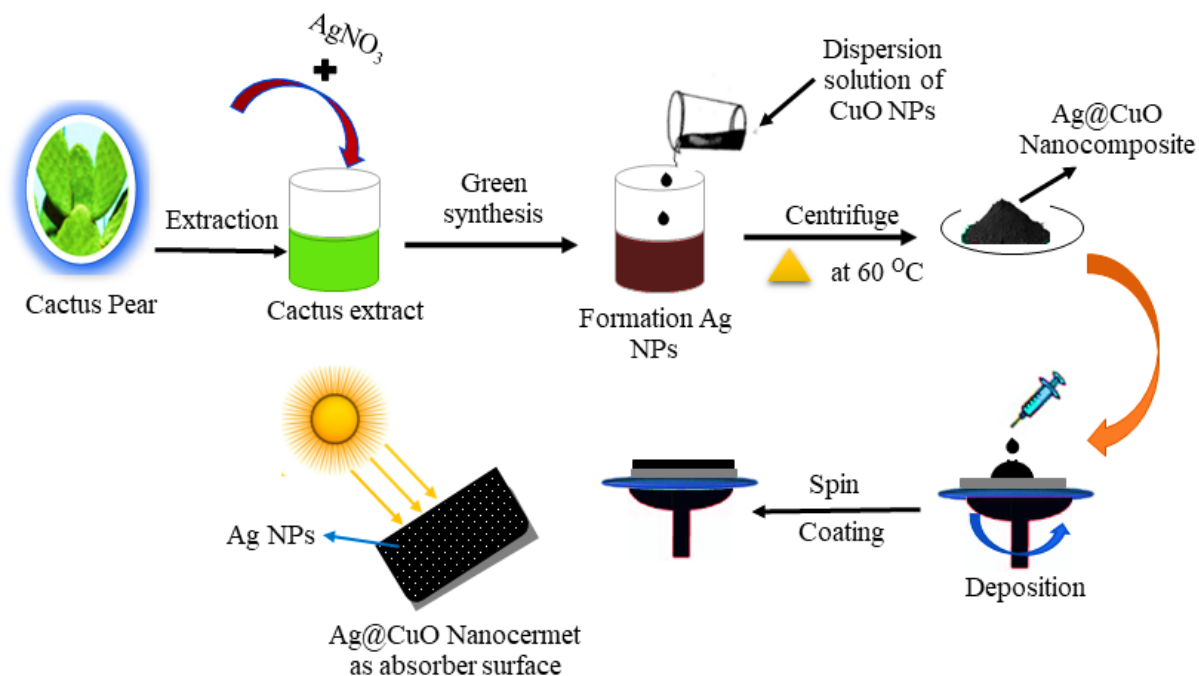
Figure 3.1.1.5 Schematic illustration of green synthesis and deposition process of Ag@CuO nanocermet as absorber surface

3.1.2 Electrochemical deposition method

3.1.2.1 Fabrication of nanostructure CuO nanocoatings

Nanostructure CuO coatings were prepared on SS substrate (1.5 cm x 1.5 cm x 1mm) via combined procedures of electrochemical deposition and thermal oxidation. Prior to deposition of the Cu thin films, the SS substrates were cleaned by ultrasonicating while dipped in distilled water, acetone, and isopropanol for 15 minutes each. Growth of the Cu thin films on SS substrates were carried out by using three-electrode configuration equipped with a saturated calomel electrode (Ag/AgCl) which served as a reference electrode (RE), Platinum (Pt) plate as a counter electrode (CE), and SS substrates as a working electrode (WE). The Pt plate and Ag/AgCl were immersed into the electrolyte solution and both connected to the potentiostat with a cathodic voltage of 1.0 V. Firstly, 0.25 M of $Cu(NO_3)_2.3H_2O$ solution as electrolyte was prepared and pH of the solution was 2.4. The cleaned WE or SS substrate was immersed into the electrolyte ($Cu(NO_3)_2.3H_2O$) solution. During the deposition the solution was stirred using Argon (Ar) gas. The Cu thin films were

electrochemically deposited on the surfaces of the WE or SS substrate at room temperature from an electrolyte solution at 15, 20, and 25 min deposition time, and then dried at 60 °C for 1 h. Finally, the dried Cu thin films were annealed at 420 °C for 2 h in a furnace to form nanostructured CuO coatings. Finally, a nano profilometer (Nanomap, Bruker) was used to measure the thickness of coatings.

3.1.3 Sputtering deposition method

3.1.3.1 Deposition of films by RF Sputtering

The target Cu metal with a diameter of 6 cm was used to deposit Cu films using RF sputtering on SS substrates in the presence of Argon (Ar) gas at 100W power. Prior to deposition, the substrates were cleaned using distilled water, acetone, and isopropanol for 15 minutes each. Argon (Ar) gas sputtering was used to clean Cu target 15 min. The distance between the sputtering Cu target and substrate was fixed at 10 cm and then the Cu target was cleaned using Ar gas for 15 min before deposition. The base pressure and RF sputtering were, respectively fixed at 1.50×10^{-1}, and 1.0×10^{-1} (Torr). During sputtering Cu thin films at room temperature, the flow rate of Ar gas was 20 standard cubic centimetres per minute (sccm). The substrate was rotated at 25 rpm to confirm uniform thickness. The thickness of the Cu coatings was controlled by deposition time (at 1.00, 1.15, 1.30, and 1.45 h).

3.1.3.2 Preparation of CuO nanocoating

The deposited SS/Cu films were chemically oxidized into CuO by immersing in an alkaline aqueous solution (i.e in 100 mL 2.25 M of potassium hydroxide (KOH), and 0.060 M potassium per sulphite ($K_2S_2O_8$) for 30 min at room temperature. The prepared CuO nanocoatings were thoroughly rinsed with distilled water and then finally dried in vacuum oven at 100 ºC for 1 h.

3.2 Characterization techniques

The term characterization refers to the general concept, and broad processes in which the properties of the material are explored, this is fundamental for scientific understanding of the materials. The size, composition, and structure of materials depend on the preparation procedure, reaction concentration, temperature, solvent condition, reaction time, and so on. Characterization techniques are the most important aspects in material science to determine the morphological, composition, structure as well as optical properties, and also various physical, chemical, electrical, and magnetic properties of materials. Nanoscale materials have a large surface-area-to-volume ratio compared to their bulk counterparts. For instance, 2 nm particles may have different optical, electronic, and surface properties than 10 nm particles, and also, the surface functionality of NPs may exhibit different properties than the corresponding bulk particles [45, 252, 271, 272].

This section will be focused on theoretical, and practical description of widely used and effective techniques employed to characterize the prepared CuO-based coatings for photothermal applications. In most cases, the widely used characterization techniques are categorised into microscopic-based techniques (i.e scanning electron microscopy (SEM), Atomic force microscopy (AFM) and energy dispersive X-ray spectroscopy (EDS)), spectroscopy-based techniques (i.e ultraviolet-visible near-infrared (UV–VIS–NIR) spectroscopy, and Fourier-transform infrared spectroscopy (IR), Raman spectroscopy, Rutherford backscattering spectrometry (RBS)), and X-ray-based techniques (i.e X-ray diffraction (XRD), and X-Ray photoelectron spectroscopy (XPS)).

3.2.1 Microscopic based characterization techniques

3.2.1.1 Scanning Electron Microscopy

Scanning electron microscopy (SEM) is a useful technique for high-resolution imaging of surfaces that is used to characterize nanomaterials. The SEM technique provides information regarding surface morphology of the materials. The SEM uses an electron rather than light for imaging surfaces, and an electron beam is directed toward the specimen at the top of the microscope by heating a metallic filament to form an image. The electron beam travels vertically via electromagnetic lenses that focus and direct the beam to the sample, as revealed in Fig 3.2.1.1. A highly concentrated electron beam is shot from an electron source and strikes the specimen surface. When the beam of electrons hits the sample, three types of

electrons (or backscattered, secondary, and Auger electrons), and X-rays are emitted. SEM uses of the backscattered and/or the secondary electrons to examine an image (i.e grain size, surface and cross-sectional morphologies) which have fairly low energy and reflected (back scattered) electrons both give information about topography of the specimen surfaces [271-273].
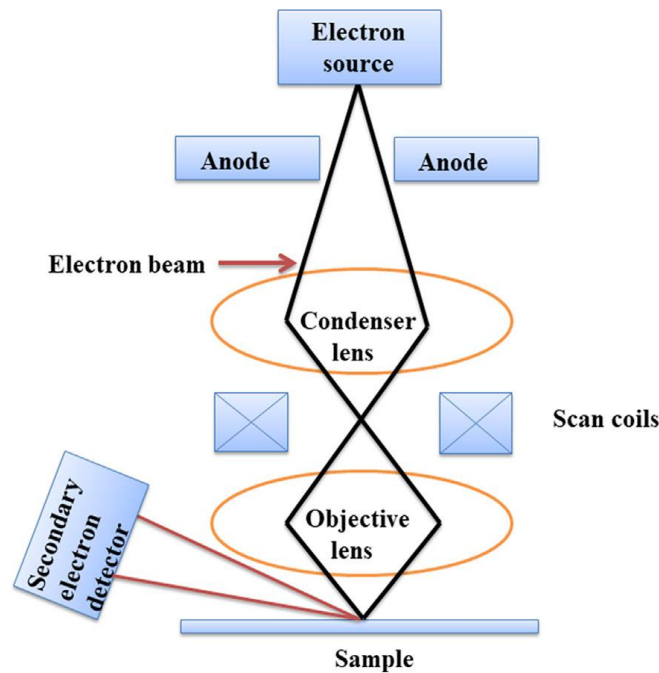
Figure 3.2.1.1: Working principle of SEM [45].

In this research work, the surface morphology of the CuO nanocoatings and Ag@CuO nanocermet coatings was acquired using scanning electron microscopy (SEM, Leo-Stero Scan 440). Using appropriate detectors, the signals from the surface of the sample was detected and then focused on a screen using cathode ray tube (CRT) to reproduce the morphology images. SEM images were taken on a higher resolution field emission with acceleration voltage ranging from 3 to 10 kV. The current probe range was 6 to 10 μm. The images were captured using SEMAfore software.

3.2.1.2 Energy Dispersive X-Ray spectroscopy

Energy dispersive X-Ray spectroscopy (EDX) is a technique for elemental analysis and their proportion present on the surfaces of the samples in conjunction with SEM of the surface morphology. EDX spectra provide elemental composition and image of materials using emitted x-rays from the material during beam bombardments. A higher energy beam of charged particles such as electrons or X-rays are focusing and moving across the material being investigated. Electrons excite from inner shells by the incident electrons and image of

the sample is obtained. The SEM microscope is integrated with Energy Dispersive X-ray Spectroscopy (EDX) and with electron backscatter diffraction pattern detection and analysis system [271-273]. The same SEM (SEM, Leo-Stero Scan 440) system was used for EDX analysis and the EDX was used to perform on randomly selected regions of samples surface with an acceleration voltage of ranged between 7-10 keV. By X-ray, it was able to obtain profiles maps of elements and perform sequence analysis of particles and regions in a sample.

3.2.1.3 Atomic Force Microscopy

Atomic force microscopy (AFM) is a non-destructive and versatile microscopic technique used to study the surface morphology at nanoscale. AFM can generate an image in three-dimensional surface images at high resolution with angstrom scale (Å), and provides various kinds of specimen surface measurements. It is essential to understand how the AFM operates, its basic components, and the interaction forces between the probe and specimen surface. The structural diagram of an AFM is displayed in Fig.3.2.1.3. The AFM measures forces between the probe and specimen surface through a sharp tip (probe) deflection system, with a laser beam incident on a flexible rod called a cantilever. The sharp tip (probe), located at the end of the cantilever with small deflection is observed in the cantilever toward the surface, and interacts with the specimen surface during the scan. Changes in specimen topography encourages movement of the cantilever, which deflects the laser beam to the photo-detector. The changes in the photo-detector output are used to adjust the movement of the piezoelectric ceramic (scanner) in the z direction, whose value is recorded as a function of the scanning [45, 271, 274].
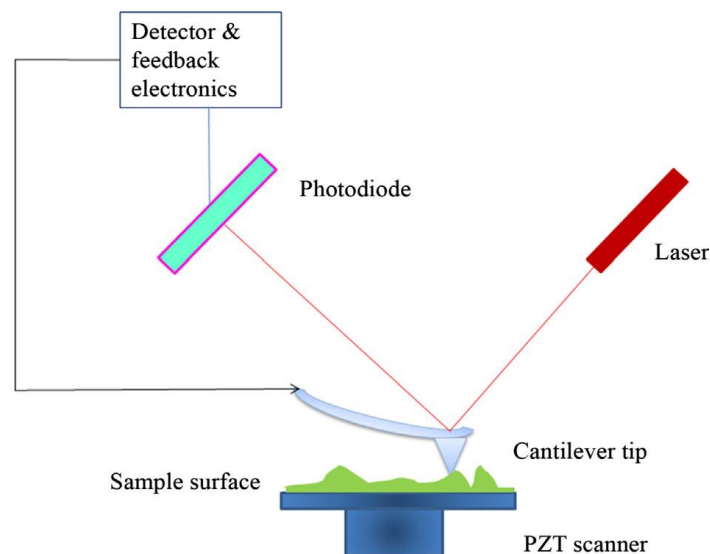
Figure 3.2.1.3: Schematic diagram of AFM principle [45].

In this research work, the topography and surface roughness of CuO nanocoatings coatings, and Ag@CuO nanocermet coatings were studied by using AFM (AFM, a Veeco® Nanoman). The system operates by scanning a tip across the sample surface while monitoring the changes in cantilever deflection with split photodiode detection. A feedback loop maintain a constant deflection between the cantilever and sample by vertically moving the scanner at each (x, y) data point to maintain a ''setup point'' deflection. The distance of the scanner moves vertically at each (x, y) data point was stored by a computer to form the topographic image of the sample surface. Digital instrument dimension 3000 AFM with a resolution of 10 pm in accompanied with nanoscope software was used for recording the surface topography and analyzing the recorded images.

3.2.2 Spectrometry-based characterization techniques

3.2.2.1 Ultraviolet-visible near infrared (UV-Vis-NIR) spectroscopy

UV-Vis-NIR spectrophotometer is a powerful characterization technique to analyse the optical property (or absorbance, reflectance, and transmittance) of nanoscale materials. It measures the interaction between absorber materials and electromagnetic radiation. The UV-Vis-NIR spectroscopy wavelength range is from the ultraviolet (200–400 nm) via the visible light region (400–800 nm) to the NIR (800–2500 nm). All non-transparent materials can absorb, reflect, and scatter specific visible wavelengths and used to analyze the optical properties of materials in terms of what they absorbed, reflected, and scattered as illustrated of in Fig.3.2.2.1. Typically, UV-Vis-NIR spectroscopic works by shining incident light at materials, and recorded the light intensity that reaches a detector, known as transmittance. Intensity loss recorded by detector, compare with the original incident light at that specific wavelengths has absorbed, reflected or scattered by the material, collectively known as extinctions [275, 276].
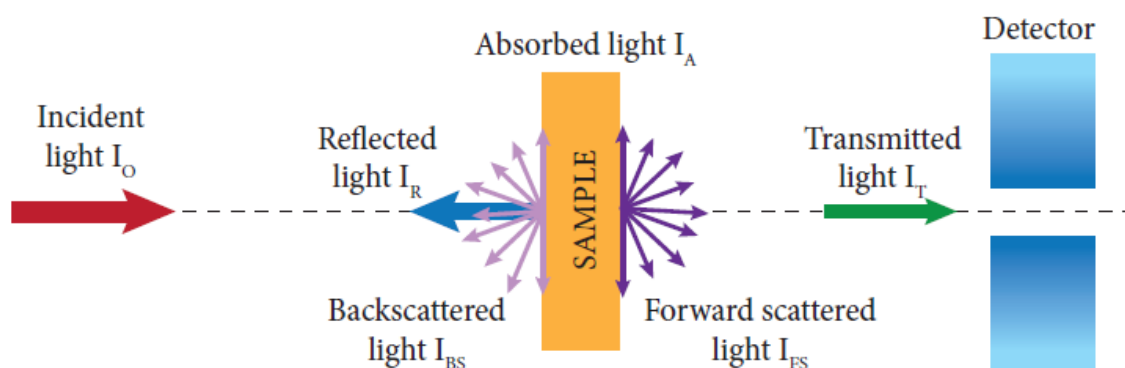
Figure 3.2.2.1: Absorption, reflection, transmission and scattering in UV-Vis-NIR spectrometer [276].

Herein, the diffuse reflectance (R) spectra of CuO nanocoatings and Ag@CuO nanocermet coatings deposited on SS substrate were measured using UV-Vis-NIR spectrometer (Varian, Inc. model Cary-2500) in the range of 0.30-2.5 μm wavelength. As a reference plate, Polytetrafluoroethylene $(C_2F_4)_n$ coated disc was used and measurements were conducted at room temperatures with 500 nm/min scanning speed. The solar absorptance(α) of all the coatings was calculated according to eq. (2.1.1.5) from the measured diffuse reflectance spectra.

3.2.2.2 Fourier-Transform Infrared Spectroscopy

The thermostatic infrared spectrophotometer is a powerful characterization technique used to measure the spectral emissivity of the absorber surface with a high spectral resolution. Thermal emission is a fundamental physical process by which all objects emit light at temperatures of above 0 K in the far IR wavelength region (>2.5 μm) or in the wavenumber range 4000-400 cm^{-1}. The spectral emissivity is an important parameter describing the thermal radiative property of absorber materials. It is well known that the emissivity (ε) value can change greatly with surface conditions of absorber surfaces and strongly depends on the surface roughness, temperature, surface oxidized film and so on. In the past decades, new developments in photonics and nanoscale fabrication have enabled research into engineered thermal emission for various applications such as passive radiative cooling, photothermal, and thermophotovoltaics [275, 277-279]. Many thermal-emission measurements are performed via reflection, and transmission measurements, and subsequent application of Kirchhoff's law, according to eq.(2.1.1.9), which relates the thermal emissivity of the absorber surface in thermal equilibrium to its absorptivity [280-282].

Herein, the thermostatic infrared spectrometer (Bruker Vertex 70) spectrometer in the infrared wavelength region (2.5–25 μm) was employed to measure was spectral reflectance in the IR region. The measurements were performed in a vacuum at room temperature and the spectra were recorded. Before the sample measurement, a background reference was performed with an Aluminium (Al) mirror placed at the same position as the sample. Finally, the thermal emissivity (ε) of CuO and Ag@CuO nanocermet coatings were calculated according to eq. (2.1.1.10).

3.2.2.3 Raman Spectroscopy

Raman spectroscopy is an important, versatile, and non-destructive technique to probe the vibrational and electronic properties of materials (solid, liquid, and gaseous). Raman spectroscopy involves measuring the inelastic scattering of monochromatic photons with different frequencies from the laser source to characterize the vibrational, rotational, and other modes of nanomaterials. Raman scattering can be divided into stokes scattering (if the emitted radiation or vibrational state has a lower frequency than the scattered photons), Antistokes scattering (if the emitted radiation has higher frequency than the scattered photons), and/or Rayleigh scattering (if the emitted radiation has same frequency with the scattered photons) (see Fig 3.4.2.3). The interaction between the scattered photons and incident light results in a shift in energy, the energy difference between the incident and scattered photon is usually known as the Raman shift (cm^{-1}); this shift provides information about the modes of phonons in the material [271, 272, 283, 284].
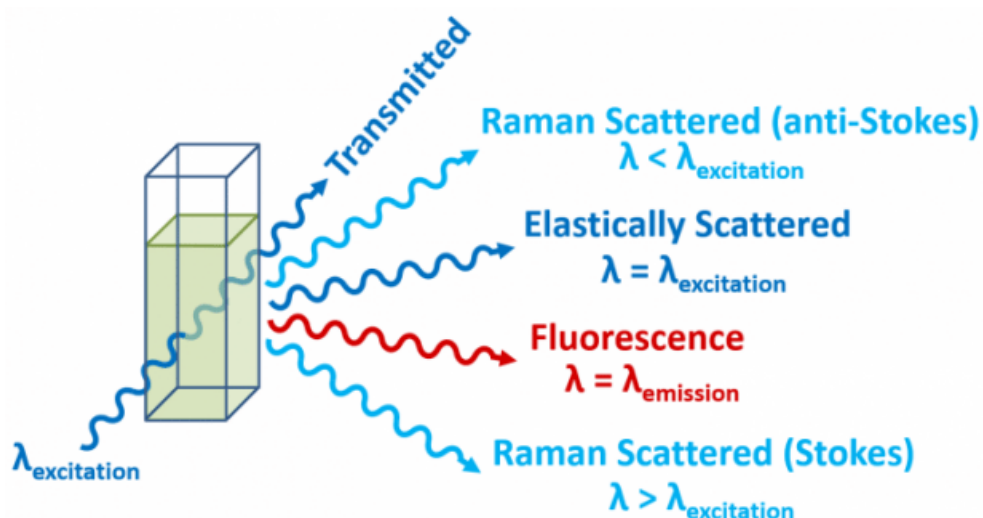
Figure 3.4.2.3 Raman spectroscopy interaction of photon with samples

In this research work, Raman spectroscopy (Jobin-Yvon T64000 Raman spectrometer) was recorded over 100–800 cm^{-1} at room temperature using 532 nm radiations for laser excitation to identify the existing phases and lattice vibrational properties of the samples. The system was operated with an output laser power of 2.5 mW and the laser beam was focused on the sample and the spectra were collected with a 600 groove/mm grating.

3.2.2.4 Rutherford Backscattering Spectroscopy

Rutherford backscattering spectroscopy (RBS) is an ion scattering technique that used nuclear technique in the ion beam analysis (IBA) fields. RBS is a useful, and precise

quantitative technique for stoichiometry, thickness, and compositional of thin film analysis without need for standards. Identification, depth, and concentration of an element is achieved by detecting the energy of beam particles by Rutherford scattering after scattered. The elastic scattering provide information on the mass involved scattering partner and also depth profile of the samples when the beam particles lose energies while crossing the sample before, and after the point of scattered. During the RBS analysis, high-energy helium ions (He^{++}) are passed into the samples, and the backscattered yield is measured at a given angle. RBS provide lower accuracies for lower elements in a periodic table [272, 285-288].
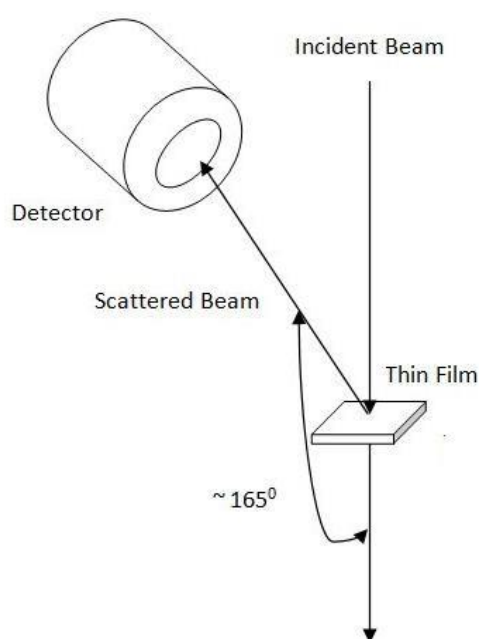
Figure 3.2.2.4: Schematic representation RBS set up at scattering angle of 165°.

Herein, the elemental composition, thicknesses, and depth profile of CuO and Ag@CuO nanocermet coatings were determined using Tandetron accelerator RBS (NEC MeV ion beam accelerator systems, RBS, USA) at iThemba labs, NRF-South Africa. The samples were individually mounted on a ladder before being loaded into a sample chamber with a vacuum pressure greater than 10^{-6} mbar. The channel energy of backscattered energy of particles was achieved using silver copper oxide nanocomposite on silicon substrate calibration sample. The scattered ion energy spectra were recorded using a Si surface detector positioned at a scattering angle of 165° with a 2MeV ^{4}He^{++} beam. The RBS spectra were simulated using SIMNRA 7.02 software to determine elemental compositions, thickness, and depth profile of the obtained coatings.

3.2.3 X-ray based Characterization Techniques

3.2.3.1 X-Ray Diffraction

X-ray diffraction (XRD) is the most widely used characterization technique and provides information related to the nature of the phase, crystalline structure, crystalline size, and lattice parameters. During the measurement, the interaction of the monochromatic X-rays beam with the atomic planes results in refracted, absorbed, scattered, and diffracted by the angle (θ) (see Fig 3.2.3.1). Scattering occurs only when the X-ray impinges the crystal lattices. Maximum scattering is eliminated as it interferes with itself, which is known as destructive interference. When the scattering comes in phase with another plane, diffraction occurs, and the diffracted beams from the sample interfere constructively for certain angles and appears as peak intensity. The diffraction of the beam is directly related to the atomic crystal arrangements, which is described by Bragg's law, and occurs only when Bragg's Law is fulfilled for constructive interferences from planes with spacing "d" [271, 272, 275, 289] and is given by eq.(3.2.3.1).

$$n\lambda = 2d \sin \theta \qquad\qquad (3.2.3.1)$$

where d is planes space planes, θ is Bragg angle, n is order of reflections, and λ *is* beam wavelengths (Fig. 3.2.3.1).
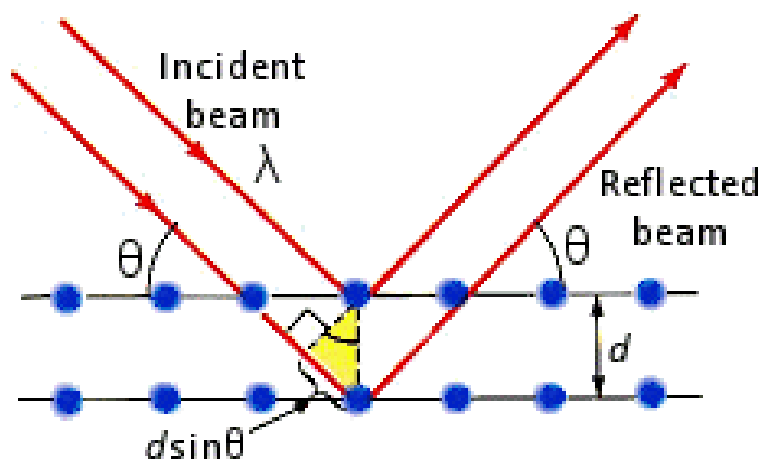
Figure 3.2.3.1: X-ray diffraction

In this research work, CuO nanocoatings and Ag@CuO nanocermet coatings were studied by using X-ray diffraction (XRD, D-800, Bruker AXS). D-800, Bruker AXS X-ray diffractometer was employed to analyze the phase and crystal size of the absorber samples. The samples were characterized by rotating the sources and detector at a constant angular

speed for 2θ between 0 and 100°. The samples were analysed at normal angles of incidence with an incident beam angle of 45°. The diffractometer uses a monochromatic Cu X-ray source with a major component CuKα-1 radiation of wavelength 01.5406 Å, a voltage of 40 kV and current of 40 mA.

3.2.3.2 X-Ray Photoelectron Spectroscopy

X-Ray Photoelectron Spectroscopy (XPS) is commonly used to analyze the near-surface composition of materials for oxidation states, and elemental composition within a material. In XPS analysis, the material irradiated with monochromatic X-rays in an ultra-high vacuum environment leads simultaneously measured both the kinetic energy and number of electron excited from core orbitals of the elements at the surface. The kinetic energies and number of electron that emitted from the material surfaces provide characteristics of the surface composition of the samples. X-ray excitation causes the emission of photoelectrons and are measured by analysing the binding energy present on the surface of the substance. The intensities of the peaks reflects the type of each element, and the position of peaks confirms the chemical states for each element within a material [272, 275, 285, 287].
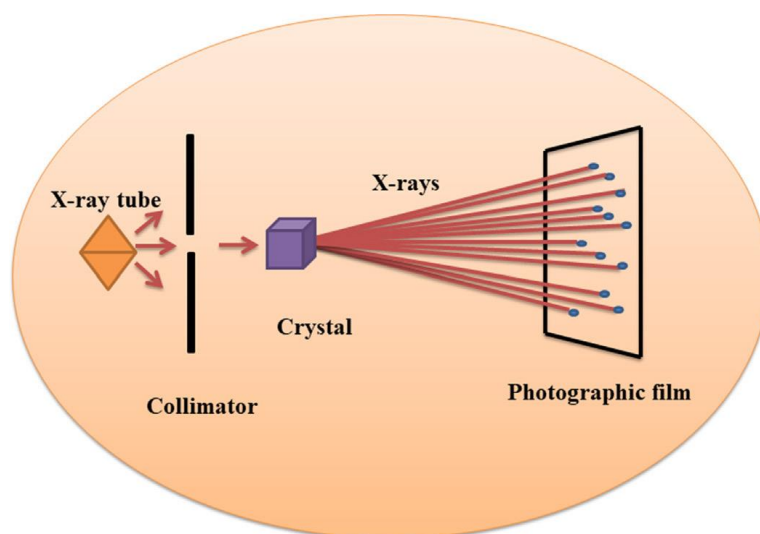
Figure 3.2.3.2 Principle of X-ray photoelectron spectroscopy

In this research work, the chemical state of CuO and Ag@CuO nanocermet coatings were analysed using X-ray photoelectron spectroscopy (XPS, a thermo K-alpha spectrophotometer). X-ray photoelectron spectroscopy (XPS) was performed using a thermo scientific K-alpha photoelectron spectrometer using monochromatic Alkα radiation. During the measurement, the sample was irradiated with X-rays and a detector measured the kinetic energies of those ejected electrons coming from the surface (from the top 1-10 nm) of the

sample. Higher resolution scans were recorded for the principal peaks at a pass energy of 50 eV. The peaks were modelled using CasaXPS software with binding energies adjusted to adventitious carbon (284.5 eV) for charge correction.

CHAPTER FOUR

RESULT AND DISCUSSION

4.1. Single layered biosynthesised copper oxide(CuO) nanocoatings as solar selective absorber

4.1.1 Possible reaction mechanism of green synthesised CuO nanoparticles

The phytochemicals present in plant materials are rich in secondary metabolites with different functional groups such as -C-O-H, –C–O–, -C-N-C-, –C=C-, –C=O– etc., which have a significant role in the formation, nucleation, accumulation, and stabilizing of the nanomaterials. Different plant parts, such as roots, stems, leaves, seeds, fruits, peel, or flowers, can be used in biosynthesis of nanoparticles. The cactus pear, commonly known as Prickly Pear belongs to Angiosperm Cactaceae family. The cactus pear (Opuntia ficus indica) is the source of several phytochemicals like flavonoids, saponins, phenylpropanoids, alkaloids, polyphenols, essential oils, and steroids. In biosynthesis, the plant extracts are mixed with a metal precursor salts at ordinary temperature, which is easy, environmentally friendly, cost-effective, and non-toxic [43, 45, 46, 290].

In this reaction mechanism, we hypothesised the organic molecules present in a plant extracts with a poly hydroxyl functional group as a phytochemical agent for CuO NPs formation as displayed in Fig.4.1.1. In the biosynthesis of CuO nanoparticles, the phytochemicals in the cactus extracts activate the copper (Cu) metal in the copper nitrate-trihydrate $(Cu(NO_3)_2.3H_2O)$ into Cu^{2+} ion in a mixture solution, leads to the formation of complex structure with phytochemicals of the extract or $[Phyto-Cu-Phyto]^{2+}$ complex structure. The formed complex structure is converted into $Cu(OH)_2$ and byproduct, and then to CuO after dried in a vacuum oven at temperature of 100 ^{o}C. Finally, the obtained amorphous CuO stabilized and capped into CuO nano-powders by annealed at 420 ^{o}C [43, 46, 291].
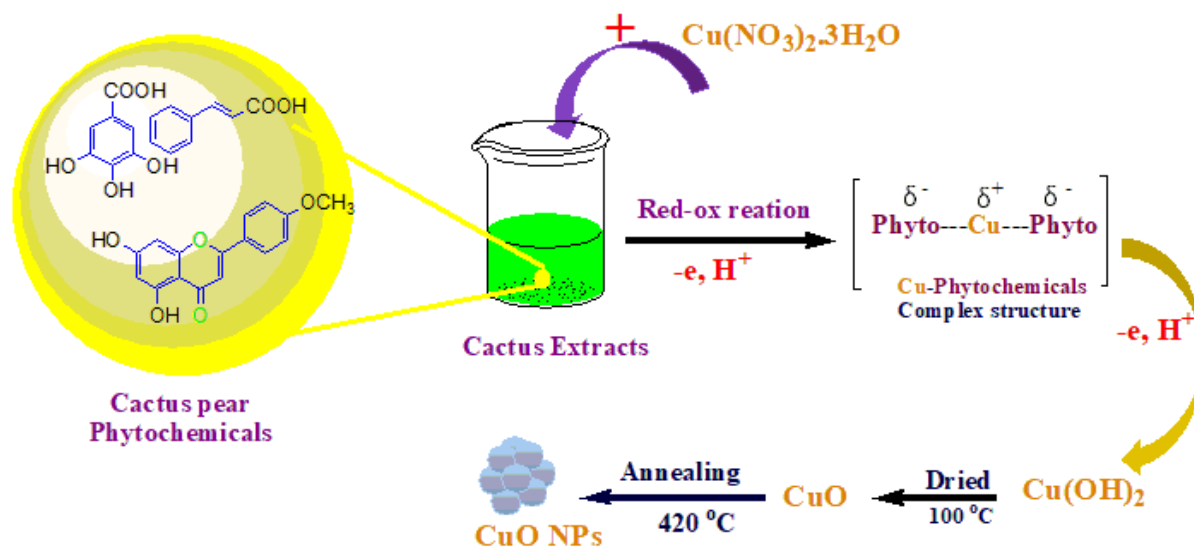
Figure 4.1.1: Proposed reaction mechanism of CuO NPs via Cactus extracts

4.1.2 Surface morphology of CuO nanocoatings

4.1.2.1 Scanning electronic microscopy

The morphological surface is one of the most important factor that influences the performance of spectrally selective absorber (SSA) coatings [292]. The surface morphology of single-layered CuO nanocoatings via green synthesis was characterized using scanning electronic microscopy (SEM). Fig.4.1.2.1(a-d) shows SEM images of CuO nanocoating on stainless steel (SS) substrate deposited using spin-coating at 700, 800, 900, and 1000 rpm, respectively. From the SEM images, nanorod likes-structures are observed, and the surface structures are densely covered and compacted at lower RS of 700, and 800 rpm as shown in Fig. 4.1.2.1(a, b). When the RS increases to 900 and 1000 rpm a nanorod-like surface with lower density is observed, as shown in Fig. 4.1.2.1(c, d). The particle size of CuO nanocoatings are found to be 57.6, 51.2, 43.1, and 36.7 nm at 700, 800 ,900, and 1000 rpm, respectively; these results confirm that thickness of coatings decrease with increase of RS of the spin coating [75, 293].
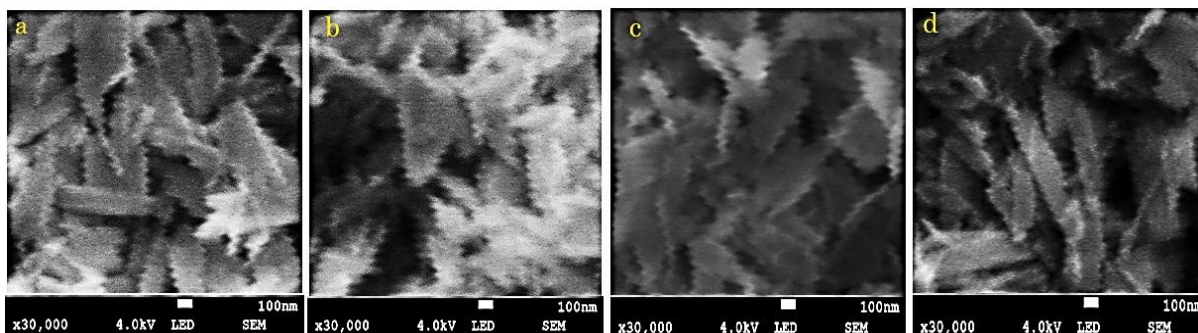
Figure 4.1.2.1: SEM image of CuO nanocoatings spin coated at RS of a) 700 b) 800 c) 900 d) 1000 rpm

4.1.2.2 Atomic force microscopy

Fig.4.1.2.2 (a-d) depicts the 3D AFM image of green synthesized CuO nanocoatings deposited by spin-coating on SS substrate at RS of 700, 800, 900, and 1000 rpm. The AFM images confirm the presence of nanorod-like structures on the CuO nanocoating surfaces. From Fig.3 (a, b) at RS of 700, and 800 rpm growth of vertically aligned nanorod-like structures with relatively uniform distribution and better coverage of nanorod surfaces are observed, and these are characterized by higher surface roughness of 28.3, and 24.5 nm, respectively. From Fig.4.1.2.2 (c, d), further, increase in the RS to 900, and 1000 rpm, complicated the uniform distribution of the particles, and the vertically aligned nanorod-like structures are reduced as well as appeared smooth with a surface roughness of 21.2, and 17.6 nm, respectively. As the RS increase the surface homogeneity of nanorod-like surfaces, and grain size are reduced, indicating that the crystallization quality and thickness of the nanocoatings are decreased. The average surface roughness of CuO coatings is slowly decreased with increasing in RS due to lowering of the coating thickness and surface uniformity of the coatings [294-296] as shown in Fig. 4.1.2.2 (a-d). It should be noted that the surface roughness is an important factor in an absorber surface, as the incident light interacts directly with it. When the incident light encounters the absorber surface of the coatings, some of them are absorbed and some reflected. The suitable surface roughness creates optical traps between nanosized particles, which can increase the scattering of short wavelengths and reflection of long wavelengths [295, 297]. Moreover, the distribution of peaks in the surface structure traps more-light in the inner structure of the coatings by multireflection, consequently, the intrinsic absorption of CuO nanocoatings can be enhanced which contribute to better solar absorption properties [41, 298].

70
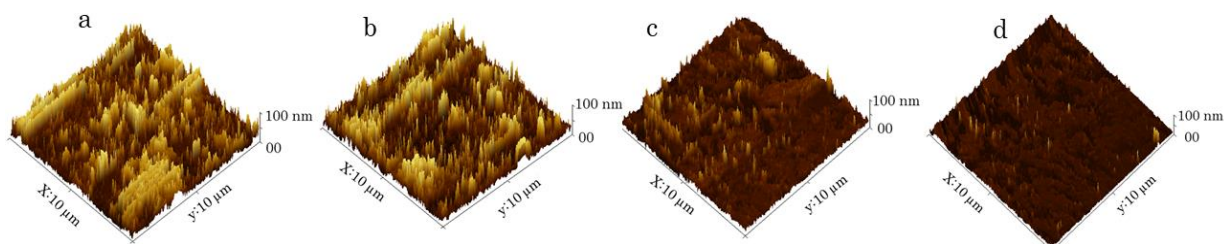
Figure 4.1.2.2: AFM of CuO nanocoatings spin coated at RS of (a) 700, (b) 800, (c) 900, and (d) 1000 rpm

4.1.3 Structural and compositional analysis of CuO nanocoatings

4.1.3.1 X-ray diffraction

The structural analysis of CuO nanocoatings were analysed from x-ray diffraction (XRD) spectra. Fig. 4.1.3.1(a-d) shows the XRD patterns of CuO nanocoatings spin-coated on SS substrates at RS of 700, 800, 900, and 1000 rpm. The crystallographic orientations originated at 2θ values of 32.6°, 35.5°, 38.6°, 48.8°, 53.5°, and 58.2° associated to (110), (11$\bar{1}$), (111), (20$\bar{2}$), (020), and (202) crystal planes of the monoclinic phase structure of CuO, respectively, and it is well-matched with the previous literature (according to the JCPDS card No. 80-1917) [40, 299, 300]. For all the obtained nanocoatings, characteristic diffraction patterns at 2θ values of 43.58°, and 50.72° attributed to (111), and (200) planes of the face-centered cubic (fcc) of Chromium Iron Nickel (Cr0.19 Fe0.7 Ni0.11) SS substrate are observed, respectively (according to the JCPDS card No. 033-0397). The average crystalline size (D) of the nanocoatings were calculated from Scherrer's formula, $D = 0.9\ \lambda/\beta\cos\theta$ where λ is wavelength, β is the full width at half maximum (FWHM) at the diffracting angle θ, by determining the width of (111) Bragg reflection [301, 302], and found to be 76, 57, 44, and 36 at RS of 700, 800, 900, and 1000 rpm, respectively. The results in agreement with the trend observed by SEM. As shown in Fig 4.1.3.1 (a-d), increasing RS results decrease in the intensity of the coatings, which confirms that the thickness, grain size, and crystallite of the deposited nanocoatings are decreased [294, 303].
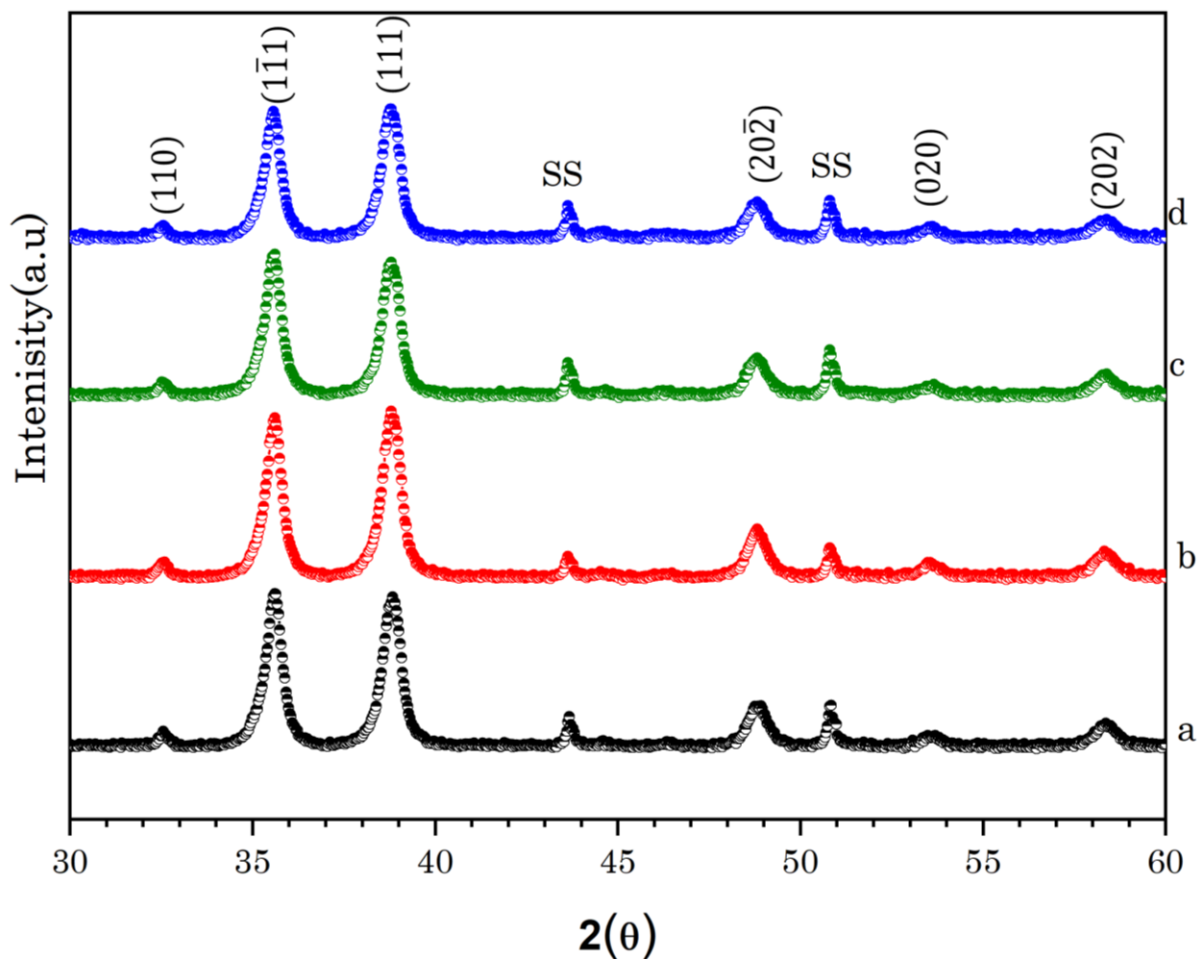
Figure 4.1.3.1: XRD of CuO nanocoatings spin coated at RS of a) 700, b)800 c) 900 d) 1000 rpm

4.1.3.2 Energy dispersive spectroscopy

The elemental compositions of green synthesised CuO nanocoatings deposited on SS substrate at different RS were determined using the EDS technique. EDS of CuO nanocoatings with nanorod-like structure (as observed in SEM) are shown in Fig.5 (a-d). The EDS spectra reveal strong peaks associated to Cu and O, confirming the purity of CuO nanocoatings. The EDS spectra also show weak peaks of Fe and Cr which originated from SS substrate. EDS result also suggests that the atomic percentage of Cu, and O are decreased with increase of RS of the coating which compliments with the XRD results.
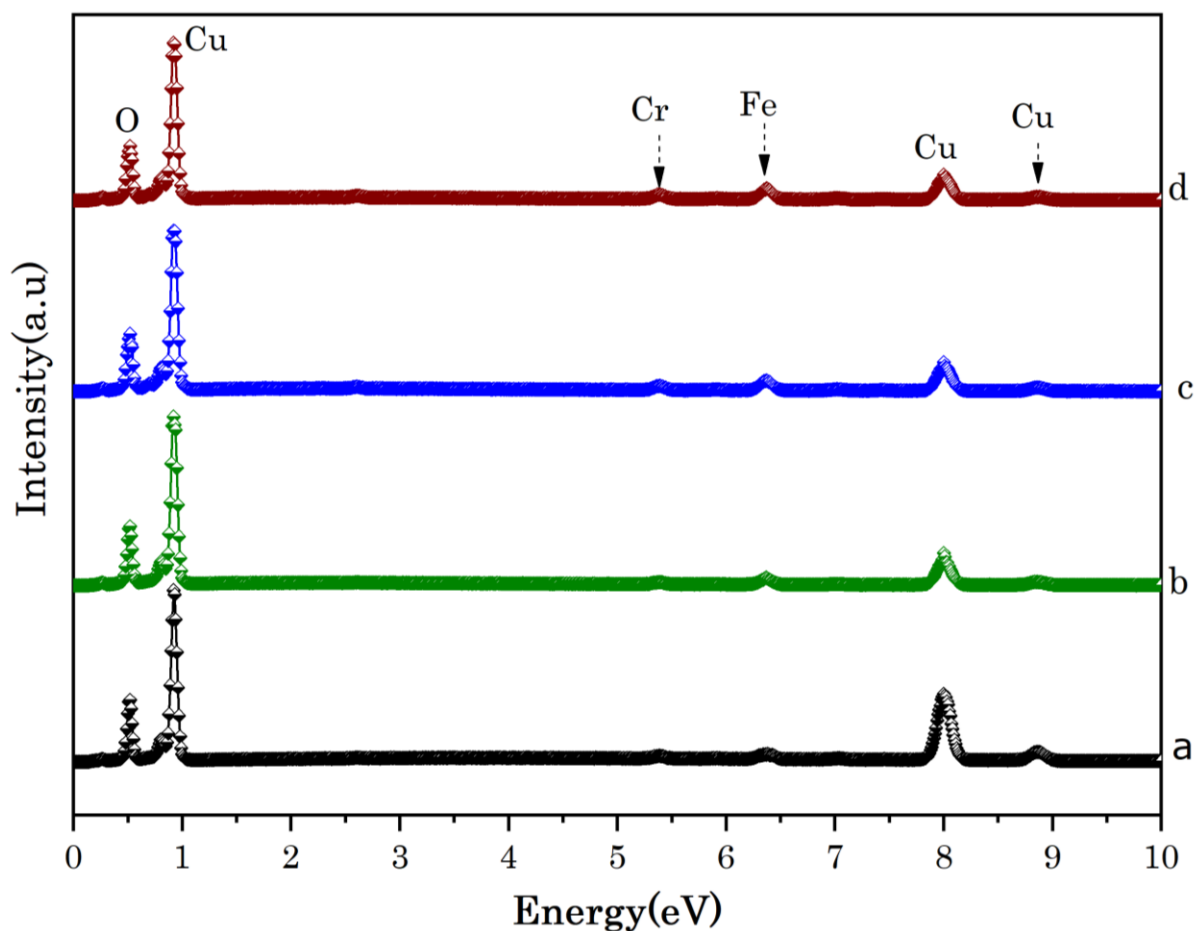
Figure 4.1.3.2: EDX spectra of CuO nanocoatings spin coated at RS of a) 700, b)800 c) 900 d) 1000 rpm

4.1.3.4 Raman spectroscopy

Raman spectroscopy is a versatile and non-destructive technique used to probe the phase and vibrational properties of materials [42]. CuO belongs to C^6_{2h} symmetry with two molecules per primitive cell, and has twelve (12) phonon modes (i.e 4Au + 5Bu +Ag + 2Bg) in Raman spectrum; of these only three (Ag + 2Bg) modes are Raman active [17, 43, 44]. Fig.4.1.3.4 (a-d) reveals the Raman spectra of biosynthesized CuO coatings recorded over 200–700 cm^{-1} at room temperature using 532 nm radiation. The Raman spectrum exhibits the characteristic peaks of CuO at 305.5, 344.3, and 642.7 cm^{-1}. The first peak at 305.5 cm^{-1} is assigned to Ag mode and the two peaks at 344.3 and 642.7 cm^{-1} are attributed to the Bg mode [43, 45]. As shown from Fig.4.1.3.4 (a-d) at lower RS of the spin coating, the Raman peak intensity is more intense, and sharper, confirming that the thickness, particle sizes, and crystallinity are improved [52], which is good complement with the obtained XRD results. Xu *et.al* [52], reported that the Raman spectra peaks become stronger as well as sharper and shift to higher wave numbers as grain size increases. Moreover, the Raman spectrum shows a weak peak at

73

596.5 cm^{-1} which clearly indicates the presence of Cu$_2$O phase [43]. From the Raman analysis both CuO and Cu$_2$O phases coexisted in the coatings. However, the XRD spectra does not reveal the presence of Cu$_2$O phase, and this confirms that Raman spectroscopy is more surface sensitive than XRD and provides more surface information [43].
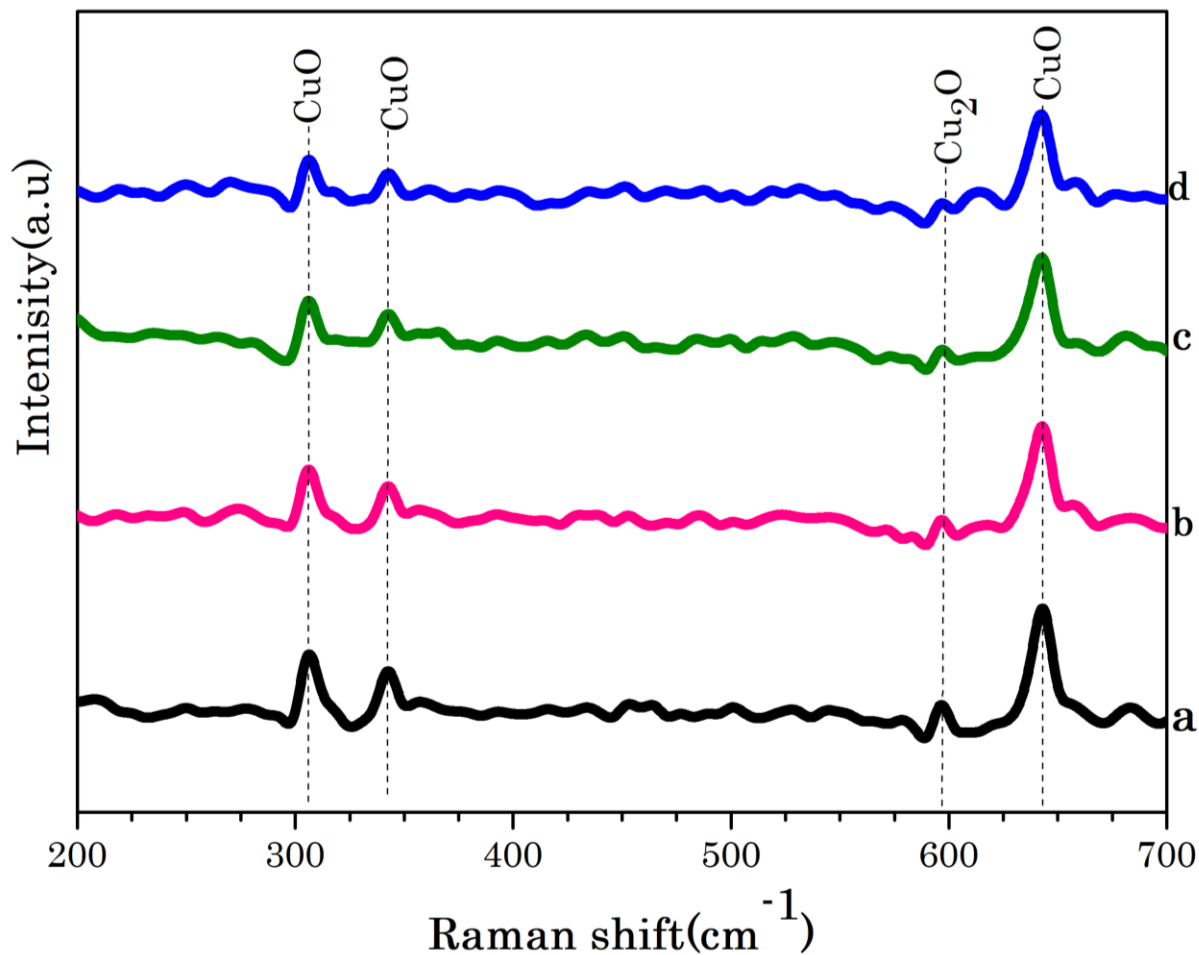
Figure 4.1.3.4 Raman spectra of CuO nanocoatings spin-coated at a) 700 b) 800 c) 900 d) 1000 rpm

4.1.4 Optical properties CuO nanocoatings

The optical properties of green synthesized CuO nanocoatings were analyzed using UV–Vis–NIR (300–2500 nm), and IR (2500–20000 nm) spectrometers. The absorptance and emissivity (α, ε) of the coatings were deduced from their corresponding diffuse reflectance spectra using eqs.(2.1.1.5) and (2.1.1.10), respectively. Fig.4.1.4 (a-b) reveals the spectral reflectance spectra of CuO nanocoating absorbers in the solar and IR region, respectively as a function of spin coating rotational speed (RS). The spectra reflectivity of CuO nanocoatings in the UV-Visible region (300–800 nm) is below 2% while above the visible (or from 800-2500 nm) a gradual transition from low to high reflectance is observed. In the IR region ($\lambda \geq$ 2500 nm), the reflectivity spectra of the coatings is above 40%, and increase with increasing RS of the spin coating, as revealed in Fig.4.1.4 (a, b) and indicates that good characteristic spectrally selective coatings were obtained [283]. At 700 rpm, the lower reflectance spectra is observed both in solar and IR spectrum and reveal the broader absorption or highest solar absorptance (α) of 0.90, and emissivity (ε) of 0.31 as shown in Fig.4.1.4 (a, b). When the RS increased to 800 and 900 rpm, the reflectivity spectra of the coatings raised, the solar absorptance (α) value is slightly decreased to 0.88 and 0.86, simultanously, the emissivity is decreased to 0.28 and 0.23, respectively. Further increasing in RS to 1000 rpm, a higher reflectance spectrum is observed; thus both (α, ε) are smoothly decreased, respectively to 0.85 and 0.19 as shown in Fig.4.1.4 (a, b).

It is well known that at lower RS of the spin coating, the coatings tended to be slightly thicker with rough surface [296] (also observed from AFM). This increases the solar absorption by lowering the surface reflection of the coatings in the solar spectrum region and also causes to have high infrared absorption as well as higher attenuation of light in the IR region. Consequently, the reflectance spectra of the coatings is lowered which is attributed to rise the of emissivity (ε) of the coatings [67, 303, 304]. Moreover, the appropriate surface roughness can determine the optical properties of absorber surfaces. When the dimension of surface roughness is longer than the wavelength (λ) of incident light, the electromagnetic wave (EW) get more trapped energy which contributes to better solar absorptivity in the solar spectrum region. On the contrary, when the wavelength (λ) of the sunlight is longer than surface roughness, the coating surface exhibits mirror-like properties and most of infrared (IR) light would be reflected in the IR region, so a lower emissivity (ε) could be achieved [41, 292, 305].
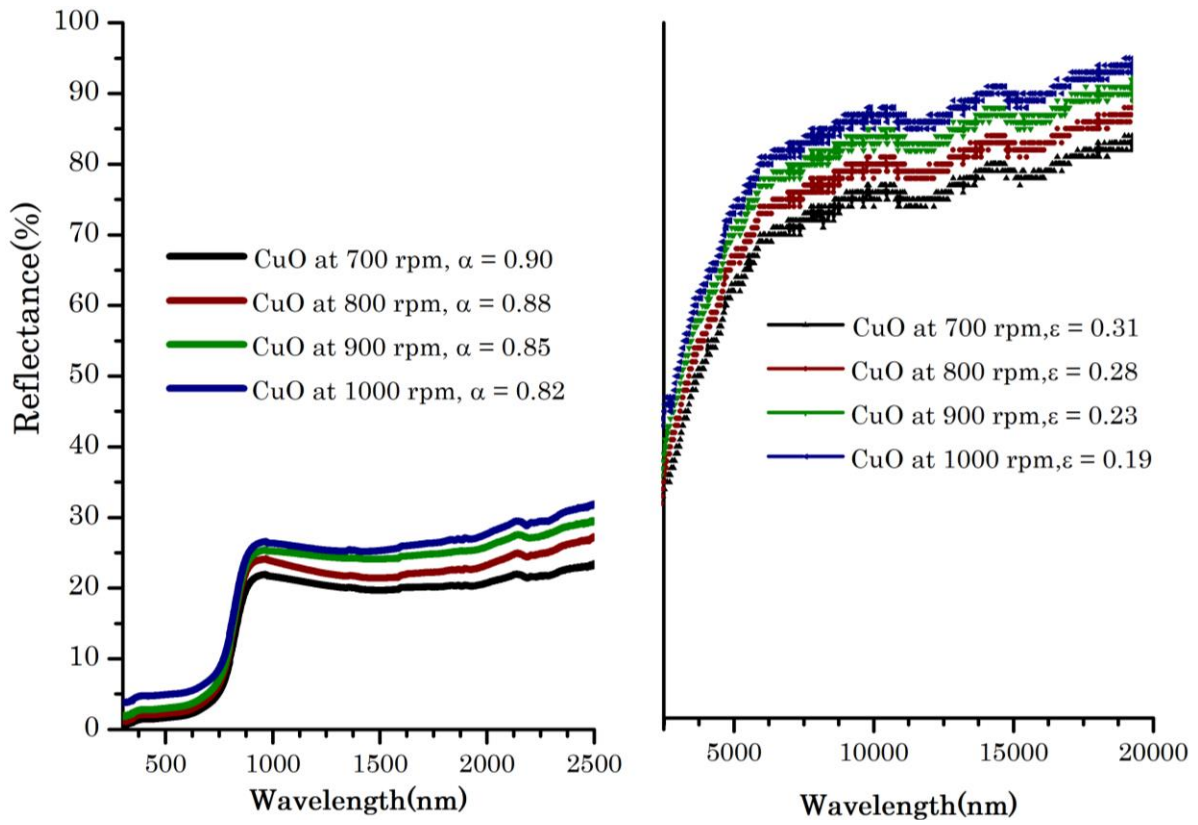
Figure 4.1.4: Diffuse reflectance of CuO nanocoatings a) solar region b) IR region

4.2 Spectrally selective single layered Ag@CuO nanocermet coatings; Surface morphology, structural, and optical properties

4.2.1 Surface morphology of Ag@CuO nanocermet coatings

4.2.1.1 Scanning electronic microscopy

The surface morphology of green synthesized single-layered Ag@CuO nanocermet coatings was characterized using Scanning electronic microscopy SEM). Fig.4.2.1.1(a-e) shows the SEM images of CuO coating and Ag@CuO nanocermet coatings spin-coated on SS substrates at 700, 800, 900 and 1000 rpm. Fig.4.2.1.1 (a) exhibits a surface image of CuO nanocoating spin-coated at 700 rpm, and a nanorod-like structures with uniform particle distribution are observed with a grain size value of 57.6 nm. Fig.4.2.1.1 (b-e) reveals Ag@CuO nanocermet coatings spin-coated at RS of 700, 800, 900, and 1000 rpm. The surface morphology confirms that bright white Ag nanoparticles clusters on CuO surface are observed, and the existence of these Ag NPs has obviously changed the boundary grains of CuO, and thus non-uniform, as well as irregular nanorod-like structures are observed, as shown in Fig.4.2.1.1 (b-e) compare to CuO coating in Fig. 4.2.1.1 (a), this may be assigned to high agglomeration came from lack crystallinity of Ag@CuO nanocermet coatings [41, 294]. When the spin coating RS increases from 700 to 1000 rpm, uniformly dispersed of Ag NPs on CuO surface are decreased, as shown in Fig.4.2.1.1(b-e). The grain size of Ag@CuO nanocermet coatings are 68.3, 56.1, 48.7, and 42.4 nm at 700, 800, 9000, and 1000 rpm, respectively; these results confirm that the coating thickness is decreased with RS of the spin coating increased [293].
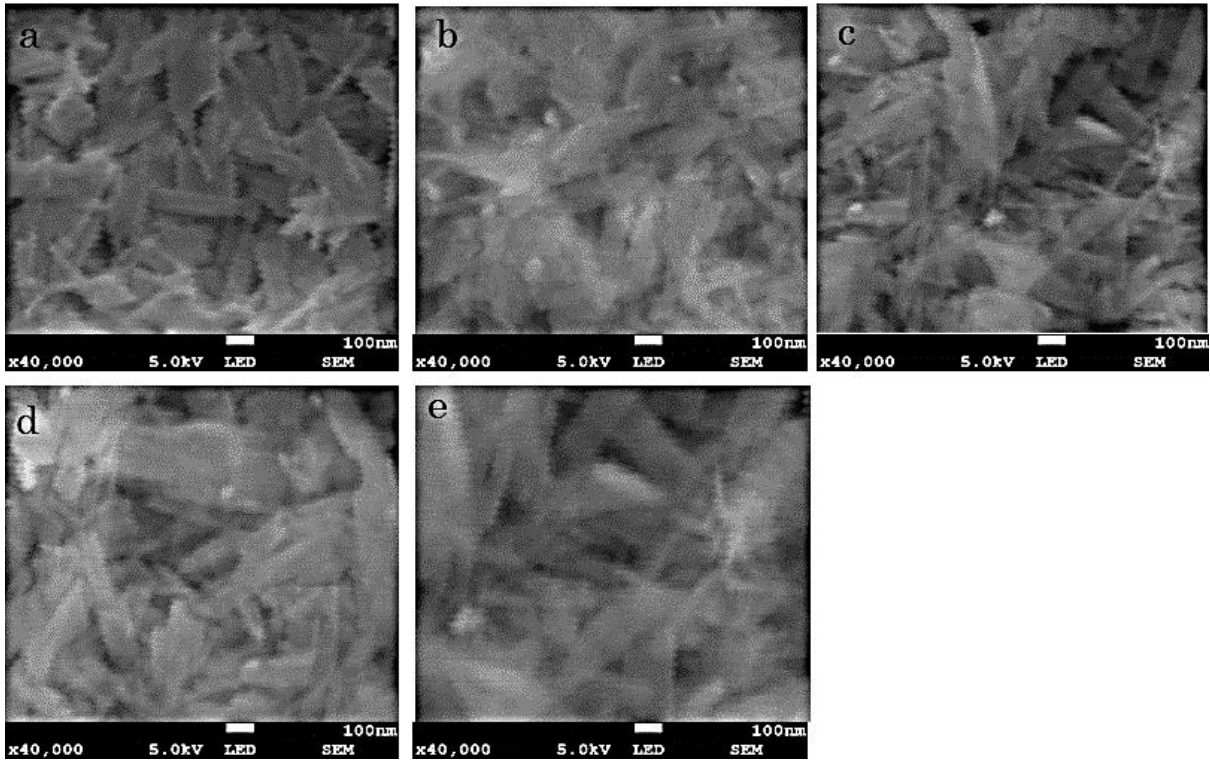
Figure 4.2.1.1: SEM images of CuO coating (a) at 700 rpm, and Ag@CuO nanocermet coatings b) 700, c) 800, d) 900, and e) 1000 rpm

4.2.1.2 Atomic force microscopy

The 3D AFM images of green synthesis CuO and Ag@CuO nanocermet coatings spin-coated at different RS are shown in Fig.4.2.1.2 (a-e). The CuO coating surface deposited at RS of 700 rpm has a relatively smooth and homogeneous surface with an average surface roughness of 34.1 nm as shown in Fig.4.2.1.2 (a). Fig.4.2.1.2 (b-e) reveals AFM images of Ag@CuO nanocermet coatings at RS of 700, 800, 900, and 1000 rpm, respectively. The embedded Ag NPs in the matrix of CuO surface presents the feature of a peak and valley structure and grain growth, as shown in Fig.4.2.1.2 (b-e). The embedded Ag NPs increase the average surface roughness of Ag@CuO nanocermet coatings compared to CuO coating due to the accumulation of plasmonic Ag NPs in the CuO matrix which leads the coatings to absorb more light (including infrared band) [292, 306]. The average surface roughness of Ag@CuO nanocermet coatings is decreased in the range of 45-23 nm as RS increased from 700 to 1000 rpm, possibly a result of lowering the thickness as well as surface uniformly of the coatings as shown in Fig.4.2.1.2(b-e). The surface roughness is a key factor to increase the surface solar absorption by decreasing the surface reflection might be with the increasing roughness in the solar spectrum region. When the incident light encounters the coating absorber surface, more light is absorbed (including infrared band), and some are reflected. Moreover, the peaks

78

and valley structures of the coatings can trap more light effectively in the inner structure of the coatings by multireflection on the surface of individual peaks [41, 292].

Figure 4.2.1.2: 3D AFM image of CuO coating (a) at 700 rpm, and Ag@CuO nanocermet coatings b) 700, c) 800, d) 900, and e) 1000 rpm

4.2.2 Structural, and compositional analysis of Ag@CuO nanocermet coatings

4.2.2.1 X-ray diffraction

The crystallinity and phase purity of Ag@CuO nanocermet coatings were evaluated from X-ray diffraction (XRD) spectra. Fig.4.2.2.1 shows the XRD patterns of green synthesized (a) CuO coating at RS of 700 rpm, and (b-e) Ag@CuO nanocermet coatings spin-coated on SS substrates at RS of 700, 800, 900, and 1000 rpm, respectively. The crystallographic orientations originated at a diffraction angle of 32.45º, 35.5º, 38.6º, 48.7º, 53.4º and 58.3º corresponding to the (110), (11$\bar{1}$), (111), (20$\bar{2}$), (020), and (202) crystal planes, respectively, as revealed in Fig.4.2.2.1 (a). These results confirm the formation of a monoclinic phase of CuO crystals, and it is well-matched with the previous literature (according to the JCPDS card No. 80-1917) [40, 299, 300]. Moreover, from Fig.4.2.2.1 (b-e), the XRD patterns at 2θ values of 38.14º and 44.27º corresponding to (111), and (200) crystal planes are assigned to face-centered cubic (fcc) phase of Ag metal (according to JCPDS file no. 35–0801) [270, 307], these confirm the successful embedment of Ag NPs into CuO to form Ag@CuO nanocermet coatings. For all coatings, the diffraction patterns originated at 2θ values of 43.58° and 50.72° associated to (111) and (200) planes of the fcc of Chromium Iron Nickel

(Cr0.19 Fe0.7Ni0.11) SS substrate, respectively (according to the JCPDS card No. 033-0397). As shown in Fig.4.2.2.1 (b-e), as the RS spin coating of Ag@CuO nanocermet coatings increased, the peaks intensity is slightly decreased, which confirms that thickness of the deposited coatings is decreased [303]. Moreover, when the Ag NPs are incorporated into CuO, the peak intensity of CuO coatings is decreased, this may be due to the lack of crystallinity of the obtained Ag@CuO nanocermet coatings as well as the scattering factors difference of Ag, and Cu atoms. However, there are no changes in the position of peaks, and thus the incorporated Ag NPs do not affect the monoclinic phase structure of CuO [298, 307].
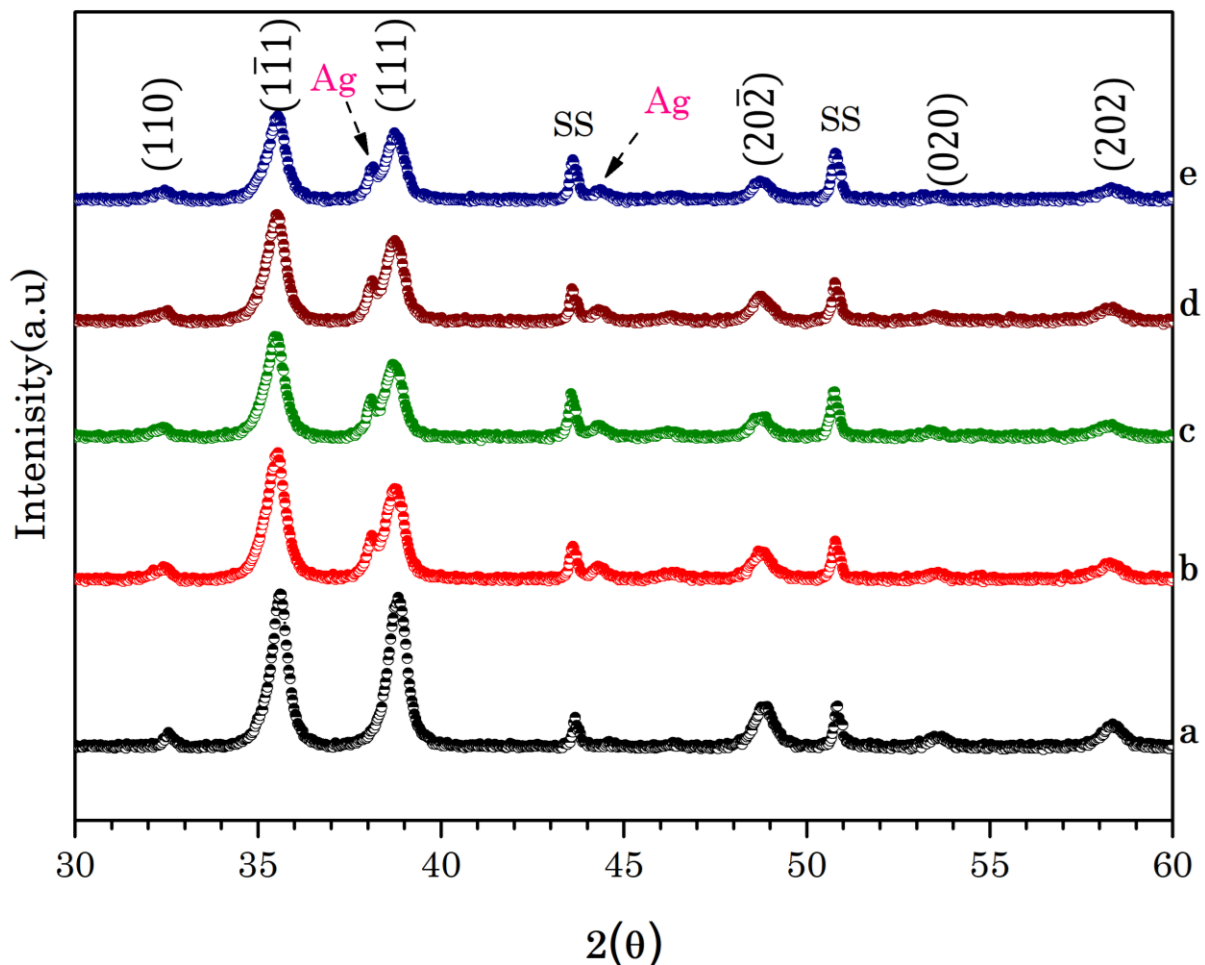
Figure 4.2.2.1: XRD pattern of CuO coating (a) at 700 rpm, and Ag@CuO nanocermet coatings b) 700, c) 800, d) 900 and e) 1000 rpm

4.2.2.2 Energy dispersive spectroscopy

The elemental composition of Ag@CuO nanocermet coatings was analyzed using Energy dispersive spectroscopy (EDS). Strong peaks attributed to O and Cu are detected which confirms the purity of coatings as shown in Fig.4.2.2.2 (a). Fig.4.2.2.2 (b-e) represents the EDS of Ag@CuO nanocermet coatings spin-coated at 700, 800, 900 and 1000 rpm. In

addition to Cu, and O, weak peaks from Ag metal are observed, as revealed in Fig.4.2.2.2 (b-e) which confirms that the Ag metal is well embedded into CuO for the formation of Ag@CuO nanocermet coatings. A weak peak of iron (Fe) from SS substrate is also observed.
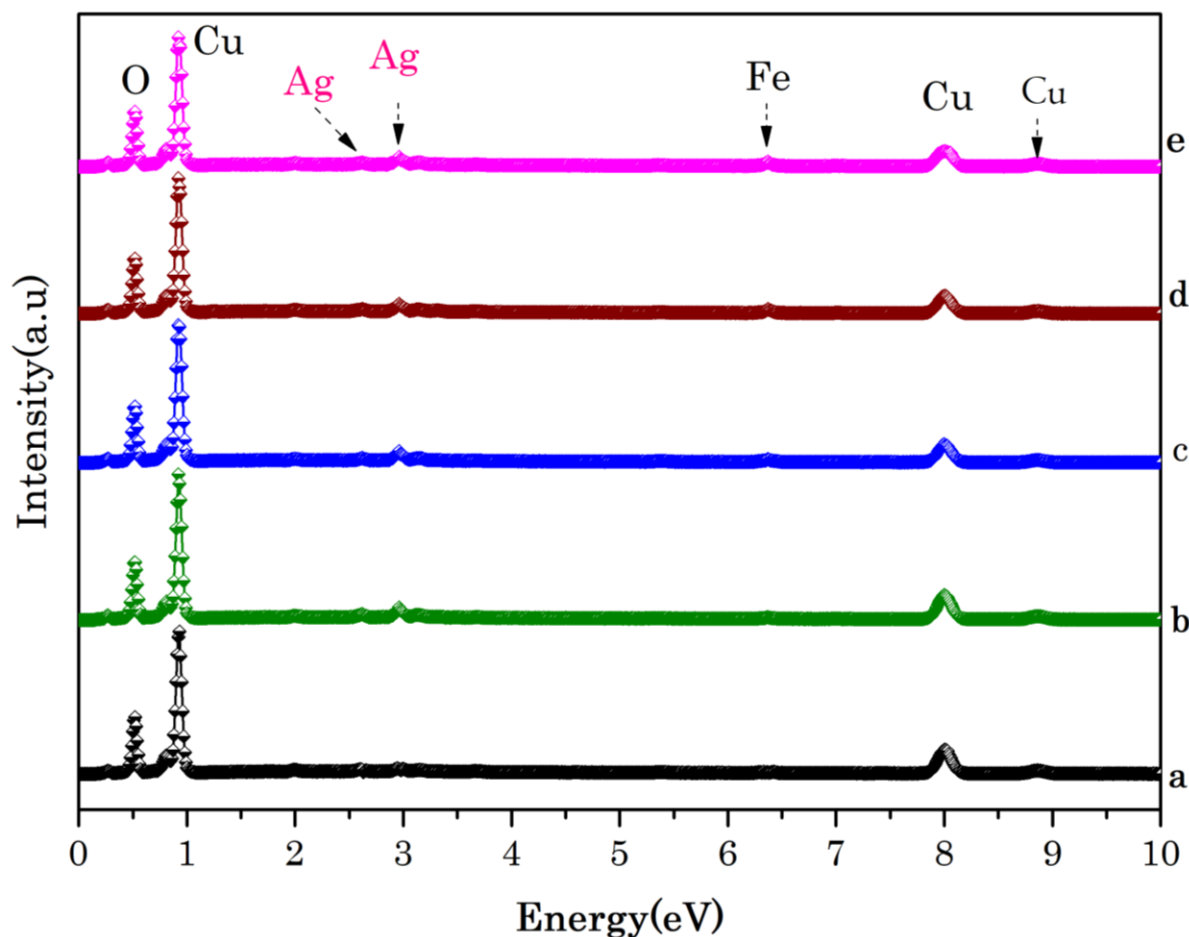
Figure 4.2.2.2: EDX spectra of CuO coating (a) at 700 rpm, and Ag@CuO nanocermet coatings b) 700, c) 800, d) 900, and e) 1000 rpm

4.2.2.3 X-ray photometry spectroscopy

The surface electronic states and elemental composition Ag@CuO nanocermet coatings on SS substrate was analyzed via X-ray photometry spectroscopy (XPS), and the results displayed in Fig.4.2.2.3 associated to 700 rpm. The Wider scan spectra of CuO nanocoating confirms the presence of Cu, O, Ag, C, and N elements as shown in Fig.4.2.2.3 (a). The high resolution of XPS spectra of Cu2p shows that two peaks of Cu $2p_{1/2}$ and Cu $2p_{3/2}$ at 953.15 eV, 933.72 eV binding energy, respectively, as shown in Fig.4.2.2.3 (b), which are typical characteristics peaks of Cu (II) for CuO. The binding energy of Cu2p$_{1/2}$ and Cu2p$_{3/2}$ are separated by 20 eV are essentially identical binding energies of Cu2p of Cu(II). The satellite peak at 944.13 eV confirms the presence of paramagnetic chemical states of Cu^{2+}. From XPS

spectra a peak with low intensity centered at 932.62 eV binding energy is associated to Cu^{1+}. As demonstrated in Fig.4.2.2.3 (b), the corresponding XPS spectra O in Ag@CuO reveals two-peaks, which indicates that there are two-oxygen states, and the peak at 529.30 eV binding energy corresponding to metal-oxygen (M-O) lattice which confirms the formation of CuO [231, 308]. In the XPS spectrum of Ag3d (Fig.4.2.2.3 (c)), two peaks of Ag $3d_{3/2}$ (375.75 eV) and Ag$3d_{5/2}$ (369.20 eV) are attributed to metallic Ag^+ and Ag^o, respectively which well-agrees with the previous reports [231, 308]. Among them, the C element might derive from impurities on the surface of the samples.
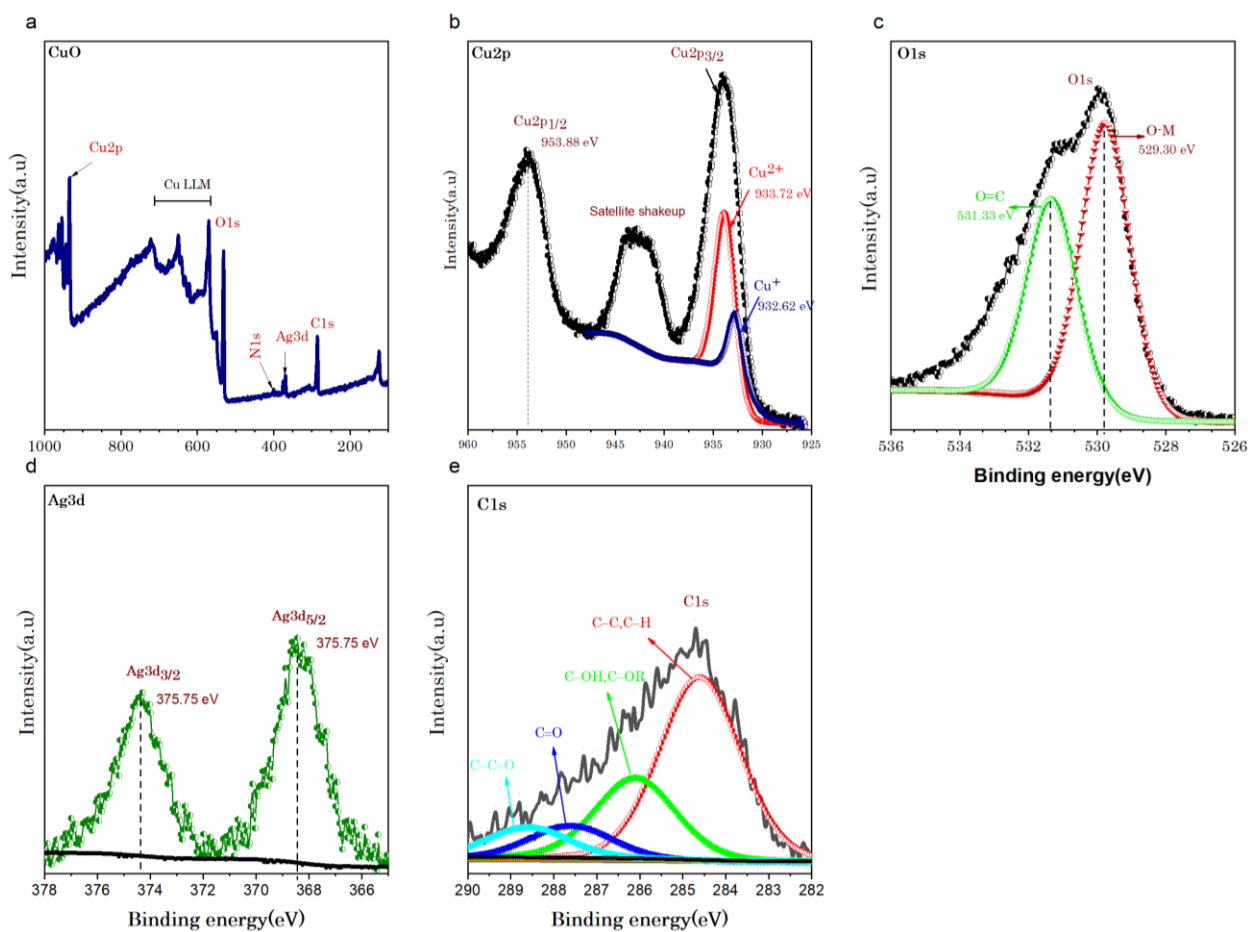
Figure 4.2.2.3: XPS spectra of a) Ag@CuO, b) Cu2p, c) O1s, d) Ag3d, and e) C1s associated to 700 rpm

82

4.2.2.4 Rutherford backscattering spectrometry

The elemental composition and thickness of green synthesized Ag@CuO nanocermet coatings were determined using Rutherford backscattering spectrometry (RBS). RBS is the most precise quantitative, and versatile technique of ion beam analysis for elemental surface analysis, and depth profiling of thin films, as gives information on the thickness, content, and depth of thin films and absolute concentration of elements in the thin film without the need for standards [286, 288, 309]. Fig.4.2.2.4 (a-e) shows the RBS spectra of CuO (a), and Ag@CuO (b-e) nanocermet coatings at RS 700, 800, 900, and 1000 rpm. The fitting of RBS spectra was simulated using SIMNRA 7.03 software to determine elemental composition and thickness of the coatings. In Fig.4.2.2.4 (a) two peaks of alpha particles backscattered from Cu and O atoms at channels of 2424, and 1112, respectively are observed. The contents of elements of Cu, and O is 54, and 46 at %, respectively, and the thickness of CuO coating is calculated to be 1406×10^{15} atoms/cm^2 (296.3 nm) at 700 rpm. Fig.4.2.2.4 (b-e) shows RBS results of Ag@CuO nanocermet coatings, the plasmonic Ag atom appeared at channel of 2605, in addition to peaks of Cu, and O atoms. The concentration of Ag, Cu, and O contents in Ag@CuO nanocermet is 5, 51, and 44 at percentage (%), respectively, and the result does not show remarkable change, as the RS is increased from 700 to 1000 rpm. Thickness of Ag@CuO nanocermet coatings are found to be 1416×10^{15} atoms/cm^2 (298.2 nm), 1296×10^{15} atoms/cm^2 (272.8 nm), 1153×10^{15} atoms/cm^2 (242.7 nm), and 998×10^{15} atoms/cm^2 (210.2 nm) at 700, 800, 900, and 1000 rpm, respectively, at 700, 800, 900 and 1000 rpm, respectively.
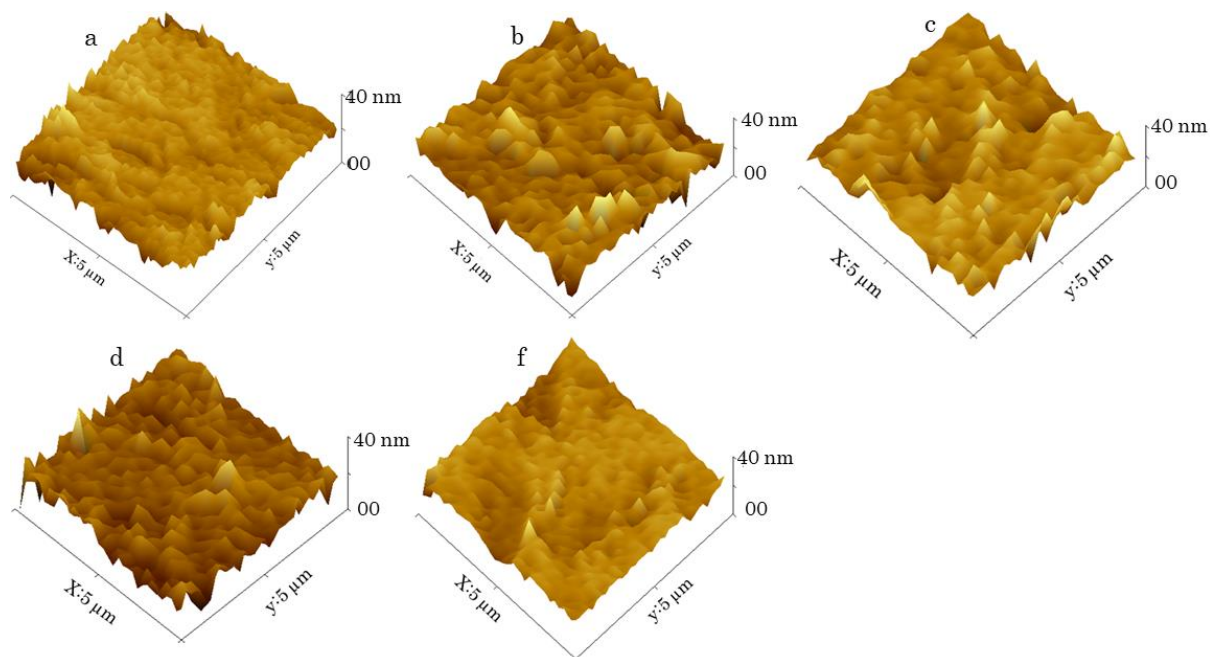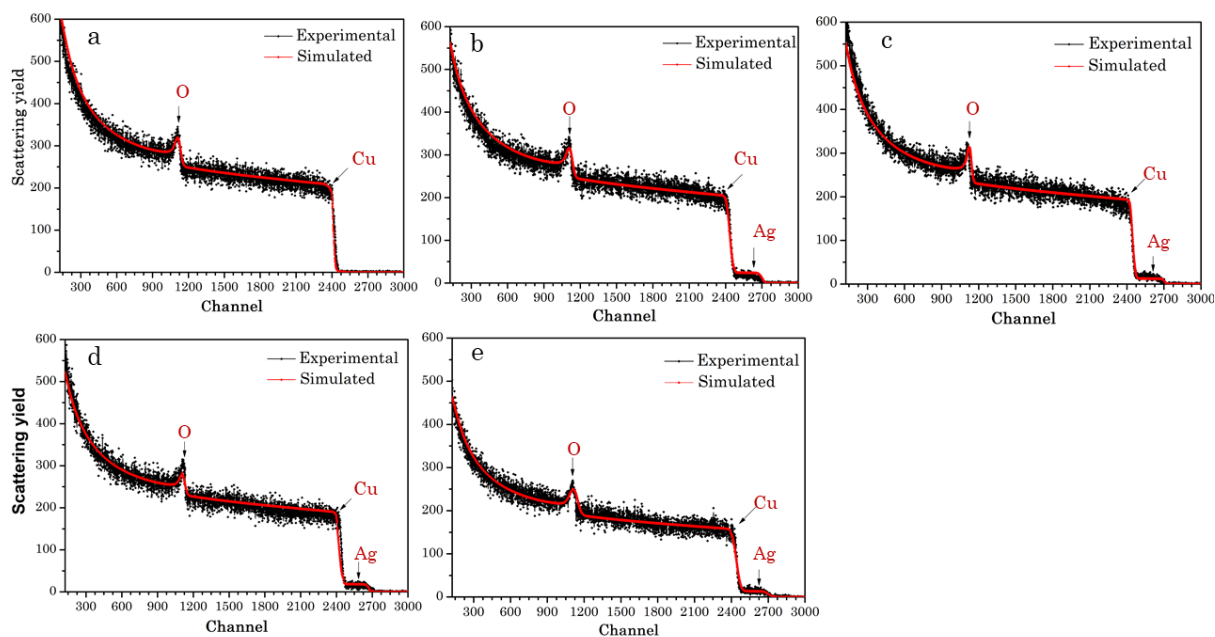
Figure 4.2.2.4: RBS spectra of CuO coating (a) at 700 rpm, and Ag@CuO nanocermet coatings b) 700, c) 800, d) 900 and e) 1000 rpm

4.2.3 Optical properties Ag@CuO nanocermet coatings

The optical property of Ag@CuO nanocermet coatings deposited on SS substrates via spin coating were characterized using UV–Vis–NIR (300–2500 nm), and IR (2500–20000 nm) spectrophotometry. The optical parameters of solar absorptance (α), and emissivity (ε) of the nanocermet coatings were calculated from their diffuse reflectance data's using eqs. (2.1.1.5), and (2.1.1.10), respectively. Fig.4.2.3 (a, b), shows the optical characteristics of both CuO, and Ag@CuO nanocermet coating absorbers in solar spectrum region (300–2500 nm), and in the mid-infrared spectrum region (2500–20000 nm), respectively as a function of spin coating rotational speed (RS). The CuO coating exhibits relatively higher reflectance spectra in solar region with a absorptance(α) value of 0.90, while in the IR region displays lower reflectance with higher emissivity (ε) value of 0.31 as shown in Fig.4.2.3 (a, b). The optimized Ag@CuO nanocermet coatings have broader absorptions in a solar spectrum compared to CuO coatings. In the UV-visible spectrum (300–800 nm) the diffuse reflectance of nanocermet coatings is lower than 3%, while above the visible (or from 800-2500 nm) a gradual transition from low to high reflectance is observed as revealed in Fig.4.2.3 (a), Simultaneously in the IR ($\lambda \geq$ 2500 nm) region, the reflectance spectra increases sharply from 27% to a value higher than 94% as shown in Fig.4.2.3 (b), indicates that good characteristics of spectrally solar selective coatings [283]. With the Ag@CuO nanocermet coating deposited at 700 rpm, a lowest reflectance spectrum is observed both in the solar and IR region; conversely, it achieves

respectively the highest solar absorptance (α) value of 0.93, and emissivity (ε) of 0.23 as shown in Fig.4.2.3 (a, b). The embedded AgNPs in the CuO surfaces enhanced the intrinsic absorption properties of Ag@CuO nanocermet coatings due to the concentrated free electrons which contribute to trapping of more incident light caused by inter-band transitions and surface plasmon resonance in the solar spectrum while being transparent to the longer wavelength of IR radiation [59, 311-313]. When the spin coating RS increases to 800 and 900 rpm, the spectral reflectance slightly increases, leading the solar absorptance(α) value to decrease to 0.91, and 0.88, together the emissivity (ε) is decreased to 0.18 and 0.14 respectively. Further increasing the RS to 1000 rpm both the absorptance (α), and emissivity(ε) values are smoothly decreased to 0.86, and 0.11, respectively. Table 4.2.3 summarise both (α, ε) values of CuO and Ag@CuO nanocermet coatings as a function of the RS of spin-coater.

Table 4.2.3: Summarise the RBS thickness, solar absorptance (α), and emissivity (ε) of CuO and Ag@CuO nanocermet as a function of RS of the spin coater.

RS of Spin-coater	CuO nanocoatings			Ag@CuO Nanocermet coatings		
	RBS thickness	Absorptance (α)	Emissivity (ε)	RBS thickness	Absorptance (α)	Emittance (ε)
700 rpm	296.3 nm	0.90	0.31	298.2 nm	0.93	0.23
800 rpm	271.0 nm	0.88	0.28	272.8 nm	0.91	0.18
900 rpm	239.8 nm	0.85	0.23	242.2 nm	0.88	0.14
1000 rpm	207.5 nm	0.82	0.19	210.2 nm	0.86	0.11

The results confirm both the solar absorptance (α), and thermal emissivity (ε) are gradually decreasing with increasing the RS due to decrease in thickness (as confirmed from RBS) and effect of surface morphology of nanorod-like surfaces of the coatings. Firstly, as the film thickness decreases, the volume of light-matter interaction and light scattering within the coatings decreases, resulting in lower light absorption and higher reflectance of the coatings, which leads to a decrease in absorptance (α) in the solar spectrum. Furthermore, based on surface morphology, the particle size of the coatings is found to decrease as RS increases, which may reduce efficient capturing of incident light in the solar spectrum [67, 292, 303, 310].

The surface roughness, and thickness of the nanocermet coatings, on the other hand can greatly influence the thermal emissivity (ε). The surface roughness is a key factor that creates more optical traps between nanoparticles, which can increase the scattering of short waves,

and the reflection of long waves [297, 314, 315]. Moreover, when the dimension of surface roughness is longer than wavelength of the incident light, the electromagnetic wave (EWs) is getting more trapped by multiple reflections, resulting in improved solar absorption in the solar spectrum region. On the contrary, when the light wavelength is longer than surface roughness, the coating surface exhibits mirror-like properties, and most of the infrared (IR) light would be reflected in the IR region, allowing for lower emissivity (ε) could be achieved. The intrinsic reflectance properties of the coatings are much higher in the IR region than in the visible spectrum [41, 292, 305].
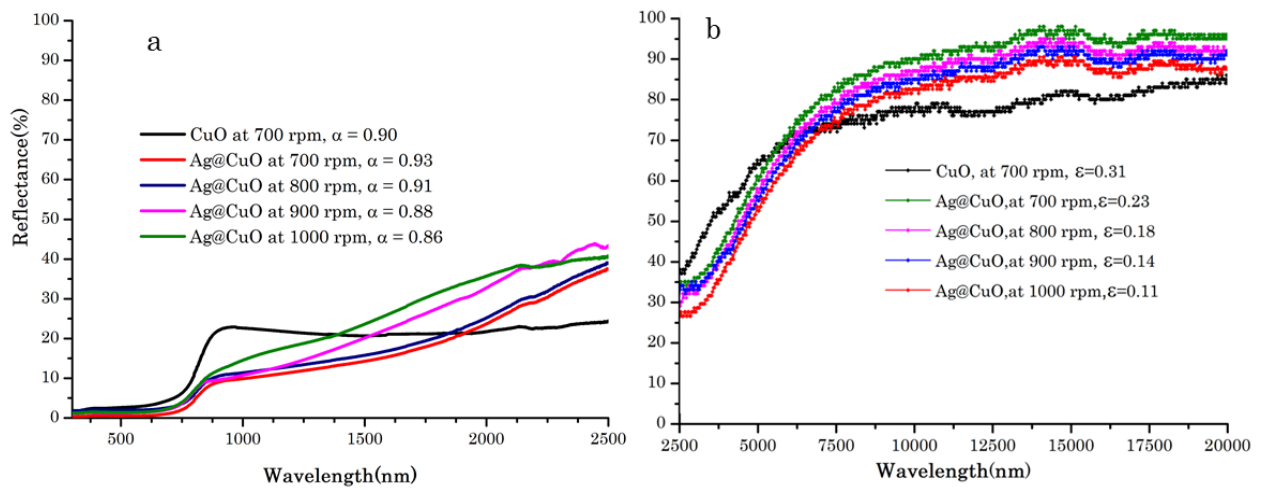
Figure 4.2.3: Reflectance spectra of CuO, and Ag@CuO nanocermet coatings: a) solar spectrum b) IR spectrum

4.3 Electrodeposition of nanostructured copper oxide (CuO) coatings as solar selective absorber

4.3.1 Electrodeposition mechanism of Cu metal

The field electrochemistry deals with electrochemical processes and involves electrodeposition or electroplating, electrophoresis, and displacement deposition for fabrication, characterization, and functionalization of materials on the electrode surface. The principle electrodeposition mechanism is the movement of positive (+ve) or negative (-ve) ions under the influence of an applied potential between electrodes in an electrolyte solution. The electrodeposition of a metal layer is achieved by the presence of a negative charge or cathodic potential on the electrode, which is immersed into ionic conductor solution or electrolyte that contains a salt precursor of the reduced metal. The metallic ions of the salt with +ve charge are attracted to the electrode surface, which provides electrons(e^-) to reduce the metal ions on the electrode or substrate surface. The interface between the electrolyte solution and electrodes is the heart of electrochemistry. It is an area where charged particles or ions are transferred. Moreover, the mechanism of depositions, nucleation, and growth processes as well as structures and properties of the deposits, are the key components in electrodeposition of materials. Generally, the electrochemical depositions of metals involve the reduction of metal ions (M^{z+}) from an electrolysis solution as follows [138, 316, 317].

$$M^{z+}_{Solution} + ze^- \longrightarrow M_{Lattice} \tag{4.3.1a}$$
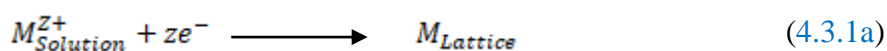
According to this equation, Z electrons(e^-) are supplied by a direct external current (DC), and then a metal ion (M^{z+}) is transferred from the electrolyte into the ionic metal lattice ($M_{Lattice}$). Herein, the electrochemical deposition of Cu metal on stainless steel (SS) substrates were carried out using three-electrode configuration equipped with a saturated calomel electrode (SCE, Ag/AgCl) as reference electrode (RE), Platinum (Pt) plate as a counter electrode (CE), and SS substrates as working electrode (WE). Fig. 4.3.1 (a, b) illustrates the electrodeposition process of Cu metal on WE or SS surface and formation of CuO, respectively.
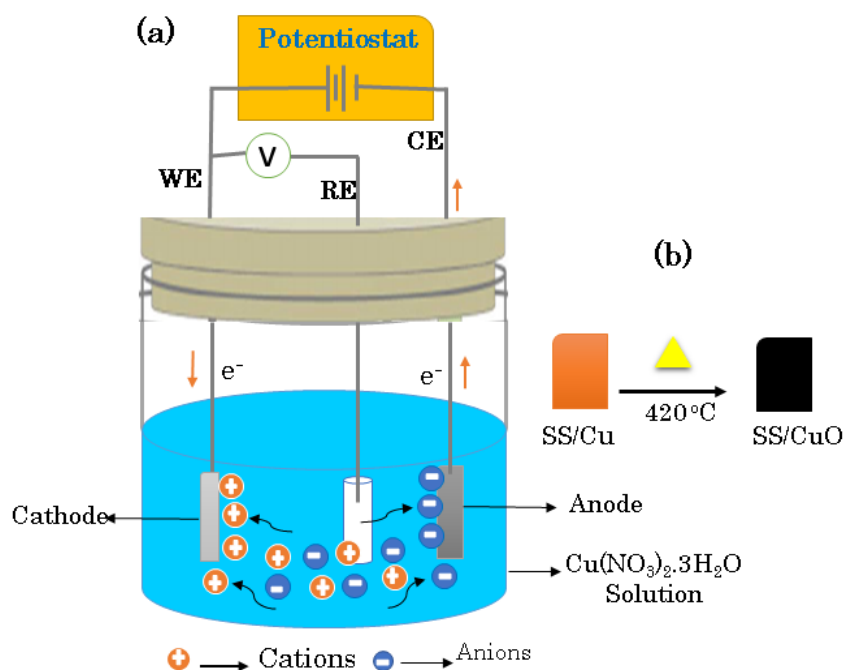
Figure 4.3.1: Schematic diagram of (a) electrodeposition process of Cu metal, and (b) thermal oxidation of Cu thin film

The electro-reduction process or reduction of copper ions(Cu^{2+}) from $Cu(NO_3)_2$ electrolyte begins as soon as a DC or cathodic potential is applied across the WE, and occurs according to the following two-stage electrochemical reactions ((Cu^{2+}/Cu^{+}, and Cu^{+}/Cu)), the 1st one being the rate-determining step, and the 2nd step is the reduction of Cu ions to Cu metal [318-321].

$$Cu^{2+} + e \longrightarrow Cu^{+}, \quad E^0 = -0.087 \quad vs \; SCE \quad Slow \qquad (4.3.1b)$$
$$Cu^{+} + e \longrightarrow Cu, \quad E^0 = -0.281 \quad vs \; SCE \quad Fast \qquad (4.3.1c)$$
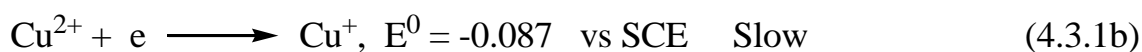
After successful electrodeposition, we observed that a red Cu thin film appeared at the surface of the SS substrates, and then the electrodeposited Cu thin films were thermally oxidized at 420 ℃, and results in the growth of nanostructured CuO coating. A nano profilometer (Nanomap, Bruker) was used to measure the coating thickness and found to be 42, 60 and 74 nm at 15, 20, and 25 min of deposition time, respectively.

4.3.2 Surface morphology of nanostructure CuO coatings

4.3.2.1 Scanning electronic microscopy

The surface morphology is one of the key factor in spectrally selective absorbers, and the absorber surfaces are strongly depends on the surface morphologies the coatings [292]. The surface morphology of electro-deposited CuO coatings were analyzed using SEM and AFM.

Fig.4.3.2.1 (a-c) exhibits the SEM images of nanostructured CuO coatings on stainless (SS) substrate at 15, 20, and 25 min deposition time. It clearly shows that uniformly distributed and well-covered nanowall-like structures of CuO coatings are observed at 15 min deposition time as revealed in Fig.4.3.2.1 (a). With increase in the deposition time to 20 min, the nanowall-like surfaces become denser and more faceted as shown in Fig.4.3.2.1 (b). Further increase in the deposition time to 25 min, resulted in the nanowall-like structures are well arranged, compacted, and more homogeneous, as revealed in Fig. 4.3.2.1 (c). The particle size of the coatings is found to be 26, 37, and 44 nm at 15, 20 and 25 min of electrodeposition, respectively. The increment in grain size confirms that the thickness and crystallization quality of the coatings are improved with deposition time, and this is attributed to increase in surface energy of the coating which is useful for selective absorber surfaces in photothermal devices [75, 294, 322].
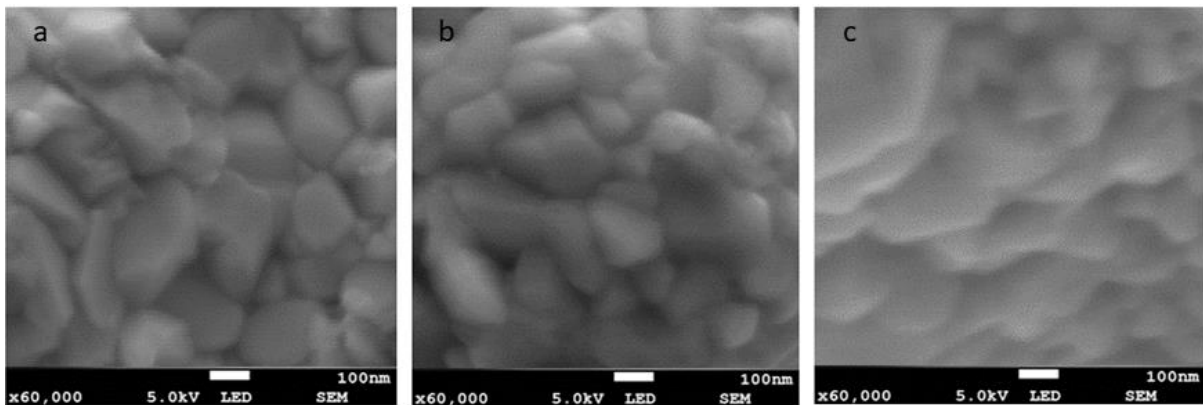
Figure 4.3.2.1: SEM images of CuO coatings electrodeposited at a) 15 min b) 20 min and c) 25 min

4.3.2.2 Atomic force microscopy

Fig.4.3.2.2 (a-c) shows 3D AFM images of nanostructured CuO coatings at 15, 20, and 25-min. From the AFM image at 15 min of deposition time, a relatively uniform and homogeneous surface morphology of CuO coatings was obtained as revealed in Fig.3 (a), indicating the well-crystallinity of the coatings [294]. When the electrodeposition time increased to 20, and 25 min, the AFM images exhibited columnar growth, formation rough surface, and valleys on the surface structure, and increases in grain sizes as shown in Fig. 4.3.2.2 (b, c), confirming that crystallization quality of the coatings is improved [323]. The average surface roughness gradually increased from 17 to 21, and then to 26 nm as the deposition time respectively increased from 15 to 20, and then to 25 min. Surface roughness can determine the absorber surfaces as incident light can be effectively trapped by increasing

of the surface roughness by multireflection [41, 324]. The scattering of light by the surface irregularities in the absorber surface causes the light path length to increase, and then the absorption of CuO coatings can be enhanced [298, 325]. And also, the distribution of the peaks, and valleys in the surface structure leads to effectively trapping more incident light in the inner structure of the coatings, consequently improving the intrinsic absorption of the coatings and thus contributing to better absorption properties [41, 294, 323].
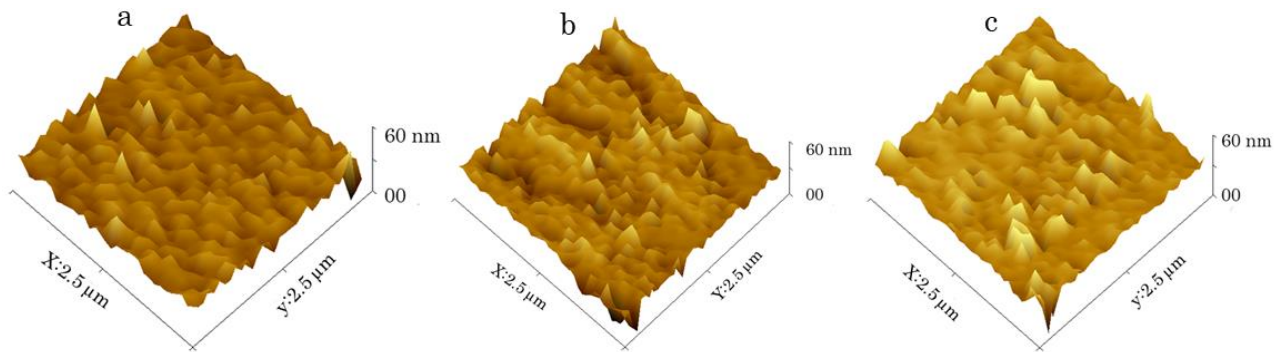
Figure 4.3.2.2: AFM images of CuO coatings electrodeposited at a) 15 min b) 20 min and c) 25 min

4.3.3 Structural and compositional analysis of nanostructure CuO coatings

4.3.3 1 X-ray diffraction

The phase purities, and crystal structure of CuO coatings were evaluated from XRD spectra. Fig 4.3.3.1 (a-c) shows the XRD diffraction pattern of CuO coatings on SS substrate for 15, 20, and 25 min of deposition time. The crystallographic orientations originated at 2θ values of 32.6^o, 35.5^o, 38.6^o, 48.8^o, 53.5^o and 58.2^o corresponding to (110), (11$\bar{1}$), (111), (20$\bar{2}$), (020), and (202) crystal planes of monoclinic structure of CuO, respectively, and it is well-matched with the literature (according to JCPDS card No. 048-1547) [40, 299, 300]. For all coatings, characteristic of diffraction patterns at 2θ values of 43.58° and 50.72° correspond to (111), and (200) planes of fcc of Chromium Iron Nickel ($Cr_{0.19}$ $Fe_{0.7}Ni_{0.11}$) SS substrate, respectively (according to the JCPDS card No. 033-0397). All XRD diffraction peaks can be indexed as typical monoclinic phases, and no other structural phases are observed except the SS substrate. The average crystalline size (D) of CuO coatings is calculated from Scherrer's formula, $D=0.9\lambda/\beta\cos\theta$, where λ is the wavelengths of X-ray radiations, β is the FWHM of the peak at the diffracting angle θ, by determining the width of (11$\bar{1}$) Bragg reflection [302], and found to be 47, 58, and 71 nm at 15, 20 and 25 min of deposition time, respectively, and the results coincides with the trends observed by SEM. The crystallite size increases with the deposition time, thus indicating that the deposition time can contribute to improve of thickness, particle size, and crystallinity of the coatings [303, 306].
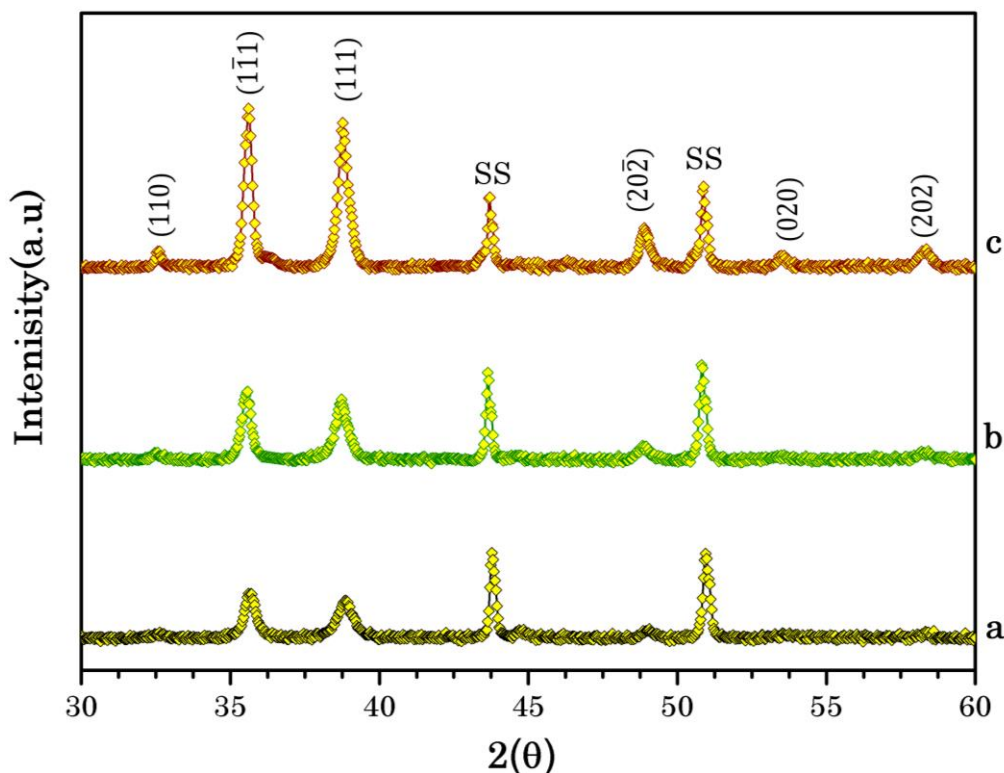
Figure 4.3.3.1: XRD spectra of CuO coatings electrodeposited a) 15 min, b) 20 min and c) 25 min

4.3.3.2 Energy dispersive X-ray spectroscopy

The elemental compositions of electrodeposited nanostructured CuO coatings with nanowall-like structures (observed from SEM) was analyzed by using EDX as shown in Fig. 4.3.3.2 (a-c). The EDX spectrum reveals a strong peaks attributed to Cu, and O indicates the purity phase of the prepared CuO coatings. The EDS results also suggested that the atomic percentage of Cu and O increases with deposition time which compliments with the XRD peak intensity results. The EDX spectral also exhibits weak peak of Cr and Fe from SS substrate.
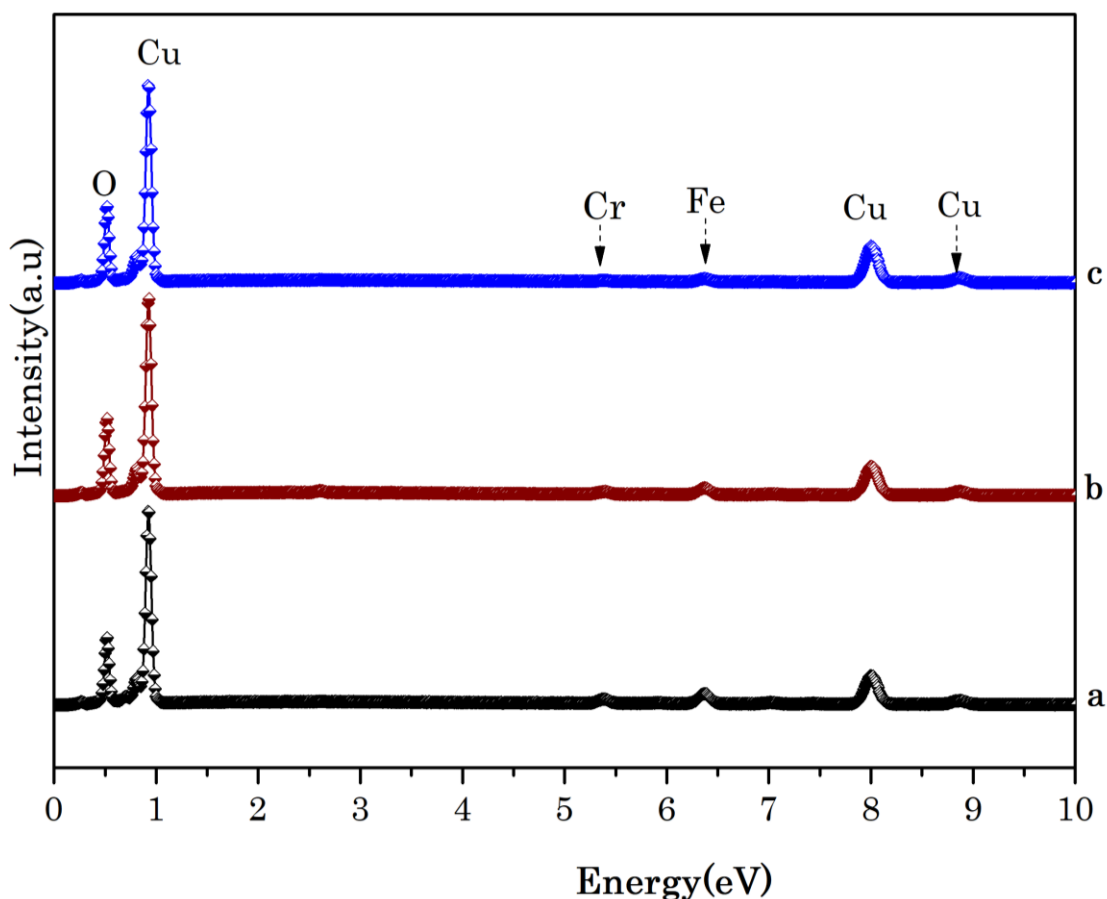
Figure 4.3.3.2: EDS spectra of CuO coatings electrodeposited a) 15 min, b) 20 min and c) 25 min

4.3.3.3 Raman spectroscopy

Raman spectroscopy was applied to investigate the existing lattice vibrations and phases with nanostructured CuO coatings because of its sensitive investigation to the atomic arrangement and lattice vibration of materials [219, 221]. Fig. 4.3.3.3 (a-d) shows Raman spectra of electrodeposited CuO coatings carried out at room temperature using 532 nm radiation for electron excitation. There are twelve optical phonon modes (i.e $4A_u + 5B_u + A1_g + 2B_g$) are in Raman spectrum for CuO, of these only Raman active ($A1_g + 2B_g$) modes are involved in the motion of Cu and O atoms [326, 327]. From the Raman spectra in Fig 4.3.3.3 (a-c), for all coatings three peaks at 305, 348 and 644 cm^{-1} are observed for characteristics of Cu-O stretching modes. The first peak at 305 cm^{-1} is assigned to asymmetric stretch A^1_g mode of CuO along with binding B^1g mode around 344 cm^{-1}, and the symmetric stretching mode appeared at 644 attributed to B^2g. As shown in Fig 4.3.3.3 (a-c), as deposition time increase from 15 to 20 min, and then to 25 min, the intensity of the Raman peak becomes stronger, and sharper that confirms the thickness and crystallinity of the obtained nanocoatings are

improved [221]. Moreover, the Raman spectra of CuO coatings show a peak around 596 cm^{-1} confirms the presence of Cu$_2$O phase [328].
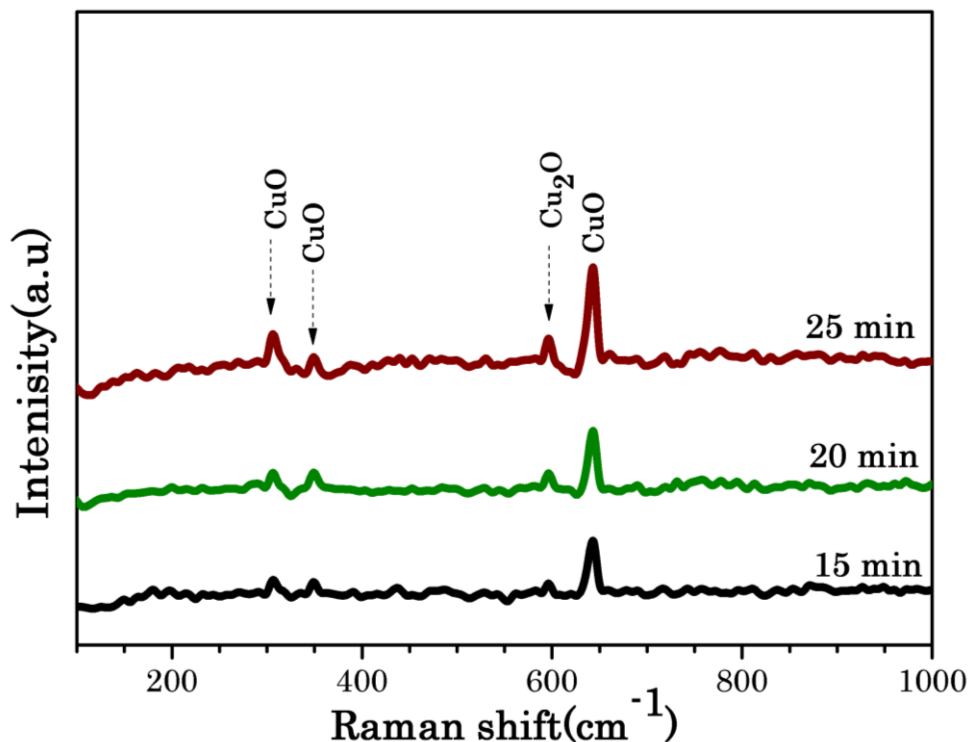
Figure 4.3.3.3: Raman spectra of CuO coatings electrodeposited at (a) 15 min, (b) 20 min, and (c) 25 min

4.3.4 Optical properties nanostructure CuO coatings

The optical property of electrodeposited CuO coatings on SS substrates at different deposition time were characterized by using UV–Vis–NIR, and IR spectrophotometers in the wavelength range of 300–2500nm, and 2500-20000nm, respectively. The solar absorptance (α) and thermal emissivity (ε) values of the coatings were calculated from their diffuse reflectance spectra using eqs.(2.1.1.5), and (2.1.1.10), respectively. Fig.4.3.4 (a, b) shows the diffuse reflectance spectra of the electrodeposited CuO coatings in the solar spectrum (300–2500nm) and IR (2500-20000nm) region, respectively. The diffuse reflectance spectra of the coatings exhibit very low reflectance spectra in the UV-visible region (300–800nm), while above the visible, the diffuse reflectance increases significantly, which confirms the spectral selectivity properties of the coatings due to its intrinsic property, and destructive interferences effect [7,51–53]. In the IR region, the coatings maintain their high reflectance spectra which helps build the absorber with low emissivity(ε); the reflectance spectra is lowering smoothly with increasing of deposition time as shown in Fig.4.3.4 (b). The CuO coating at 15 min exhibits higher reflectance throughout the solar spectrum region and acquires of (α = 0.88 and ε = 0.14). When the deposition time increased to 20 min, the reflectance of the coating was

94

slightly decreased as shown in Fig.4.3.4 (a, b), and both absorptance (α), and thermal emissivity (ε) are gradually increasing respectively to 0.90, and 0.19. Further increase the deposition time to 25 min, the reflectance spectra is lowered, and it achieves higher solar absorptance (α) of 0.92 and emissivity (ε) of 0.23 as revealed in Fig.4.3.4 (a, b).

It is well known that, the CuO coatings thickness is increased with deposition time, this leads to improve grain size of the particles (also confirmed from SEM image). In the solar spectrum the large grain size can improve the light trapping or volume of light-matter interactions between the nanoparticles resulting in lowering reflection, which can enhance solar absorption and leads the absorption edge to shift towards higher wavelengths; consequently, solar absorptance (α) value of the coatings is increased [42, 56, 303]. Moreover, surface roughness is a key factor which leads to increase in the coating solar absorption by decreasing the surface reflection might be with the increasing of roughness in the solar region. On the other hand, in the IR spectrum the thermal emittance (ε) is a function of surface properties especially, the surface roughness of the films. Increasing of surface roughness with thickness can result in light scattering and radiation loss which causes higher emittance (ε) in the IR region. And also, increasing in coating thickness leads to high infrared absorption as well as higher attenuations of light and consequently decreases the reflectance spectra in the IR wavelengths attributing to rise emissivity (ε) value of the coatings. The intrinsic reflectance property of the coatings is much higher in the IR region than in the visible spectrum. In general, the thermal emissivity is a function of surface roughness and is found accordingly to rise with increase in surface roughness of the coatings [303, 305, 315].
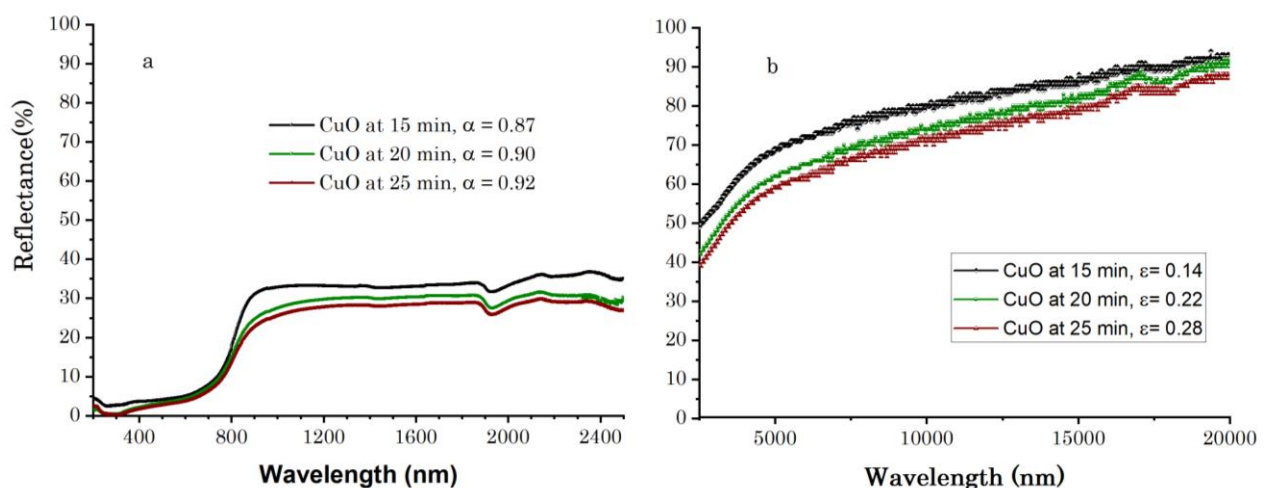
Figure 4.3.4: Reflectance spectra of CuO coatings a) UV-Vis-NIR range b) IR range

4.3.4.1 Optical band-gap energy of CuO coatings

The optical band-gap energy (Eg) of a semiconductor material is the energy required to excite electron from the valence band (VB) to that of the conduction band (CB), and this energy reflects the ability of semiconductor materials to excite electrons from VB to CB as illustrates in Fig.4.3.4.1a. The properties semiconductor properties are strongly affected by the band-gap energy (Eg) parameters.
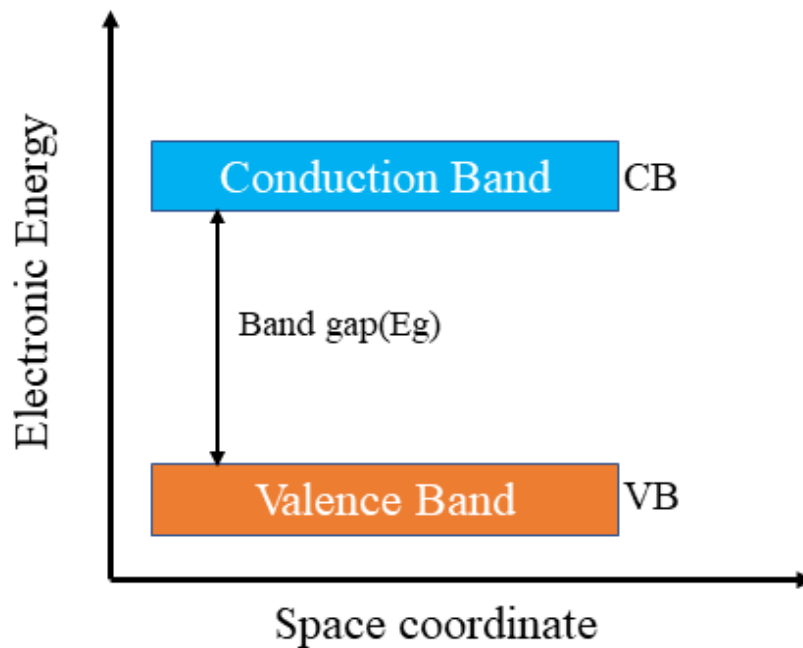
Figure 4.3.4.1 Band gap energy diagram

In semiconductor materials, there are two types of transitions that occur i.e direct transition and indirect transition. The Kubelka-Munk (K-M or F(R)) function is the most employed function to estimate the band-gap energy (Eg) of semiconductor absorbers, like CuO from diffuse reflectance (DR) spectra [329-331], and here, the function is applied to estimate the optical Eg of CuO coatings by using eq.(4.3.4.1a).

$$F(R) = \frac{(1-R)^2}{2R} = \frac{\alpha}{s} \qquad (4.3.4.1a)$$

Where R, α and s are reflectance, absorption and scattering coefficients, the scattering coefficient(s) is dominated by the particle size of the semiconductor material and does very slowly with wavelength range. Hence, in direct transitions the K–M function is approximately proportional to the absorption coefficients (α) of the material or $F(R) \approx \alpha$, and can be obtained by multiply the F(R) function with photon energy (hv) associated with an electronic transition (n) using eq.(4.3.4.1b) [327, 332].

96

$$F(R)hv = \alpha hv = A(hv - E_g)^n \qquad\qquad (4.3.4.1b)$$

Where, A is physical constant or the band edge parameter, Eg is band-gap energy, h is plank's constant, and n is transition band type, for direct transition, n = ½.

Fig. 4.3.4.1 (a) shows UV-Vis-NIR spectrometer reflectance of CuO coatings in the range of 200–1000 nm at 15, 20, and 25 min electrodeposition time, and (b) a plot between the photon energy (hv), and the quantity ($\alpha hv)^2$ to estimate the optical band gap energy of CuO coatings. The optical band gap was estimated by intercept of the straight line with X-axis as displayed in Fig. 4.3.4.1b (b), and the intercepts of this plot on the photon energy (hv) axis gives the band gap of CuO coatings. When the deposition time increases from 15 to 20, and then to 25 min, the spectral reflectance is slightly lowered, as revealed in Fig 4.3.4.1b(a); this enhances solar absorption properties of the coatings [333]. The estimated direct band gap for 15 to 20, and 25 min of deposition time are 1.45, 1.47, and 1.50 eV, respectively and these results are well matched with the literature. Bayansal *et.al* [334] obtained a band gap 1.42 eV for CuO thin film deposited via successive ionic layer adsorption on glass substrate. Moreover, the estimated band gap energy of CuO coatings decreases slightly with deposition time increased, and smaller band gap energies are needed for high solar absorptions [335, 336]. The CuO coating at 25 min of deposition time experiences lower diffuse reflectance spectra in the UV−Vis−NIR region, attributed to its higher absorptivity which can be described by its lower band gap value of 1.45 eV because the lower band gap materials have higher solar absorption above the band gap [331]. The band gap may be influenced by crystallinity, particle growth, and stress of the prepared coatings. The overall crystal structure was improved with the increasing deposition time as observed from XRD results. On the other hand, the grain size could play an important role in the observed reduced band gap values since the grain size of CuO coatings was increased with increase in deposition time and the larger grain size that may cause good absorption (as evident from Fig.4.3.4.1). It is also known that the stress in thin films decreases with an increase in thin film thickness. Improved crystallinity and increased grain size shifting the absorption edge towards higher wavelengths and thereby causing the band gap to shift to lower position [327, 337].
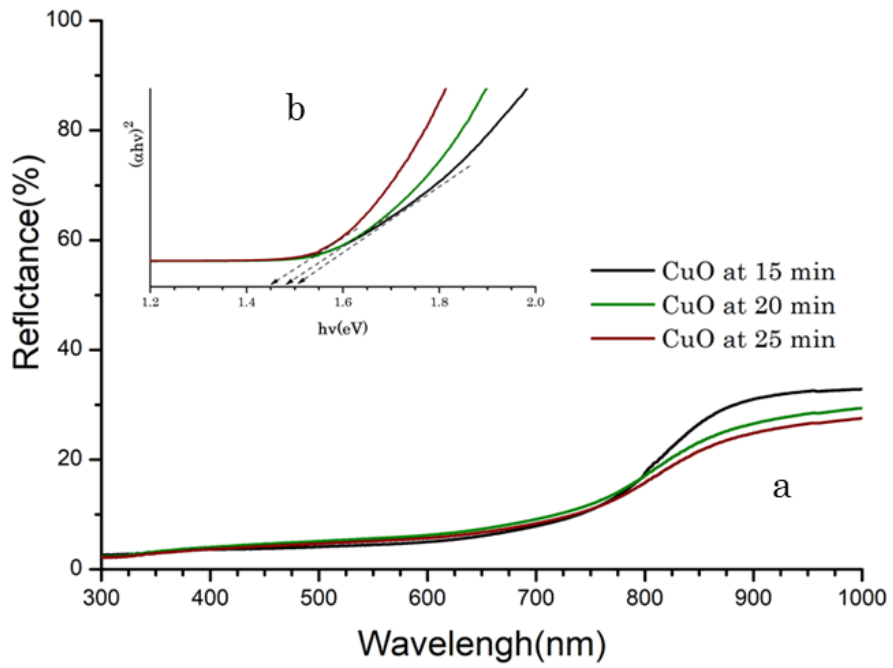
Figure 4.3.4.1: Diffuse reflectance spectra of CuO coatings (a), and estimated band-gap energy (b) of CuO coatings

4.4 Thickness dependent morphological, structural, and optical properties of CuO nanocoatings as solar selective absorber

4.4.1 Sputtering mechanisms and nanostructure CuO formation

Sputtering deposition is one of physical vapor deposition (PVD) techniques that used to produce uniform thin films or coatings on a substrate. The cathodic sputtering process takes place through the ejection or eroding of atoms and/or small clusters from a solid target under the plasma bombardment of energetic positive ions, typically inert gas of Argon (Ar) ions. The collision of inert gas ions or (Ar^+) ions with the target causes the sputtering or releasing of atoms from the target and then condensed on the substrates as a thin film similar to the target materials [338, 339]. Fig. 4.1.1(a) illustrates the sputtering process of Copper (Cu) thin films on SS substrate from Cu target (Cu, 99.99% in purity). Typically, cathodic voltage is applied to the Cu target to start the Argon (Ar) gas ionization. As the gas is ionized, the plasma or vacuum chamber consisting of electrons and the positively charged Ar^+ ions. The positively charged (or Ar^+) ions hitted the Cu target with kinetic energy proportional to the Cu target. Above an energy threshold, the Cu target atoms are started to eject and travel across the vacuum chamber and eventually condensed on SS substrate surface [338-340]. The thickness of the Cu films was controlled by deposition time and found to be 300, 400, 500, and 600 nm at 1.00, 1.15, 1.30, and 1.45 h, respectively.
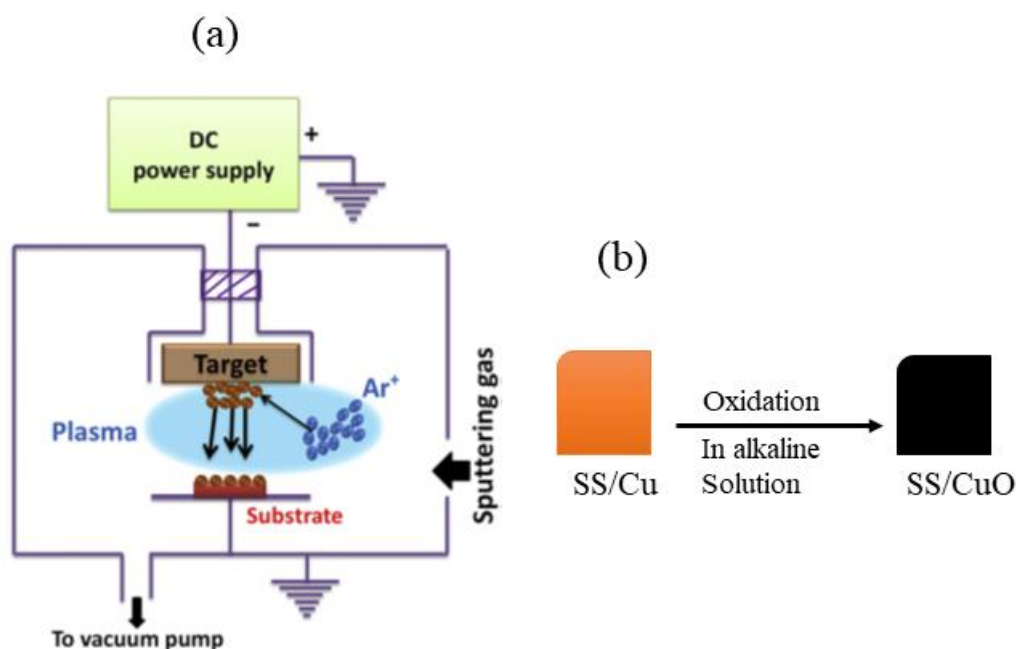
Figure 4.4.1: a) Sputtering process of Cu thin films, and b) thermal oxidation of deposited Cu film to CuO

The chemical reaction mechanisms that were involved in the formation of nanostructure CuO coatings on SS substrates at room temperature described below (eqs.(4.1.1a-d). The deposited Cu films of SS substrates were successfully oxidized into nanostructure CuO by immersed the Cu film in alkaline aqueous solution that contains KOH and $K_2S_2O_4$. The chemical reaction is simply an oxidation-dehydration process.

$$Cu + 2KOH + K_2S_2O_8 \longrightarrow 2K_2SO_4 + Cu(OH)_2 \tag{4.1.1a}$$

$$Cu(s) \longrightarrow Cu^{2+}(aq) + 2e^- \tag{4.1.1b}$$

$$Cu^{2+}(aq) + 2OH^- \longrightarrow Cu(OH_2)(aq) \tag{4.1.1c}$$

$$Cu(OH)_2(aq) \longrightarrow CuO + H_2O \tag{4.1.1d}$$
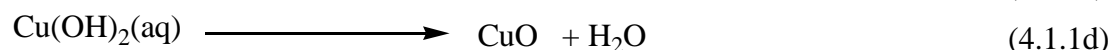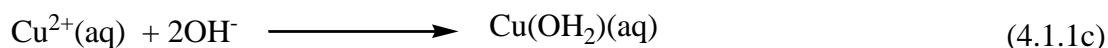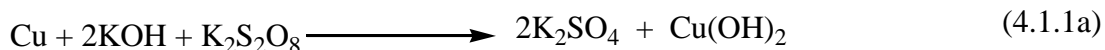
When the deposited Cu film is dipped into the alkaline solution, it starts to released Cu^{2+} ions. The presence of potassium hydroxide (KOH) accelerated the formation of Cu^{2+} ions from the Cu film in the reaction medium and enhanced the oxidization process of Cu film. The ionized Cu^{2+} ions then react with the OH$^-$ ion and resulted the formation of copper hydroxide $(Cu(OH)_{2(aq)}$ (eq.(4.1.1.1(c)). The formed $Cu(OH)_{2(aq)}$ act as nuclei, and increasing the growth of nuclei in the subsequent reactions influenced the stability of $Cu(OH)_2$ in the reaction medium and then converted to the nanoflake-like surface of CuO [52, 172, 341-345]. Finally, the formed CuO coatings is crystalized at 100 ºC in a vacuum furnace.

4.4.2 Surface morphology of CuO nanocoatings

4.4.2.1 Scanning electron microscopy

The morphological surface of the obtained CuO nanocoatings was investigated using Scanning electron microscopy (SEM). Fig.4.4.2.1 show SEM images of CuO nanocoatings on SS substrate at 300, 400, 500, and 600 nm. From Fig. 4.4.2.1(a) as deposited uniform nanosquare-like surfaces of Cu was observed at 300 nm coating thickness. The nanosquare-like surfaces of Cu coatings are changed to vertically aligned nanoflake surfaces of CuO after the Cu coatings were oxidized in alkaline solution as shown in Fig. 4.4.2.1(b, c). The nanoflake surfaces are well distributed and uniform, However, further increased the thickness to 500, and 600nm, the nanoflake surface is transformed to densely rice-leave-like surfaces as revealed in Fig. 4.4.2.1(d, e). Moreover, growth of some agglomerated particles is observed from denser, and compacted nanocoatings. The spaces or pores with in the surface of the coatings enables to enhance the solar absorption of the CuO nanocoatings [75, 346]. The particle size of CuO nanocoating is found to be 26.65, 39.50, 50.24, and 59.60 nm for 300,

400, 500, and 600 nm of coating thicknesses, respectively, these results confirm that crystallinity of the CuO nanocoating is improved with increasing of the coating thicknesses [36, 347].
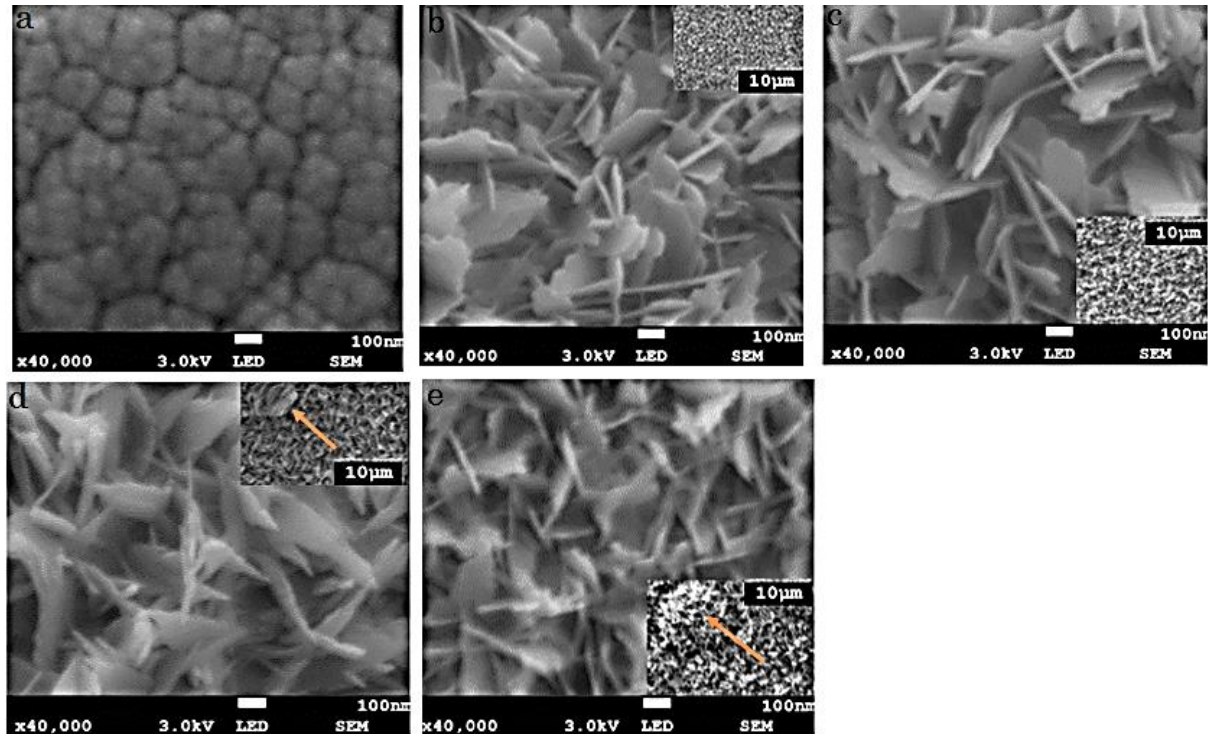
Figure 4.4.2.1: SEM images of Cu 300 nm (a), and CuO 300-600 nm (b-e) as a function of thickness

4.4.2.2 Atomic force microscopy

The surface morphology and average surface roughness of CuO nanocoatings were further investigated using atomic force microscopy (AFM). Fig. 4.4.2.2 demonstrates the 3D AFM images of CuO on SS substrate at 300, 400, 500, and 600 nm of coating thickness. As shown in, Fig. 4.4.2.2(a), as deposited Cu coating is uniform, and homogeneous surfaces is observed with average surface roughness of 9.9 nm. After the Cu coatings were oxidized into CuO a rough surface is observed. The CuO nanocoatings mainly consist of uniformly distributed and congruent vertical grains at 300, and 400 nm coatings thickness with 21.55 and 24.03 nm average surface roughness, respectively as shown in Fig. 4.4.2.2 (b, c). when the coating thickness increased to 500, and 600 nm, structural evolution as well as grain growth are observed, and the surface roughness of the coatings is increased respectively to 26.10, and 28.36 nm. Noticeably, the surface roughness of the coatings is gradually increased with a thickness accompanying with grains growth which can increase the scattering of short waves to trap more photons in the solar regions, and the reflection of long waves [346, 348, 349].
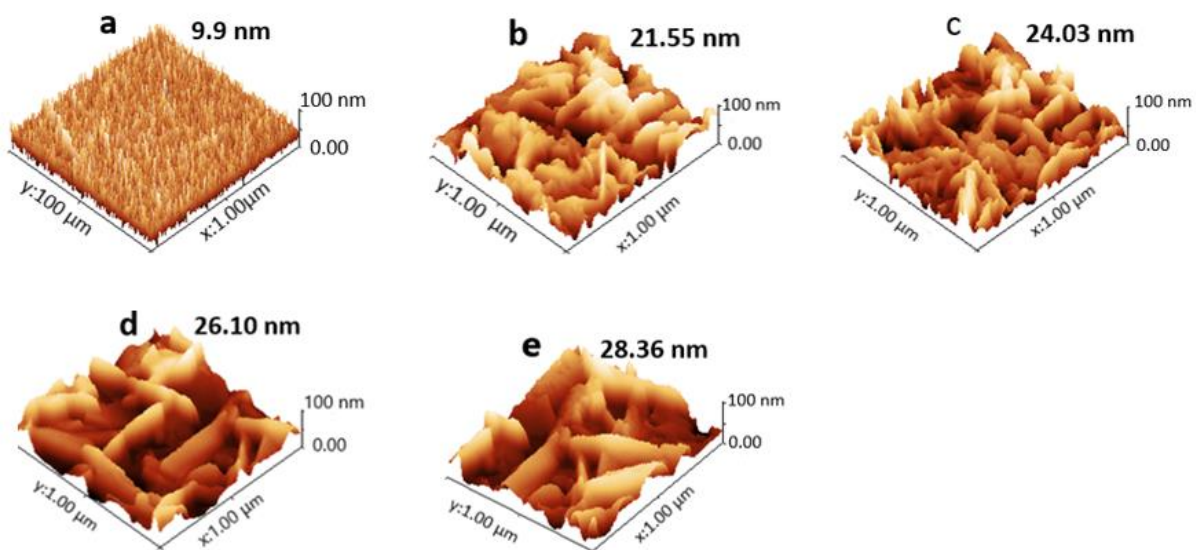
Figure 4.4.2.2: AFM images of Cu 300 nm (a), and CuO 300-600 nm (b-e) film thickness.

4.4.3 Structural, and compositional analysis of CuO nanocoatings

4.4.3.1 X-ray diffraction

The structural properties of the obtained CuO nanocoatings were investigated using X-ray diffraction (XRD). Fig. 4.4.3 illustrates diffraction peaks of Cu (a) metal and CuO (b-e) deposited on SS substrate at 300, 400, 500, and 600 nm coating thickness. For all the coatings, the diffraction peaks originated at 2θ of 43.38° and 50.42° corresponding to (111), and (200) planes of fcc phase of Cu metal, respectively. The XRD peaks at 2θ of 35.5° and 38.4° associated to (002), and (200) crystal planes of monoclinic structure of CuO, respectively (according to the JCPDS card No. 80-1917) [40, 299, 300] as shown in Fig. 4.4.3.1 (b-e). The diffraction peaks does not reveal peaks attributed to cupreous oxide (Cu_2O) indicate that either Cu_2O does not exist or the proportion of Cu_2O is low. The peak referenced by 'SS' centered at 2θ of 74.70° is from SS substrate. The diffraction peak intensities is increased as a coating thickness increases indicating that the crystallinity nature of the monoclinic structure of CuO nanocoatings is improved [323].
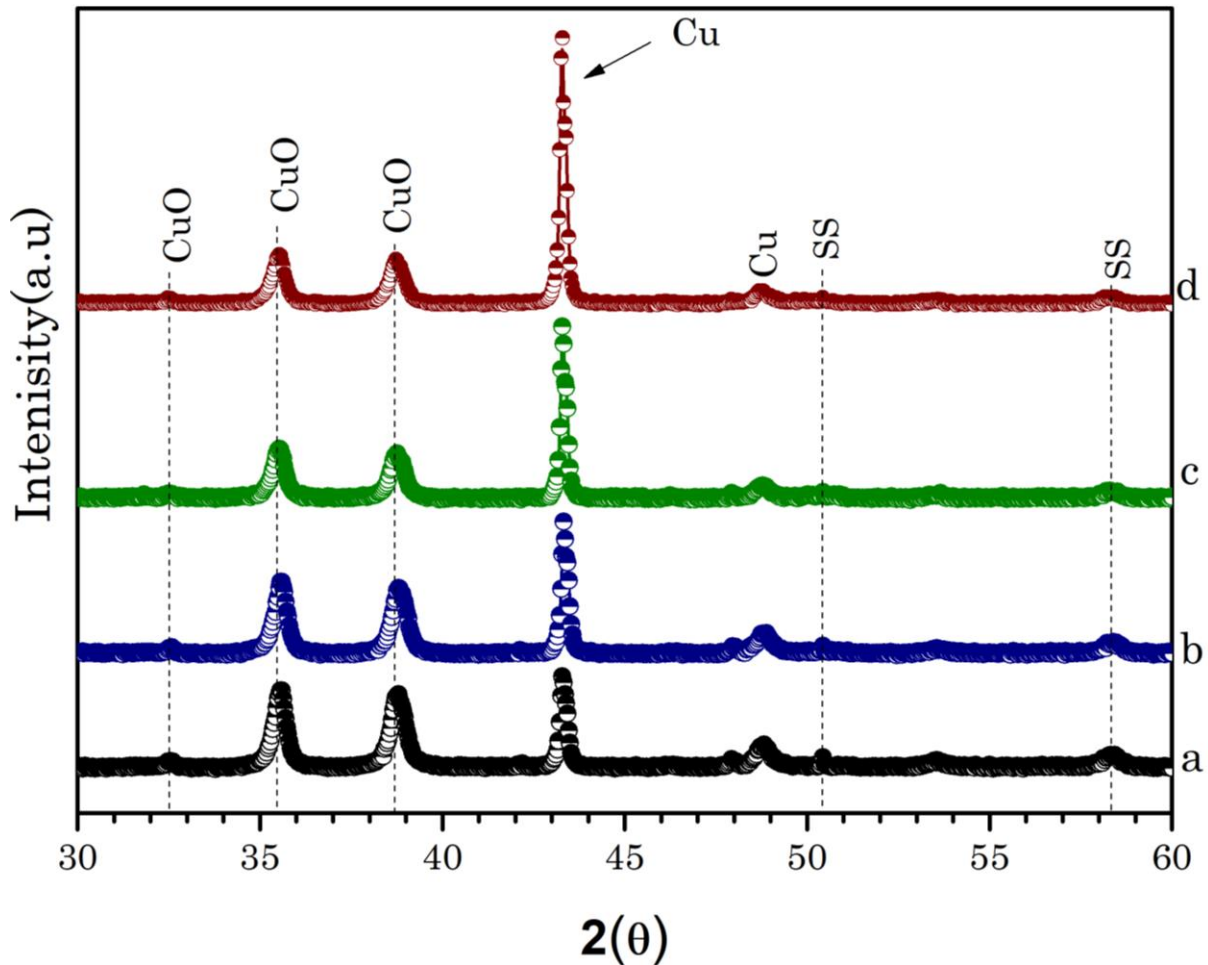
Figure 4.4.3.1: XRD of CuO (a-d) 300-600 nm coatings thickness

4.4.3.2 Energy dispersive spectroscopy

The elemental composition of CuO nanocoatings was analyzed using Energy dispersive spectroscopy (EDS). As deposited from Fig.4.4.3.2 (a), a strong peak corresponding to Cu metal only is observed. From Fig.4.4.3.2 (b-e) in addition to Cu peaks, a peak attributed to O is observed in the spectra, confirms that the purity of obtained CuO. EDX result also suggests that the atomic percentage of Cu and O are increased with increases of thickness of the coatings which is compliment with the XRD results. The EDX spectra also shows weak peaks of chromium Cr and C originating from SS substrate and carbon, respectively.
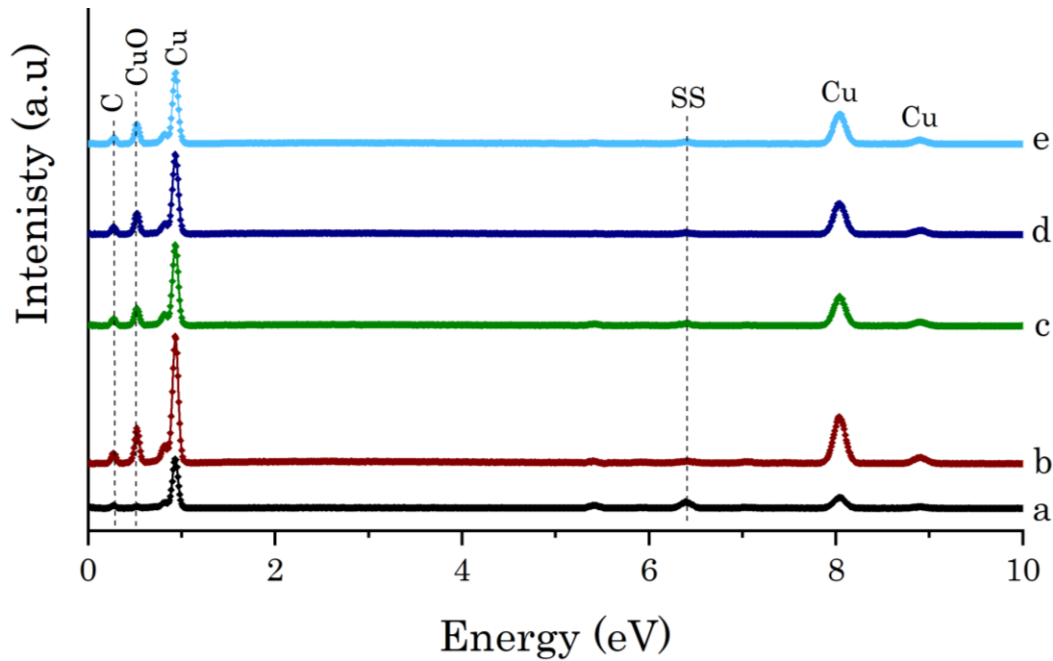
Figure 4.4.3.2. EDX spectra of Cu 300 nm (a), and CuO 600-300 nm (b-e) film thickness

4.4.4 Optical properties of CuO nanocoatings

The optical properties of CuO nanocoatings on SS substrate were characterized using UV–Vis–NIR, and IR spectrometers in the wavelength of 300–2500 nm, and 4000-20000 nm, respectively. The SS substrate as a substrate has been extensively studied, and it exhibits (α,ε) of 0.36 and 0.14, respectively [6, 350]. The solar absorptance (α), and thermal emissivity (ε) values of the coatings were calculated from their diffuse reflectance spectra using eqs.(2.1.1.5), and (2.1.1.10), respectively to analyse their spectral selectivity. Fig.4.4.4(a,b), depicts the detailed diffuse reflectance characteristics of CuO, respectively, in the solar and IR spectrum. From Fig.4.4.3 (a, b), the Cu coatings have the highest reflectance spectra with solar absorptance (α= 0.57) in the solar spectrum and emissivity of (ε=0.18) in the IR region due to large concentrated free electrons in metals which shows high nature of reflectance both in the wavelength of range solar spectrum, and IR region [351, 352].

Fig.4.4.4 (a) displays the reflectance spectra of CuO nanocoatings in the solar spectrum (300-2500 nm). For all nanocoatings, the reflectance spectra is almost close to zero (0) in the visual wavelength (400-800 nm) region and show negligible variation, while above the UV-visible region (400-2500 nm), the reflectance spectra is rather high confirms that CuO nanocoating surfaces have good intrinsic absorption properties [13, 27, 53, 151]. Above the visible region (or from 800-2500 nm) all the coatings reveal lower reflectance (< 18%) and acquire a solar absorptance (α = 0.94) at 300 nm of coating thickness. The reflectance spectra

of the coatings are decreased as the thickness of the coatings increased to 400, and 500 nm, and thus a high absorption with solar absorptance of (α = 0.95, and 0.96) is observed respectively. Further increasing to 600 nm, the reflectance spectra is lowered, strong and broad absorption is occurred and exhibits an excellent absorption (α = 0.97) as revealed in Fig.4.4.4 (a). Clearly, the results confirm that as the coating thickness increases, the absorption edge expands to near-infrared region and achieved broader absorption in solar spectrum, due to the volume light-matter interactions increases, which enhances light absorptions of the coatings. Moreover, both particle size and surface roughness of CuO coatings are gradually increasing with thickness of the coatings which are beneficial for efficiently capturing more photons in the solar spectrum region. In the contrary, higher average surface roughness can result in radiation loss by increased thermal emittance (ε) of the coatings [36, 349, 353-355].
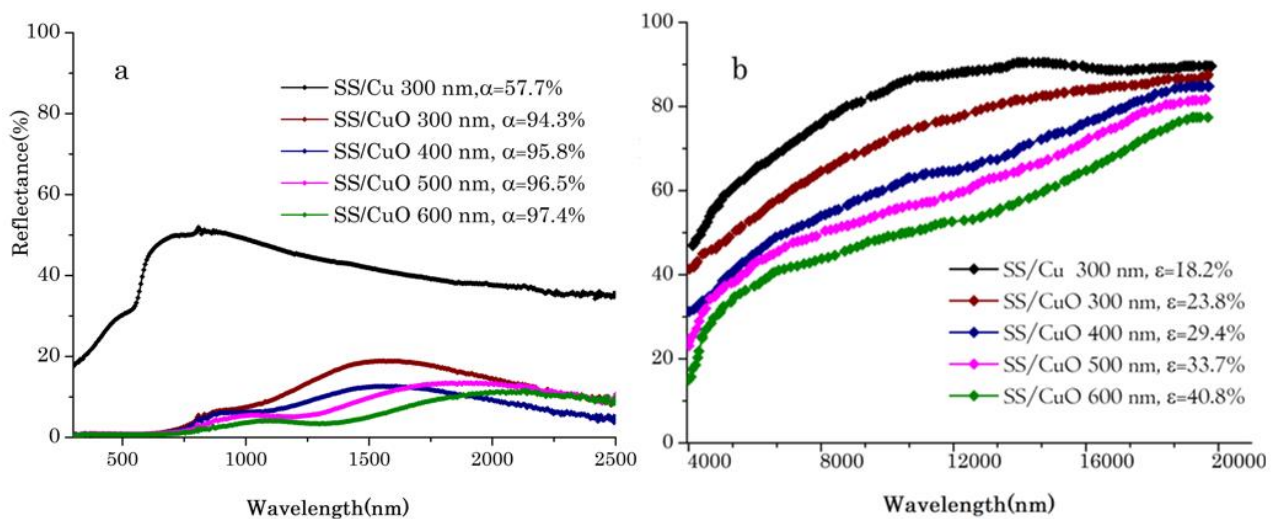
Figure 4.4.4: Diffuse reflectance spectra of CuO nanocoatings a) solar spectrum b) IR spectrum

Conversely, the thermal emissivity (ε) of the nanocoatings was analyzed using IR from 4000-20000nm wavelength as displayed in Fig.4.4.3 (b). The CuO shows higher spectral reflectance near to 90%, and it exhibits emissivity (ε) of 0.23 at 300nm. When the thickness is increased to 400, 500 and 600nm, the reflectance spectra is lowered, and thus, the emissivity (ε) of the nanocoatings is gradually increasing, respectively to 0.29. 0.33 and 0.40. The infrared emissivity (ε) of the obtained coatings are increasing with the thickness attributed with different effects, specifically surface properties. Increasing in coating thickness causes to have high infrared absorption can lead to higher attenuation of light in the IR region; consequently, the reflectance of the coatings is lowered, which is attributed to rise

the emissivity (ε) of the coatings in the infrared wavelengths [67, 303]. Moreover, the spaces or pores between nanoparticles can enhance the average surface roughness of the coatings (observed from AFM), this can cause light scattering and radiation losses which leads to lower reflectance spectra in the IR spectrum. The reduction of reflectance spectra inversely increased in the emissivity (ε) of coatings [51, 151, 349, 354].

4.4.4.1 Optical band gap energy

Band-gap energy (Eg) reflects the ability of semiconductor materials to excite electrons from VB to CB. The optical band-gap energy is crucial in predicting solar absorption property of semiconductor materials. The Kubelka-Munk (K-M) function is the most common to estimate Eg of semiconductor materials from their diffuse reflectance spectra. Diffuse reflectance is a non-destructive technique for surface examination and in particular to estimate the Eg and optical properties of semiconductor materials like CuO [329, 330, 356]. To calculate the optical Eg from diffuse reflectance spectra of CuO, here the K–M function F(R) is applied using eqs(4.3.4.1a), and (4.3.4.1b) [327, 332, 356].

 Fig. 4.4.3.1b shows the diffuse reflectance (a), and estimated Eg (b) of CuO. The reflectance spectra is decreased as the coatings thickness increases from 300 to 600 nm, as shown in Fig. 4.4.4.1 (a), this enables to improve solar absorptions of the coatings [333]. The optical Eg is estimated by the intercept of the straight line with X-axis as shown in Fig. 4.4.3.1 (b), and optical Eg values are found to be 1.62, 1.45, 1.34, and 1.27 eV at 300, 400, 500, and 600 nm coatings thickness, respectively, and these results are well-matched with the literature. Bayansal *et.al* [334] demonstrated CuO film on glass substrates via successive ionic layer adsorption and obtained 1.42 eV of Eg, and also Shahid *et.al* [329] prepared CuO via hydrothermal and reported a Eg of 1.34 eV. Moreover, the estimated Eg values are gradually decreased with increased coating thicknesses, and smaller Eg values are needed for higher solar absorptions [335, 336].
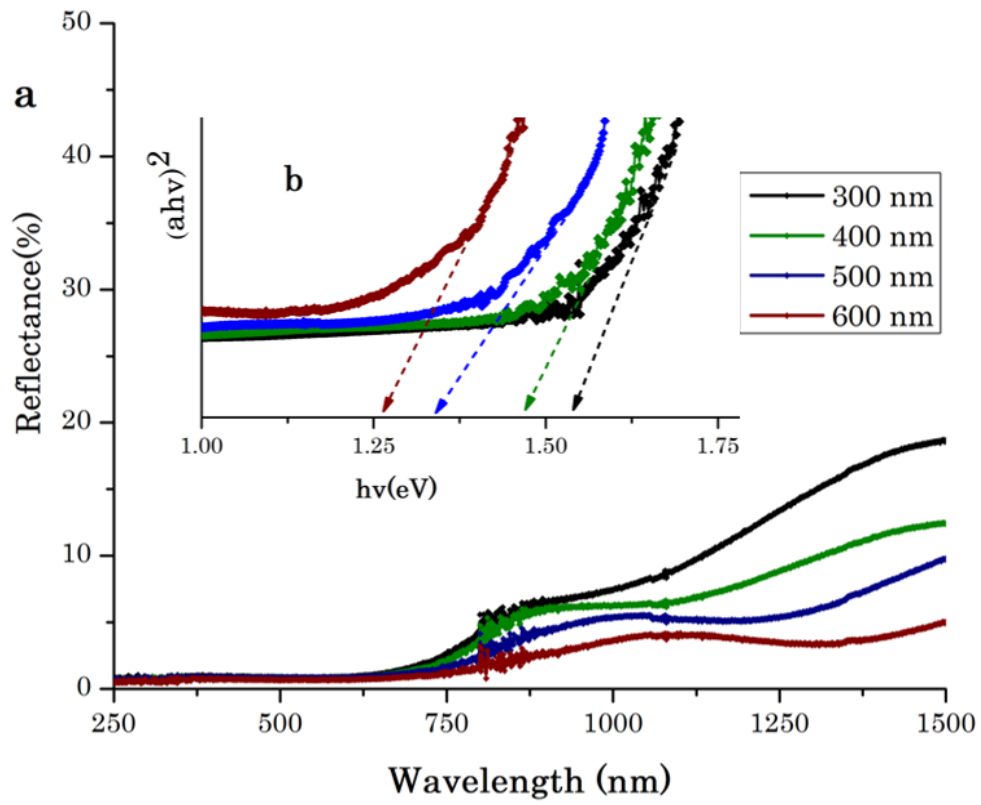
Figure 4.4.4.1: Diffuse reflectance (a), and bandgap values (b) of CuO nanocoatings

CHAPTER FIVE

CONCLUSION

Due to climate change and gradual increase of global energy consumption studies on renewable energy sources for clean and sustainable growth are needed. Solar energy is becoming indispensable as it is a source of clean environmental energy, bountiful and inexhaustible. Solar-to-thermal energy conversion is considered as a direct method of harnessing and converting solar radiation into thermal, and then to thermophotovoltaics for various potential applications. In solar-to-thermal energy systems nanostructured absorber surfaces enable to enhance the conversation efficiency of the solar radiation to thermal energy by manipulating spectral selectivity properties ranging from solar spectrum region (300–2500 nm) to mid-infrared (IR) spectrum (2500–25000 nm). The conversion solar to thermal energy can be improved using of solar selective absorber (SSA) surfaces consisting of semiconductor and/or novel plasmonic nanoparticles that are incorporated in semiconductor matrix. In this research work, green-synthesized single-layered CuO nanocoatings, and Ag@CuO nanocermet coatings deposited on SS substrates using spin-coater at different rotational speed (RS) and also CuO via electrochemical and Radio frequency (RF) sputtering depositions as SSA surfaces were investigated. The influences of synthesis methods on the morphological, structural, and optical properties of the obtained coatings were studied. The results clearly showed that synthesis methods and the thickness of the coatings have a significant effect on the morphological and optical properties of the coatings. The SEM confirms that the surface of CuO nanocoatings varies with synthesis methods, and thus, nanorods, nanowalls, and nanoplates CuO surfaces are observed from the green synthesis, electrochemical, and sputtering methods, respectively. The XRD confirms the presence of crystal monoclinic phase structure of CuO. The incorporating Ag NPs does not affect the monoclinic phase structure CuO, even if it affected the nanorod like-surfaces of CuO and XRD peak intensities. EDX and Raman spectra confirm the purity of elemental composition and lattice vibrational within the coatings, respectively. The RBS experiment revealed the elemental concentration and changes in the thickness with rotational speed of the spin coater. The optical properties of all coatings were deduced from UV-Vis-NIR and IR spectrometers reflectance measurements in the solar spectrum and IR region, respectively, and the optimized coatings exhibited a high solar absorptance ($\alpha > 0.90$). The broader and highest solar absorptance ($\alpha \approx 0.97$) value is achieved using RF sputtering method even if the

emissivity (ε = 0.40) is high. The absorption edge of the coatings is slightly shifted towards higher wavelengths as thickness increased, this enable to increase solar absorption in solar spectrum, while the emissivity (ε) of the coatings is decreased. Both the solar absorptance (α) and emissivity (ε) values of the coatings are gradually increased as the thickness of coatings is increased because of the intrinsic absorption properties and higher attenuation of light, respectively. The optical band-gap energy of CuO nanocoatings was estimated from the diffuse reflectance spectra and found to decreased as solar absorption properties of the coatings was increased; this may be influenced by several parameters such as crystallinity, grain growth, and stress of the coatings.

RECOMMENDATIONS

Although nanostructure CuO nanocoatings, and Ag@CuO nanocermet coatings were successfully prepared, and characterized as solar selective absorber surfaces using green synthesis, electrodeposition, and sputtering methods, the thermal stability of the coatings at low temperature (≤ 100 ^{o}C), and med-temperature ($100 \leq T \leq 400$ ^{o}C) are under ongoing investigations and its preliminary results of CuO show the material could be applicable for medium temperature applications.

REFERANCES

[1] Xu, K., *etal, High temperature solar selective absorber coatings for solar thermal application.* Materiomics, 2019.

[2] Mandal, D., *etal, Fabrication of a Wide Angle Plasmonic Selective Absorbers for HighEfficiency Solar Thermal Energy Conversions.* Advanced Materials, 29(2017)1702156.

[3] Hadke, S., *etal, Emerging Chalcogenide Thin Films for Solar Energy Harvesting Devices.* Chemical Reviews, 2021.

[4] Chang, C., *etal, 3D porous solar driven interfacial evaporator for high-efficiency steam generations.* American chemical society, 4(2019) 3546-3555.

[5] Yi, F., *etal, Solar thermal driven capacitanceenhancement of super-capacitors.* Energy & Env. Science, 11(2018)2016-2024.

[6] Cao, F., *etal, A high temperaturestable spectrally selective absorbers based on cermet of titaniumnitride in SiO₂.* Solar Energy Materials and Solar Cells, 100(2017)12-17.

[7] Balzani, V., *etal, Photochemicalconversion of solar energy.* Chemistry & Sustainability Energy & Materials, 1(2008) 26-58.

[8] Ren, H., *etal, Hierarchical graphene foam for efficientomnidirectional solar to thermal energy conversions.* Advanced materials, 29(2017)1702590.

[9] Cao, F., *etal, Temperature stable spectrally-selective solar absorbers based on cermet of titanium nitride in SiO2.* Solar Energy Materials and Solar Cells, 160(2017)12-17.

[10] Nuru, Z.Y., *etal, Pt–Al2O3 nanocoatings for high temperature concentrated solarthermal power applications.* Physica B: Condensed Matter, 407(2012)1634-1637.

[11] Xu, K., *etal, A review of high-temperature selective absorbing coatings for solar thermal application.* Materiomics, 6(2020)167-182.

[12] Kennedy, C.E., *Review of mid-to high-temperature solarselective absorber materials*, National Renewable Energy -2002

[13] Cao, F., *etal, Enhanced Thermal Stability of W-Ni-Al2O3Cermet Based Spectrally Selective Absorber with Tungsten(W) Infrared Reflector.* Advanced Energy Materials, 5(2015)1401042.

[14] Khamlich, S., *etal, Annealing effect on the structural and optical property of Cr/α-Cr2O3 monodispersedparticles based solar absorbers.* Applied Surface Science, 265(2013)745-749.

[15] Song, P., *etal, The investigation of thermalstability of Al/NbMoN/NbMoON/SiO2 absorbing coatings.* Solar Energy Materials and Solar Cells, 171(2017)253-257.

[16] Karoro, A., Z.Y. Nuru, L. Kotsedi, K. Bouziane, B.M. Mothudi, and M. Maaza, *Laser nanostructured Co nanocylinders-Al2O3 cermets for enhanced & flexible solar selective absorbers applications.* Applied Surface Science, 347(2015) 679-684.

[17] Dan, A., Harish C., Chattopadhyay, Kamanio, Basu, Bikramjit, *Solar energy absorption mediated by surface plasma polariton in spectrally selective dielectric metal dielectric coatings:* Renewable and Sustainable Energy, 79(2017)1050-1077.

[18] Chen, M., J. Mandal, Q. Ye, A. Li, Q. Cheng, T. Gong, T. Jin, Y. He, N. Yu, and Y. Yang, *A Scalable Dealloying Technique To Create Thermally Stable Plasmonic Nickel Selective Solar Absorbers.* ACS Applied Energy Materials, 2019.

[19] Ehrenreic, H., *Symposium on the Fundamental Optical Properties of Solids Relevant to Solar Energy Conversion.* NASA STI/Recon Technical Report N, 77(1975)

[20] González, F., E. Barrera-Calva, L. Huerta, and R.S. Mane, *Coatings of Fe3O4 nanoparticles as selective solar absorber.* The Open Surface Science Journal, 3(2011) 131-135.

[21] Ienei, E., L. Isac, and A. Duta, *Synthesis of alumina thin films by spray pyrolysis.* Revue Roumaine de Chimie, 55(2010) 161-165.

[22] Moon, J., D. Lu, B. VanSaders, T.K. Kim, S.D. Kong, S. Jin, R. Chen, and Z. Liu, *High performance multi-scaled nanostructured spectrally selective coating for concentrating solar power.* Nano Energy, 8(2014) 238-246.

[23] Wang, K., Z. Wu, C. Peng, K. Wang, B. Cheng, C. Song, G. Han, and Y. Liu, *A facile process to prepare crosslinked nano-graphites uniformly dispersed in titanium oxide films as solar selective absorbers.* Solar Energy Materials and Solar Cells, 143(2015) 198-204.

[24] Antonaia, A., A. Castaldo, M. Addonizio, and S. Esposito, *Stability of W-Al2O3 cermet based solar coating for receiver tube operating at high temperature.* Solar Energy Materials and Solar Cells, 94(2010) 1604-1611.

[25] Adsten, M., R. Joerger, K. Järrendahl, and E. Wäckelgård, *Optical characterization of industrially sputtered nickel–nickel oxide solar selective surface.* Solar energy, 68(2000) 325-328.

[26] Nuru, Z.Y., D. Perez, K. Kaviyarasu, A. Vantomme, and M. Maaza, *Annealing effect on the optical properties and interdiffusion of MgO/Zr/MgO multilayered selective solar absorber coatings.* Solar Energy, 120(2015) 123-130.

[27] Nuru, Z.Y., J. Sackey, L. Kotsedi, N. Matinise, C. Ndlangamandla, and M. Maaza, *Structural and optical properties of ZrOx/Zr/ZrOx/AlxOy multilayered coatings as selective solar absorbers.* Journal of Alloys and Compounds, 773(2019) 975-979.

[28] Xue, Y., C. Wang, W. Wang, Y. Liu, Y. Wu, Y. Ning, and Y. Sun, *Spectral properties and thermal stability of solar selective absorbing AlNi–Al2O3 cermet coating.* Solar Energy, 96(2013) 113-118.

[29] Selvakumar, N., N.T. Manikandanath, A. Biswas, and H.C. Barshilia, *Design and fabrication of highly thermally stable HfMoN/HfON/Al2O3 tandem absorber for solar thermal power generation applications.* Solar Energy Materials and Solar Cells, 102(2012) 86-92.

[30] Kumar, S.K., S. Suresh, S. Murugesan, and S.P. Raj, *CuO thin films made of nanofibers for solar selective absorber applications.* Solar Energy, 94(2013) 299-304.

[31] Wang, J., Z. Chen, and D. Li, *Simulation of two-dimensional Mo photonic crystal surface for high-temperature solar-selective absorber.* physica status solidi (a), 207(2010) 1988-1992.

[32] Rydosz, A., A. Brudnik, and K. Staszek, *Metal Oxide Thin Films Prepared by Magnetron Sputtering Technology for Volatile Organic Compound Detection in the Microwave Frequency Range.* Materials (Basel), 12(2019).

[33] Zhu, L., M. Gao, C.K.N. Peh, and G.W. Ho, *Solar-driven photothermal nanostructured materials designs and prerequisites for evaporation and catalysis applications.* Materials Horizons, 5(2018) 323-343.

[34] Gao, F., Y. Yao, W. Wang, X. Wang, L. Li, Q. Zhuang, and S. Lin, *Light-driven transformation of bio-inspired superhydrophobic structure via reconfigurable PAzoMA microarrays: from lotus leaf to rice leaf.* Macromolecules, 5(2018) 2742-2749.

[35] Liu, H., H. Fu, Y. Liu, X. Chen, K. Yu, and L. Wang, *Synthesis, characterization and utilization of oxygen vacancies contained metal oxide semiconductor for energy and environmental catalytic.* Chemosphere, 272(2021)129534.

[36] Chan, K.-Y., Bee-San, *Atomic force microscopy and X-ray diffraction investigation of copper thin films prepared by dc magnetron sputtering technique.* Microelectronics, 37(2006)1064-1071.

[37] Vakulov, D.A. Khakhulin, and O.A. Ageev, *Thermal stability of ZnO thin films fabricated by pulsed laser deposition.* Materials Science in Semiconductor Processing, 66(2017) 21-25.

[38] Ollier, E., N. Dunoyer, H. Szambolics, and G. Lorin, *Nanostructured thin films for solar selective absorbers and infrared selective emitters.* Solar Energy Materials and Solar Cells, 170(2017) 205-210.

[39] Prakash, S., N. Elavarasan, A. Venkatesan, K. Subashini, M. Sowndharya, and V. Sujatha, *Green synthesis of CuO nanopartcles and its application in Biginelli reaction, BTB photo-degadation and antibacterial activities.* Advanced Powder Technology, 29(2018)3315-3326.

[40] Karthick, S., S.M. , and S. Suresh, *Preparation and characterization of CuO nanostructures on copper substrate as selective solar absorbers.* Materials Chemistry and Physics, 143(2014) 1209-1214.

[41] He, M., Y. Wang, H. Wang, and R. Chen, *A one-step sol–gel route derived Ag–CuO film as a novel solar selective absorber.* Solar Energy Materials and Solar cells, 144(2016) 264-272

[42] Prasanth, D., K. Sibin, and H.C. Barshilia, *Optical properties of sputter deposited nanocrystalline CuO thin films.* Thin Solid Films, 673(2019) 78-85.

[43] Welegergs, G., H. Gebretinsae, R. Akoba, N. Matinsie, Z. Nuru, and M. Maaza, *Electrochemical properties of green synthesised Zinc oxide (ZnO) Nanoparticles.* MRS Advances, 5(2020) 1103-1112.

[44] Rajeshkumar, S. and L. Bharath, *Mechanism of plant-mediated synthesis of silver nanoparticles–a review on biomolecules involved, characterisation and antibacterial activity.* Chemico-biological interactions, 273(2017) 219-227.

[45] Karthik, L., A.V. Kirthi, S. Ranjan, and V.M. Srinivasan, *Biological synthesis of nanoparticles and their applications*. 2019.

[46] Tsegay, M., H. Gebretinsae, G. Welegergs, M. Maaza, and Z. Nuru, *Novel green synthesized Cr2O3 for selective solar absorber: Investigation of structural, morphological, chemical, and optical properties.* Solar Energy, 236(2022) 308-319.

[47] Nuru, Z.Y., *Spectrally selective AlXOY/Pt/AlXOY solar absorber coatings for high temprature solar-thermal applications,* 2014.

[48] Carrasco, J.M., L.G. Franquelo, J.T. Bialasiewicz, E. Galván, R.C. PortilloGuisado, M.M. Prats, J.I. León, and N. Moreno-Alfonso, *Power-electronic systems for the grid integration of renewable energy sources: A survey.* IEEE Transactions on industrial electronics, 53(2006) 1002-1016.

[49] Khelifa, A., S. Khamlich, Z. Nuru, L. Kotsedi, A. Mebrahtu, M. Balgouthi, A. Guizani, W. Dimassi, and M. Maaza, *Growth and characterizations of spectrally selective Cr2O3/Cr/Cr2O3 multilayer solar absorber by e-beam evaporation.* Alloys and Compounds, 734(2018) 204-209.

[50] Herrera-Zamora, D., F. Lizama-Tzec, I. Santos-González, R. Rodríguez-Carvajal, O. García-Valladares, O. Arés-Muzio, and G. Oskam, *Electrodeposited black cobalt selective coatings for application in solar thermal collectors: Fabrication, characterization, and stability.* Solar Energy, 207(2020) 1132-1145.

[51] Xiao, X., L. Miao, G. Xu, L. Lu, Z. Su, N. Wang, and S. Tanemura, *A facile process to prepare copper oxide thin films as solar selective absorbers.* Applied Surface Science, 257(2011) 10729-10736.

[52] Karthick Kumar, S., S. Suresh, S. Murugesan, and S.P. Raj, *CuO thin films made of nanofibers for solar selective absorber applications.* Solar Energy, 94(2013) 299-304.

[53] Siddiqui, H., M.S. Qureshi, and F.Z. Haque, *Valuation of copper oxide (CuO) nanoflakes for its suitability as an absorbing material in solar cells fabrication.* Optik, 127(2016) 3713-3717.

[54] Cheng, B., K.K. Wang, K.P. Wang, M. Li, W. Jiang, B.J. Cong, C.L. Song, S.H. Jia, G.R. Han, and Y. Liu, *Preparation and characterization of porous carbon–titania nanocomposite films as solar selective absorbers.* Journal of Alloys and Compounds, 635(2015) 129-135.

[55] Amri, A., Z.T. Jiang, T. Pryor, C.-Y. Yin, and S. Djordjevic, *Developments in the synthesis of flat plate solar selective absorber materials via sol–gel methods: A review.* Renewable and Sustainable Energy Reviews, 36(2014) 316-328.

[56] Shehayeb, S., X. Deschanels, I. Karamé, L. Ghannam, and G. Toquer, *Spectrally selective coatings obtained from electrophoretic deposition of CuO nanoparticles.* Surface and Coatings Technology, 322(2017) 38-45.

[57] Dolai, S., R. Dey, S. Das, S. Hussain, R. Bhar, and A. Pal, *Cupric oxide (CuO) thin films prepared by reactive dc magnetron sputtering technique for photovoltaic application.* Journal of Alloys and Compounds, 724(2017) 456-464.

[58] Marques, L., S. Braz, and E. Fernandes, *High emissivity ZnO coatings prepared from chloride electrolyte by electrodeposition on a "Dynamic Hydrogen Bubble Template".* Infrared Physics & Technology, 113(2021) 103614.

[59] Prasad, M.S., V.V. Dutt, K.P. Kumar, S. Atchuta, V. Anbazhagan, and S. Sakthivel, *A functional Ag-TiO2 nanocomposites solar selective absorber with antimicrobial activities by photochemical-reduction process.* Photochemistry and Photobiology B: Biology, 199(2019) 111626.

[60] Salvi, S.S., V. Bhalla, R.A. Taylor, V. Khullar, T.P. Otanicar, P.E. Phelan, and H. Tyagi, *Technological advances to maximize solar collector energy output:* Electronic Packaging, 140(2018)040802.

[61] Cao, F., K. McEnaney, G. Chen, and Z. Ren, *A review of cermet-based spectrally selective solar absorbers.* Energy & Environmental Science, 7(2014) 1615-1627.

[62] Boldoo, T., J. Ham, E. Kim, and H. Cho, *Review of the Photothermal Energy Conversion Performance of Nanofluids, Their Applications, and Recent Advances.* Energies, 13(2020) 5748.

[63] Burschka, J., N. Pellet, S.-J. Moon, R. Humphry-Baker, P. Gao, M.K. Nazeeruddin, and M. Grätzel, *Sequential deposition as a route to high-performance perovskite-sensitized solar cells.* Nature, 499(2013) 316.

[64] Elliott, D.A., N. Nabavizadeh, S.K. Seung, E.K. Hansen, and J.M. Holland, *Radiation Therapy.* 268(2018) 268-290.

[65] Dan, A., H.C. Barshilia, K. Chattopadhyay, and B. Basu, *Solar energy absorption mediated by surface plasma polaritons in spectrally selective dielectric-metal-dielectric coatings: a critical review.* Renewable and Sustainable Energy Reviews, 79(2017) 1050-1077.

[66] Kim, J.U., S. Lee, S.J. Kang, and T.-i. Kim, *Materials and design of nanostructured broadband light absorbers for advanced light-to-heat conversion.* Nanoscale, 10(2018) 21555-21574.

[67] Dan, A. and B. Basu, *Understanding spectrally selective properties of solar absorbers*, in *Energy Saving Coating Materials*, Elsevier, 2020, 133-151.

[68] Liu, B., C. Wang, S. Bazri, I.A. Badruddin, Y. Orooji, S. Saeidi, S. Wongwises, and O. Mahian, *Optical property and thermal stabilities evaluation of solar absorber enhanced by nanostructure selective coatings.* Powder Technology, 2020.

[69] Atchuta, S., S. Sakthivel, and H.C. Barshilia, *Nickel doped cobaltites spinel solar selective absorber coatings for efficient photothermal conversions with a low thermal radiative losses at high temperatures.* Solar Energy Materials and Solar Cells, 200(2019)109917.

[70] Dan, A., A. Biswas, P. Sarkar, S. Kashyap, K. Chattopadhyay, H.C. Barshilia, and B. Basu, *Enhancing spectrally selective response of W/WAlN/WAlON/Al2O3 Based nanostructure multilayered absorber coatings through graded optical constant.* Solar Energy Materials and Solar Cells, 176(2018)157-166.

[71] Atkinson, C., C.L. Sansom, H.J. Almond, and C.P. Shaw, *Coatings for concentrating solar systems – A review.* Renewable and Sustainable Energy Reviews, 45(2015) 113-122.

[72] Gao, M., L. Zhu, C.K. Peh, and G.W. Ho, *Solar absorber material and system designs for photothermal water vaporization towards clean water and energy production.* Energy & Environmental Science, 12(2019) 841-864.

[73] Irshad, M.S., N. Arshad, and X. Wang, *Nanoenabled photothermal materials for clean water production.* Global Challenges, 5(2021) 2000055.

[74] Liu, X.-S., *Inorganic photochemical synthesis*, in *Modern Inorganic Synthetic Chemistry*. Elsevier 2017, 143-165.

[75] Wang, X., X. Wu, L. Yuan, C. Zhou, Y. Wang, K. Huang, and S. Feng, *Solar selective absorbers with foamed nanostructure prepared by hydrothermal method on stainless steel.* Solar Energy Materials and Solar Cells, 146(2016) 99-106.

[76] Nunes, R.A.X., V.C. Costa, W. Sade, F.R. Araújo, and G.M. Silva, *Selective Surfaces of Black Chromium for Use in Solar Absorbers.* Materials Research, 21(2017).

[77] Shimizu, M., M. Suzuki, F. Iguchi, and H. Yugami, *High-temperature Solar Selective Absorbers Using Transparent Conductive Oxide Coated Metal.* Energy Procedia, 57(2014) 418-426.

[78] Chen, J., C. Guo, J. Chen, J. He, Y. Ren, and L. Hu, *Microstructure, optical and electrical properties of CrAlN film as a novel material for high temperature solar selective absorber applications.* Materials Letters, 133(2014) 71-74.

[79] Tabor, H., *Selective radiation. i. wavelength discrimination. ii. wavefront discrimination.* Bull. Res. Counc. Isr., Sect. C, 5(1956).

[80] Shaffer, L., *Wavelength-dependent (selective) processes for the utilization of solar energy.* Solar Energy, 2(1958) 21-26.

[81] Agnihotri, O. and B.K. Gupta, *Solar selective surfaces.* wi, 1981.

[82] Randich, E. and D. Allred, *Chemically vapor-deposited ZrB2 as a selective solar absorber.* Thin Solid Films, 83(1981) 393-398.

[83] Ehrenreich, H. and B. Seraphin, *Symposium on the Fundamental Optical Properties of Solids Relevant to Solar Energy Conversion.* STIN, 77(1975) 12538.

[84] González, F., E. Barrera-Calva, L. Huerta, and R.S. Mane, *Coatings of Fe3O4 nanoparticles as selective solar absorber.* The Open Surface Science Journal, 3(2011).

[85] Zhang, K., L. Hao, M. Du, J. Mi, J.-N. Wang, and J.-p. Meng, *A review on thermal stability and high temperature induced ageing mechanisms of solar absorber coatings.* Renewable and Sustainable Energy Reviews, 67(2017) 1282-1299.

[86] Agnihotri, O. and B.K. Gupta, *Solar selective surfaces.* New York, 1981.

[87] Pellegrini, G., *Experimental methods for the preparation of selectively absorbing textured surfaces for photothermal solar conversion.* Solar Energy Materials, 3(1980) 391-404.

[88] Soum-Glaude, A., A. Le Gal, M. Bichotte, C. Escape, and L. Dubost, *Optical characterization of TiAlNx/TiAlNy/Al2O3 tandem solar selective absorber coatings.* Solar Energy Materials and Solar Cells, 170(2017) 254-262.

[89] Zou, C., L. Huang, J. Wang, and S. Xue, *Effects of antireflection layers on the optical and thermal stability properties of a spectrally selective CrAlN–CrAlON based tandem absorber.* Solar Energy Materials and Solar Cells, 137(2015) 243-252.

[90] Gong, D., H. Liu, G. Luo, P. Zhang, X. Cheng, B. Yang, Y. Wang, J. Min, W. Wang, and S. Chen, *Thermal aging test of AlCrNO-based solar selective absorbing coatings prepared by cathodic arc plating.* Solar Energy Materials and Solar Cells, 136(2015) 167-171.

[91] Barrera-Calva, E., J. Mendez-Vivar, M. Ortega-Lopez, L. Huerta-Arcos, J. Morales-Corona, and R. Olayo-Gonzalez, *Silica-CuO composites as solar selective coating prepared by dipping sol-gel.* Materials Science, 2008(2008)

[92] González-Roubaud, E., D. Pérez-Osorio, and C. Prieto, *Review of commercial thermal energy storage in concentrated solar power plants: Steam vs. molten salts.* Renewable and sustainable energy reviews, 80(2017) 133-148.

[93] Li, C.-J., P. Li, K. Wang, and E.E. Molina, *Survey of property of key single and mixture halide salts for potential applications as high temperature heat transfer fluid for concentrated solar thermal power system.* AIMS Energy, 2(2014)133-157.

[94] Pitz-Paal, R., A. Amin, M. Oliver Bettzuge, P. Eames, G. Flamant, F. Fabrizi, J. Holmes, A. Kribus, H. van der Laan, and C. Lopez, *a review of development issues and potentials to 2050.* Solar energy engineering, 134(2012).

[95] Hang, Q., Z. Jun, Y. Xiao, and C. Junkui, *Prospect of concentrating solar power in China—the sustainable future.* Renewable and sustainable energy reviews, 12(2008) 2505-2514.

[96] Trieb, F. and H. Müller-Steinhagen, *Concentrating solar power for seawater desalination in the Middle East and North Africa.* Desalination, 220(2008) 165-183.

[97] Abbas, M., B. Boumeddane, N. Said, and A. Chikouche, *A 100 MW solar power plant using hydrogen for Algeria.* International journal of hydrogen energy, 36(2011) 4305-4314.

[98] Weinstein, L.A., J. Loomis, B. Bhatia, D.M. Bierman, E.N. Wang, and G. Chen, *Concentrating Solar Power.* Chem Rev, 115(2015) 12797-838.

[99] Rebouta, L., P. Capela, M. Andritschky, A. Matilainen, P. Santilli, K. Pischow, and E. Alves, *Characterizations of TiAlSiN/TiAlSiON/SiO2 optical stacks designed by modelling calculations for solar selective application.* Solar energy materials and solar cells, 105(2012)202-207.

[100] Liu, H., F. Ren, Q. Li, X. Cheng, T. Fu, M. Duan, Q. Wan, Y. Chen, D. Fu, , and B. Yang, *Structure and thermal stabilities of spectrally selective absorbers based on AlCrON coatings for solar to thermal conversion application.* Solar Energy Materials and Solar Cells, 157(2016) 108-116.

[101] Selvakumar, N., N. Manikandanath, A. Biswas, and H.C. Barshilia, *Design and fabrication of thermally stable HfMoN/HfON/Al2O3 tandem absorber for solar thermal power generation application.* Solar energy materials and solar cells, 102(2012)86-92.

[102] Valleti, K., D.M. Krishna, and S. Joshi, *Functional multi-layer nitride coatings for high temperature solar selective applications.* Solar energy materials and solar cells, 121(2014) 14-21.

[103] Tsai, T., S. Hsueh, and J. Fang, *Optical Properties of Al x O y/Ni/Al x O y Multilayered Absorber Coatings Prepared by Reactive DC Magnetron Sputtering.* Journal of electronic materials, 43(2014) 229-235.

[104] Maaza, M., B. Ngom, Z. Nuru, and S. Khamlich, *Surface-Interface Investigation and Stability of Cermet-Based Solar Absorbers by Grazing Angle X-Rays Reflectometry: Pt–Al 2 O 3 Case.* Arabian Journal for Science and Engineering, 39(2014) 5825-5846.

[105] Zhou, E., K. Xu, and C. Wang, *Analysis of the Cost and Value of Concentrating Solar Power in China.* 2019.

[106] Sergeant, N.P., M. Agrawal, and P. Peumans, *High performance solar-selective absorbers using coated sub-wavelength gratings.* Optics express, 18(2010) 5525-5540.

[107] Teles, M.d.P.R., K.A. Ismail, and A. Arabkoohsar, *A new version of a low concentration evacuated tube solar collector: Optical and thermal investigation.* Solar Energy, 180(2019) 324-339.

[108] Psomopoulos, C., *Solar energy: Harvesting the sun's energy for a sustainable future.* Solar Energy, 117(2013) 2.

[109] Tian, Y. and C.-Y. Zhao, *A review of solar collectors and thermal energy storage in solar thermal applications.* Applied energy, 104(2013) 538-553.

[110] Kalogirou, S.A., S. Karellas, K. Braimakis, C. Stanciu, and V. Badescu, *Exergy analysis of solar thermal collectors and processes.* Progress in Energy and Combustion Science, 56(2016) 106-137.

[111] Evangelisti, L., R.D.L. Vollaro, and F. Asdrubali, *Latest advances on solar thermal collectors: A comprehensive review.* Renewable and Sustainable Energy Reviews, 114(2019) 109318.

[112] Ravi Kumar, K., N. Krishna Chaitanya, and N. Sendhil Kumar, *Solar thermal energy technologies and its applications for process heating and power generation–A review.* 2021.

[113] Selvakumar, N. and H.C. Barshilia, *Review of physical vapor deposited (PVD) spectrally selective coatings for mid-and high-temperature solar thermal applications.* Solar energy materials and solar cells, 98(2012)1-23.

[114] Hafez, A., A. Attia, H. Eltwab, A. ElKousy, A. Afifi, A. AbdElhamid, A. AbdElqader, S.K. Fateen, K. El-Metwally, and A. Soliman, *Design analysis of solar parabolic trough thermal collectors.* Renewable and Sustainable Energy Reviews, 82(2018) 1215-1260.

[115] Abdulhamed, A.J., N.M. Adam, M.Z.A. Ab-Kadir, and A.A. Hairuddin, *Review of solar parabolic-trough collector geometrical and thermal analyses, performance, and applications.* Renewable and Sustainable Energy Reviews, 91(2018) 822-831.

[116] Ummadisingu, A. and M. Soni, *Concentrating solar power–technology, potential and policy in India.* Renewable and sustainable energy reviews, 15(2011) 5169-5175.

[117] Atchuta, S., S. Sakthivel, and H.C. Barshilia, *Selective properties of high-temperature stable spinel absorber coatings for concentrated solar thermal application.* Solar Energy, 199(2020) 453-459.

[118] Tian, Y., X. Liu, A. Ghanekar, and Y. Zheng, *Scalable-manufactured metal–insulator–metal based selective solar absorbers with excellent high-temperature insensitivity.* Applied Energy, 281(2021)116055.

[119] Ozgen, F., M. Esen, and H. Esen, *Experimental investigation of thermal performance of a double-flow solar air heater having aluminium cans.* Renewable Energy, 34(2009) 2391-2398

[120] Li, P., B. Liu, Y. Ni, K.K. Liew, J. Sze, S. Chen, and S. Shen, *Large-Scale Nanophotonic Solar Selective Absorbers for High-Efficiency Solar Thermal Energy Conversion.* Adv Mater, 27(2015) 4585-91.

[121] Li, P., B. Liu, Y. Ni, K.K. Liew, J. Sze, S. Chen, and S. Shen, *Large-Scale Nanophotonic Solar Selective Absorbers for High-Efficiency Solar Thermal Energy Conversion.* Advanced Materials, 27(2015) 4585-4591.

[122] Kim, C.C., J.W. Garland, H. Abad, and P.M. Raccah, *Modeling the optical dielectric function of semiconductors: extension of the critical-point parabolic-band approximation.* Physical Review B, 45(1992) 11749.

[123] Nohava, J., P. Dessarzin, P. Karvankova, and M. Morstein, *Characterization of tribological behavior and wear mechanisms of novel oxynitride PVD coatings designed for applications at high temperatures.* Tribology International, 81(2015) 231-239.

[124] West, A., *'Solid State Chemistry'John willey & Sons*, 2003

[125] Chen, Z., X. Zhao, and Y. Tang, *"Thin Films for Energy Harvesting, Conversion, and Storage"*. 2019, Multidisciplinary Digital Publishing Institute. 2010, 608.

[126] Ding, T., X. Yang, L. Bai, Y. Zhao, K.E. Fong, N. Wang, H.V. Demir, and X.W. Sun, *Colloidal quantum-dot LEDs with a solution-processed copper oxide (CuO) hole injection layer.* Organic Electronics, 26(2015) 245-250.

[127] Frey, H. and H.R. Khan, *Handbook of thin film technology*, springer, 2015.

[128] Granqvist, C.G., *Preparation of thin films and nanostructured coatings for clean tech applications: A primer.* Solar Energy Materials and Solar Cells, 99(2012) 166-175.

[129] Seshan, K., *Handbook of Thin Film Deposition Techniques Principles, Methods, Equipment and Applications, Second Editon*. CRC press, 2002.

[130] Kern, W. and K.K. Schuegraf, *Deposition technologies and applications: Introduction and overview*, in *Handbook of Thin Film Deposition Processes and Techniques*. Elsever, 2001, 11-43.

[131] Rossnagel, S., *Thin film deposition with physical vapor deposition and related technologies.* Journal of Vacuum Science & Technology A: Vacuum, Surfaces, and Films, 21(2003) 574-587.

[132] Cao, F., D. Kraemer, L. Tang, Y. Li, A.P. Litvinchuk, J. Bao, G. Chen, and Z. Ren, *A high-performance spectrally-selective solar absorber based on a yttria-stabilized zirconia cermet with high-temperature stability.* Energy & Environmental Science, 8(2015) 3040-3048.

[133] Teixeira, V., E. Sousa, M. Costa, C. Nunes, L. Rosa, M. Carvalho, M. Collares-Pereira, E. Roman, and J. Gago, *Spectrally selective composite coatings of Cr–Cr2O3 and Mo–Al2O3 for solar energy applications.* Thin solid films, 392(2001) 320-326.

[134] Zhang, Q.-C. and Y. Shen, *High performance W–AlN cermet solar coatings designed by modelling calculations and deposited by DC magnetron sputtering.* Solar Energy Materials and Solar Cells, 81(2004) 25-37.

[135] Kumar, S.K., S. Murugesan, S. Suresh, and S.P. Raj, *Nanostructured CuO thin films prepared through sputtering for solar selective absorbers.* J. Sol. Energy, 2013(2013) 147270.

[136] Bernal, M. and J. Ustarroz, *Electrodeposition of nanostructured catalysts for electrochemical energy conversion: current trends and innovative strategies.* Current Opinion in Electrochemistry, 2021, 100688.

[137] Ojo, A.A. and I.M. Dharmadasa, *Electroplating of semiconductor materials for applications in large area electronics: A review.* Coatings, 8(2018) 262.

[138] Zhang, Q., K. Zhang, D. Xu, G. Yang, H. Huang, F. Nie, C. Liu, and S. Yang, *CuO nanostructures: synthesis, characterization, growth mechanisms, fundamental properties, and applications.* Progress in Materials Science, 60(2014) 208-337.

[139] Ebenezar, J., *Recent trends in materials science and applications*. Vol. 189. 2017: Springer.

[140] Vangari, M., T. Pryor, and L. Jiang, *Supercapacitors: review of materials and fabrication methods.* Journal of Energy Engineering, 139(2013) 72-79.

[141] Sagadevan, S., J. Podder, and I. Das, *Recent trends in materials science and applications-Nanomaterials, Crystal Growth, Thin films.* Quantum Dots, & Spectroscopy (Proceedings ICRTMSA 2016), 189(2017) 145-152.

[142] Lu, C., L. Qi, J. Yang, D. Zhang, N. Wu, and J. Ma, *Simple template-free solution route for the controlled synthesis of Cu (OH) 2 and CuO nanostructures.* The Journal of Physical Chemistry B, 108(2004) 17825-17831.

[143] Currier, J.M., J.M. Holland, K. Drescher, and D. Foy, *Initial psychometric evaluation of the Moral Injury Questionnaire—Military version.* Clinical psychology & psychotherapy, 22(2015) 54-63.

[144] Karami, H. and B. Afshari, *Square Pulse Galvanostatic Synthesis and Characterization of Nano-Copper Oxide.* Int. J. Electrochem. Sci, 12(2017) 1492-1505.

[145] Zhang, J.X. and K. Hoshino, *Fundamentals of nano/microfabrication and scale effect.* Molecular Sensors and Nanodevices; Zhang, JXJ, Hoshino, K., Eds, 2019, 43-111.

[146] Kerdcharoen, T. and C. Wongchoosuk, *Carbon nanotube and metal oxide hybrid materials for gas sensing*, in *Semiconductor Gas Sensors*. Elsevier, 2013, 386-407.

[147] Nwambaekwe, K.C., V. John-Denk, S.F. Douman, P. Mathumba, S.T. Yussuf, O.V. Uhuo, P.I. Ekwere, and E.I. Iwuoha, *Crystal engineering and thin film deposition strategy towards improving the performance of kesterite photovoltaic cells.* Materials Research and Technology, 2021.

[148] Eskandari, A., P. Sangpour, and M. Vaezi, *Hydrophilic Cu2O nanostructured thin films prepared by facile spin coating method: investigation of surface energy and roughness.* Materials Chemistry and Physics, 147(2014) 1204-1209.

[149] He, G. and K. Wang, *The super hydrophobicity of ZnO nanorods fabricated by electrochemical deposition method.* Applied Surface Science, 257(2011) 6590-6594.

[150] Tran, T.H. and V.T. Nguyen, *Copper Oxide Nanomaterials Prepared by Solution Methods, Some Properties, and Potential Applications: A Brief Review.* Int Sch Res Notices, 2014(2014) 856592.

[151] Prasanth, D., K.P. Sibin, and H.C. Barshilia, *Optical properties of sputter deposited nanocrystalline copper oxide thin films.* Thin Solid Films, 673(2019) 78-85.

[152] Mabrouki, M., *Effect of annealing temperature on the structural, physical, chemical, and wetting properties of copper oxide thin films.* Materials Today: Proceedings, 13(2019) 771-776.

[153] Sangwaranatee, N., M. Horprathum, C. Chananonnawathorn, and Hendro, *Effect of annealing treatment on sputtered copper oxide thin film.* Materials Today: Proceedings, 5(2018) 15170-15173.

[154] Ghidan, A.Y., T.M. Al-Antary, and A.M. Awwad, *Green synthesis of CuO nanoparticles using Punica granatum peels extract: Effect on green peach Aphid.* Environmental Nanotechnology,6(2016) 95-98.

[155] Du, Y., X. Gao, and X. Meng, *Preparation and characterization of single-phased n-type CuO film by DC magnetron sputtering.* Physica B: Condensed Matter, 560(2019) 37-40.

[156] Krishnamoorthy, K. and S.-J. Kim, *Growth, characterization and electrochemical property of hierarchical CuO nanostructures for supercapacitor applications.* Materials Research Bulletin, 48(2013) 3136-3139.

[157] Wu, D., Q. Zhang, and M. Tao, *LSDA+ U study of cupric oxide: Electronic structure and native point defects.* Physical Review B, 73(2006) 235206.

[158] Khan, M.M., S.F. Adil, and A. Al-Mayouf, *Metal oxides as photocatalysts.* 2015, Elsevier.

[159] Hong, J., J. Li, and Y. Ni, *Urchin-like CuO microspheres: Synthesis, characterization, and properties.* Journal of alloys and compounds, 481(2009) 610-615.

[160] Dar, M.A., S.H. Nam, Y.S. Kim, and W.B. Kim, *Synthesis, characterization, and electrochemical properties of self-assembled leaf-like CuO nanostructures.* Journal of Solid State Electrochemistry, 14(2010) 1719-1726.

[161] Chen, J., F. Zhang, J. Wang, G. Zhang, B. Miao, X. Fan, D. Yan, and P. Yan, *CuO nanowires synthesized by thermal oxidation route.* Journal of Alloys and Compounds, 454(2008) 268-273.

[162] Li, Y., J. Liang, Z. Tao, and J. Chen, *CuO particles and plates: synthesis and gas-sensor application.* Materials Research Bulletin, 43(2008) 2380-2385.

[163] Yao, W.-T., S.-H. Yu, Y. Zhou, J. Jiang, Q.-S. Wu, L. Zhang, and J. Jiang, *Formation of uniform CuO nanorod structures by spontaneous aggregations: Selective synthesis of CuO, Cu2O, and Cu nanopartcles by solid−liquid phase arc discharge process.* Physical Chemistry B, 109(2005) 14011-14016.

[164] Zhang, Y., S.W. Or, X. Wang, T. Cui, W. Cui, Y. Zhang, and Z. Zhang, *Hydrothermal Synthesis of Three-Dimensional Hierarchical CuO Butterfly-Like Architectures.* European journal of inorganic chemistry, 2009(2009) 168-173.

[165] Jiang, Z., Q. Niu, and W. Deng, *Hydrothermal synthesis of CuO nanostructures with novel shapes.* Nanoscience, 12(2007) 40-44.

[166] Zhang, H., S. Li, X. Ma, and D. Yang, *Controllable growth of dendrite-like CuO nanostructures by ethylene glycol assisted hydrothermal process.* Materials Research Bulletin, 43(2008) 1291-1296.

[167] Dar, M., Q. Ahsanulhaq, Y. Kim, J. Sohn, W. Kim, and H. Shin, *Versatile synthesis of rectangular shaped nanobat copper oxide nanostructure by hydrothermal methods; structural property and growth mechanism.* Applied Surface Science, 255(2009) 6279-6284.

[168] Abaker, M., A. Umar, S. Baskoutas, S. Kim, and S. Hwang, *Structural and optical properties of CuO layered hexagonal synthesised by low-temperature hydrothermal processes.* Applied Physics, 44(2011) 155405.

[169] Xia, J., H. Li, Z. Luo, K. Wang, S. Yin, and Y. Yan, *Ionic liquid-assisted hydrothermal synthesis of three-dimensional hierarchical CuO peachstone-like architectures.* Applied surface science, 256(2010) 1871-1877.

[170] Liu, J., J. Jin, Z. Deng, S.-Z. Huang, Z.-Y. Hu, L. Wang, C. Wang, L.-H. Chen, Y. Li, and G. Van Tendeloo, *Tailoring CuO nanostructure for enhanced photocatalytic properties.* Colloid and interface science, 384(2012)1-9.

[171] Pan, Q., K. Huang, S. Ni, F. Yang, S. Lin, and D. He, *Synthesis of sheaf-like CuO from aqueous solution and their application in lithium-ion batteries.* Journal of Alloys and Compounds, 484(2009) 322-326.

[172] Jeong, D., J. Lee, H. Hong, D. Choi, J.-W. Cho, S.-K. Kim, and Y. Nam, *Absorption mechanism and performance characterization of CuO nanostructured absorbers.* Solar Energy Materials and Solar Cells, 169(2017) 270-279.

[173] Bhattacharjee, A. and M. Ahmaruzzaman, *CuO nanostructures: facile synthesis and application for enhanced photodegradation of organic compounds and reduction of p-nitrophenol from aqueous phase.* RSC Advances, 6(2016) 41348-41363.

[174] Liu, J., X. Huang, Y. Li, K. Sulieman, X. He, and F. Sun, *Hierarchical nanostructures of cupric oxide on a copper substrate: controllable morphology and wettability.* Journal of Materials Chemistry, 16(2006) 4427-4434.

[175] Liu, X., Z. Li, Q. Zhang, F. Li, and T. Kong, *CuO nanowires prepared via a facile solution route and their photocatalytic property.* Materials Letters, 72(2012) 49-52.

[176] Liao, L., Z. Zhang, B. Yan, Z. Zheng, Q. Bao, T. Wu, C.M. Li, Z. Shen, J. Zhang, and H. Gong, *Multifunctional CuO nanowire devices: p-type field effect transistors and CO gas sensors.* Nanotechnology, 20(2009) 085203.

[177] Ethiraj, A.S. and D.J. Kang, *Synthesis and characterization of CuO nanowires by a simple wet chemical method.* Nanoscale research letters, 7(2012) 70.

[178] Dupas, C. and M. Lahmani, *Nanoscience: Nanotechnologies and nanophysics*. springer, 2007.

[179] Salari, M., M. Rezaee, S. Marashi, and S. Aboutalebi, *The role of the diluent phase in the mechanochemical preparation of TiO2 nanoparticles.* Powder technology, 192(2009) 54-57.

[180] Yadav, T., R. Yadav, and D. Singh, *Mechanical milling: A top down approach for the synthesis of nanomaterials and nanocomposites. Nanosci Nanotechnol 2 (2022): 22–48*.

[181] Jeevanandam, J., Y.S. Chan, and M.K. Danquah, *Biosynthesis of metal and metal oxide nanoparticles.* ChemBioEng Reviews, 3(2016) 55-67.

[182] Jana, R., A. Dey, M. Das, J. Datta, P. Das, and P.P. Ray, *Improving performance of device made up of CuO nanoparticles synthesized by hydrothermal over the reflux method.* Applied Surface Science, 452(2018) 155-164.

[183] Shi, Y., *Hot wire chemical vapor deposition(CVD) chemistry in the gas phases and on the catalyst surfaces with organosilicon compounds.* chemical research, 48(2015) 163-173.

[184] Safarifard, V. and A. Morsali, *Sonochemical syntheses of a new fibrous-like nano-scale manganese (II) coordination supramolecular compounds; fabrication of octahedral-like Mn3O4 nano-structure.* Ultrasonics sonochemistry, 21(2014) 253-261.

[185] Ameri, B., S.S.H. Davarani, R. Roshani, H.R. Moazami, and A. Tadjarodi, *A flexible mechanochemical route for the synthesis of CuO nanorods/ nanowires for supercapacitor application: the effect of morphologies on the charge storage ability.* Alloys and Compounds, 695(2017) 114-123.

[186] Liu, Q., H. Liu, Y. Liang, Z. Xu, and G. Yin, *Large-scale synthesis of single-crystalline CuO nanoplatelets by a hydrothermal process.* Materials research bulletin, 41(2006) 697-702.

[187] Guan, X., L. Li, G. Li, Z. Fu, J. Zheng, and T. Yan, *Hierarchical CuO hollow microspheres: Controlled synthesis for enhanced lithium storage performance.* Alloys and Compounds, 509(2011) 3367-3374.

[188] Wang, S., C. Hsiao, S.-J. Chang, K. Lam, K. Wen, S. Hung, S. Young, and B. Huang, *A CuO nanowire infrared photodetector.* Sensors and Actuators A: Physical, 171(2011) 207-211.

[189] Hu, Y., X. Huang, K. Wang, J. Liu, J. Jiang, R. Ding, X. Ji, and X. Li, *Kirkendall-effect-based growth of dendrite-shaped CuO hollow micro/nanostructures for lithium-ion battery anodes.* Journal of Solid State Chemistry, 183(2010) 662-667.

[190] Zhao, Y., J. Zhao, Y. Li, D. Ma, S. Hou, L. Li, X. Hao, and Z. Wang, *Room temperature synthesis of 2D CuO nanoleaves in aqueous solution.* Nanotechnology, 22(2011) 115604.

[191] Tsai, C.-M., G.-D. Chen, T.-C. Tseng, C.-Y. Lee, C.-T. Huang, W.-Y. Tsai, W.-C. Yang, M.-S. Yeh, and T.-R. Yew, *CuO nanowire synthesis catalyzed by a CoWP nanofilter.* Acta materialia, 57(2009) 1570-1576.

[192] Zhu, G., H. Xu, Y. Xiao, Y. Liu, A. Yuan, and X. Shen, *Facile fabrication and enhanced sensing properties of hierarchically porous CuO architectures.* ACS applied materials & interfaces, 4(2012) 744-751.

[193] Sahay, R., J. Sundaramurthy, P.S. Kumar, V. Thavasi, S.G. Mhaisalkar, and S. Ramakrishna, *Synthesis and characterization of copper oxide nanofibers, and investigations for its suitabilities as blocking layer in ZnO NPs based dye sensitized solar cell and as photocatalysts in organic dye degradation.* Solid State Chemistry, 186(2012) 261-267.

[194] Anandan, S., X. Wen, and S. Yang, *Room temperature growth of CuO nanorod arrays on copper and their application as a cathode in dye-sensitized solar cells.* Materials Chemistry and Physics, 93(2005) 35-40.

[195] Feng, Y. and X. Zheng, *Plasma-enhanced catalytic CuO nanowires for CO oxidation.* Nano letters, 10(2010) 4762-4766.

[196] Wang, L., Q. Zhou, G. Zhang, Y. Liang, B. Wang, W. Zhang, B. Lei, and W. Wang, *A facile room temperature solution-phase route to synthesize CuO nanowires with enhanced photocatalytic performance.* Materials Letters, 74(2012) 217-219.

[197] Zhu, Y., A. Moo, T. Yu, X. Xu, X. Gao, Y. Liu, C. Lim, Z. Shen, C. Ong, and A. Wee, *Enhanced field emission from O2 and CF4 plasma-treated CuO nanowires.* Chemical physics letters, 416(2006) 458-463.

[198] Liu, J., X. Huang, Y. Li, Z. Li, Q. Chi, and G. Li, *Formation of hierarchical CuO microcabbages as stable bionic superhydrophobic materials via a room-temperature solution-immersion process.* Solid State Sciences, 10(2008) 1568-1576.

[199] Rejith, S. and C. Krishnan, *Optical, thermal and magnetic studies on zinc-doped copper oxide nanoparticles.* Materials Letters, 106(2013) 87-89.

[200] Yang, X.-D., L.-L. Jiang, C.-J. Mao, H.-L. Niu, J.-M. Song, and S.-Y. Zhang, *Sonochemical synthesis and nonlinear optical property of CuO hierarchical superstructures.* Materials Letters, 115(2014) 121-124.

[201] Liu, J., X. Huang, Y. Li, K.M. Sulieman, X. He, and F. Sun, *Hierarchical nanostructures of cupric oxide on a Cu substrates: controllable morphologies and wettabilities.* Materials Chemistry, 16(2006) 4427.

[202] Yin, R., T. Agrawal, U. Khan, G.K. Gupta, V. Rai, Y.-Y. Huang, and M.R. Hamblin, *Antimicrobial photodynamic inactivations in nanomedicine:* Nanomedicine, 10(2015) 2379-2404.

[203] Vaidehi, D., V. Bhuvaneshwari, D. Bharathi, and B.P. Sheetal, *Antibacterial and photocatalytic activities of CuO NPs synthesized using Solanumlycopersicum leaf extracts.* Materials Research, 5(2018) 85403.

[204] Diamond, D.M., A.M. Campbell, C.R. Park, J. Halonen, and P.R. Zoladz, *synthesis on the neurobiological basis of stressinduced amnesia, flashbulb and traumatic memories, and the Yerkes-Dodson law.* Neural plasticity, 2007(2007).

[205] Sivaraj, R., P.K. Rahman, P. Rajiv, H.A. Salam, and R. Venckatesh, *Biogenic copper oxide NPs synthesis using Tabernaemontanadivaricate leaf extracts and its antibacterial activities against urinary tract pathogen.* Spectrochimica Acta Part A, 178(2014) 178-181.

[206] Bordbar, M., Z. Sharifi-Zarchi, and B. Khodadadi, *Green synthesis of copper oxide nanoparticles/ clinoptilolite using Rheumpalmatum L. root extracts: high catalytic activity for reduction of 4-nitro phenol, rhodamine B, and methylene blue.*Sol-Gel Science and Technology, 81(2017) 724-733.

[207] Vickers, N.J., *Animal communication: when i'm calling you, will you answer too?* Current biology, 27(2017) R713-R715.

[208] Praburaman, L., J.-S. Jang, G. Muthusamy, S. Arumugam, K. Manoharan, K.-M. Cho, C. Min, S. Kamala-Kannan, and O. Byung-Taek, *Piper betle-mediated synthesis, characterizationantibacterial and rat splenocyte cytotoxic effects of copper oxide nanoparticles.* Artificial cells, nanomedicine, and biotechnology, 44(2016) 1400-1405.

[209] Mittal, A.K., Y. Chisti, and U.C. Banerjee, *Synthesis of metallic nanoparticles using plant extracts.* Biotechnology advances, 31(2013) 346-356.

[210] Åsbrink, S. and L.-J. Norrby, *A refinement of the crystal structure of copper (II) oxide with a discussion of some exceptional esd's.* Acta Crystallographica Section B: Structural Crystallography and Crystal Chemistry, 26(1970) 8-15.

[211] Keriti, Y., R. Brahimi, Y. Gabes, S. Kaci, and M. Trari, *Physical and photo-electrochemical properties of CuO thin film grown on µc-Si: H/glass. Application to solar energy conversion.* Solar Energy, 206(2020) 787-792.

[212] Moura, A.P., L.S. Cavalcante, J.C. Sczancoski, D.G. Stroppa, E.C. Paris, A.J. Ramirez, J.A. Varela, and E. Longo, *Structure and growth mechanism of CuO plates obtained by microwave-hydrothermal without surfactants.* Advanced Powder Technology, 21(2010) 197-202.

[213] Hong, N.H., *Introduction to nanomaterials: basic properties, synthesis, and characterization*, in *Nano-Sized Multifunctional Materials*. Elsevier 2019, 1-19.

[214] Rehman, S., A. Mumtaz, and S. Hasanain, *Size effects on the magnetic and optical properties of CuO nanoparticles.* Journal of Nanoparticle Research, 13(2011) 2497-2507.

[215] Yang, M. and J. He, *Fine tuning of the morphology of copper oxide nanostructures and their application in ambient degradation of methylene blue.* Journal of colloid and interface science, 355(2011) 15-22.

[216] Al-Gaashani, R., S. Radiman, N. Tabet, and A.R. Daud, *Synthesis and optical properties of CuO nanostructures obtained via a novel thermal decomposition method.* Journal of Alloys and Compounds, 509(2011) 8761-8769.

[217] Jin, C., K. Baek, S. Park, H.W. Kim, W.I. Lee, and C. Lee, *Influence of SnO2 coating and thermal annealing on the structure and luminescence properties of CuO nanorods.* Solid state communications, 150(2010) 1812-1817.

[218] Aslani, A. and V. Oroojpour, *CO gas sensing of CuO nanostructures, synthesized by an assisted solvothermal wet chemical route.* Physica B: Condensed Matter, 406(2011) 144-149.

[219] Purusottam, B., K. Sivajee-Ganesh, K. Jayanth-Babu, O. Hussain, and C. Julien, *Microstructure and supercapacitive properties of rf-sputtered copper oxide thin films: influence of O 2/Ar ratio.* Ionics, 2015. **21**(8): p. 2319-2328.

[220] Wang, W., L. Wang, H. Shi, and Y. Liang, *A room temperature chemical route for large scale synthesis of sub-15 nm ultralong CuO nanowires with strong size effect and enhanced photocatalytic activity.* CrystEngComm, 2012. **14**(18): p. 5914-5922.

[221] Xu, J., W. Ji, Z. Shen, W. Li, S. Tang, X. Ye, D. Jia, and X. Xin, *Raman spectra of CuO nanocrystals.* Journal of Raman spectroscopy, 1999. **30**(5): p. 413-415.

[222] Debbichi, L., M. Marco de Lucas, J. Pierson, and P. Kruger, *Vibrational properties of CuO and Cu4O3 from first-principles calculations, and Raman and infrared spectroscopy.* The Journal of Physical Chemistry C, 2012. **116**(18): p. 10232-10237.

[223] Shih, P.-H., C.-L. Cheng, and S.Y. Wu, *Short-range spin-phonon coupling in in-plane CuO nanowires: a low-temperature Raman investigation.* Nanoscale research letters, 2013. **8**(1): p. 1-6.

[224] Zoolfakar, A.S., R.A. Rani, A.J. Morfa, A.P. O'Mullane, and K. Kalantar-Zadeh, *Nanostructured copper oxide semiconductors: a perspective on materials, synthesis methods and applications.* journal of materials chemistry c, 2014. **2**(27): p. 5247-5270.

[225] Senthuran, S., S. Suresh, and S. Paul Raj, *Nanostructured CuO Thin Films Prepared through Sputtering for Solar Selective Absorbers.* Journal of Solar Energy, 2013. **2013**: p. 1-6.

[226] Zhang, X., Y.-G. Guo, W.-M. Liu, and J.-C. Hao, *CuO three-dimensional flowerlike nanostructures: Controlled synthesis and characterization.* Journal of Applied Physics, 2008. **103**(11): p. 114304.

[227] Lin, C.-C. and J.-S. Liao, *Production of CuO nanoparticles using a simple precipitation method in a rotating packed bed with blade packings.* Journal of Alloys and Compounds, 2019. **775**: p. 419-426.

[228] Li, X. and C. Wang, *Engineering nanostructured anodes via electrostatic spray deposition for high performance lithium ion battery application.* Journal of Materials Chemistry A, 2013. **1**(2): p. 165-182.

[229] Li, J., Y. Zhang, L. Li, Y. Wang, L. Zhang, B. Zhang, and F. Wang, *Formation of dumbbell and sphere-like CuO as high-performance anode materials for lithium ion batteries.* Materials Letters, 2020. **261**: p. 127058.

[230] Liu, Y., L. Xiong, P. Li, H. Fu, Z. Hou, L. Zhu, and W. Li, *Self-supported CuO nanoflake arrays on nanoporous Cu substrate as high-performance negative-electrodes for lithium-ion batteries.* Journal of Power Sources, 2019. **428**: p. 20-26.

[231] Zhang, Y., L. Feng, H. Chen, W. Zhang, B. Liu, S. Ji, Y. Chuan, and R. Wang, *CuO@ Ag core-shell material preparation and as high-stability anodes for lithium-ion batteries.* Powder Technology, 2019. **355**: p. 386-392.

[232] Ji, D., H. Zhou, Y. Tong, J. Wang, M. Zhu, T. Chen, and A. Yuan, *Facile fabrication of MOF-derived octahedral CuO wrapped 3D graphene network as binder-free anode for high performance lithium-ion batteries.* Chemical Engineering Journal, 2017. **313**: p. 1623-1632

[233] Fu, Q., X. Tang, B. Huang, T. Hu, L. Tan, L. Chen, and Y. Chen, *Recent progress on the long-term stability of perovskite solar cells.* Advanced Science, 2018. **5**(5): p. 1700387.

[234] Ge, J., C.R. Grice, and Y. Yan, *Cu-based quaternary chalcogenide Cu 2 BaSnS 4 thin films acting as hole transport layers in inverted perovskite CH 3 NH 3 PbI 3 solar cells.* Journal of Materials Chemistry A, 2017. **5**(6): p. 2920-2928.

[235] Sun, W., Y. Li, S. Ye, H. Rao, W. Yan, H. Peng, Y. Li, Z. Liu, S. Wang, and Z. Chen, *High-performance inverted planar heterojunction perovskite solar cells based on a solution-processed CuO x hole transport layer.* Nanoscale, 2016. **8**(20): p. 10806-10813.

[236] Kim, H.-M., J. Kim, S.-Y. Cho, and J. Jang, *Solution-processed metal-oxide p–n charge generation junction for high-performance inverted quantum-dot light-emitting diodes.* ACS applied materials & interfaces, 2017. **9**(44): p. 38678-38686.

[237] Shirota, Y. and H. Kageyama, *Charge carrier transporting molecular materials and their applications in devices.* Chemical reviews, 2007. **107**(4): p. 953-1010.

[238] Jesuraj, P.J., H. Hafeez, S.H. Rhee, D.H. Kim, J.C. Lee, W.H. Lee, D.K. Choi, A. Song, K.-B. Chung, and M. Song, *Enhanced device efficiency in organic light-emitting diodes by dual oxide buffer layer.* Organic Electronics, 2018. **56**: p. 254-259.

[239] Chen, Z. and Z.-b. Deng, *High efficiency organic light-emitting diodes using CuO x/Cu dual buffer layers.* Optoelectronics Letters, 2015. **11**(3): p. 187-190.

[240] He, D., S. Xing, B. Sun, H. Cai, H. Suo, and C. Zhao, *Design and construction of three-dimensional flower-like CuO hierarchical nanostructures on copper foam for high performance supercapacitor.* Electrochimica Acta, 2016. **210**: p. 639-645.

[241] Wang, X., D.-M. Tang, H. Li, W. Yi, T. Zhai, Y. Bando, and D. Golberg, *Revealing the conversion mechanism of CuO nanowires during lithiation–delithiation by in situ transmission electron microscopy.* Chemical Communications, 2012. **48**(40): p. 4812-4814.

[242] Tiwari, J.N., R.N. Tiwari, and K.S. Kim, *Zero-dimensional, one-dimensional, two-dimensional and three-dimensional nanostructured materials for advanced electrochemical energy devices.* Progress in Materials Science, 2012. **57**(4): p. 724-803.

[243] Chen, J., H.-Y. Xu, J.-H. Ruan, Y.-M. Xin, Y. Li, D.-C. Li, A.-G. Wang, and D.-S. Sun, *Preparation and electro-chemical performance of binder free sodium-vanadium-bronze thin film electrode at low temperature liquid phase deposition methods.* Materials Chemistry and Physics, 249(2020) 122935.

[244] Zhang, Y., M.K. Ram, E.K. Stefanakos, and D.Y. Goswami, *Synthesis, characterization, and applications of ZnO nanowires.* Nanomaterials, 2012. **2012**.

[245] Wang, Z., S. Zhao, S. Zhu, Y. Sun, and M. Fang, *Photocatalytic synthesis of M/Cu 2 O (M= Ag, Au) heterogeneous nanocrystals and their photocatalytic properties.* CrystEngComm, 2011. **13**(7): p. 2262-2267.

[246] Heng, Z.W., W.C. Chong, Y.L. Pang, and C.H. Koo, *An overview of the recent advances of carbon quantum dots on metal oxides in theapplication of heterogeneous photocatalytic in photo-degradation of pollutants towards visiblelight and solarenergy exploitations.* Environmental Chemical Engineering (2021) 105199.

[247] Sun, S., X. Zhang, J. Zhang, L. Wang, X. Song, and Z. Yang, *Surfactant-free CuO mesocrystals with controllable dimensions: green ordered-aggregation-driven synthesis, formation mechanism and their photochemical performances.* CrystEngComm, 2013. **15**(5): p. 867-877.

[248] Rashad, M., M. Rüsing, G. Berth, K. Lischka, and A. Pawlis, *CuO and Co3O4 nanoparticles: synthesis, characterizations, and Raman spectroscopy.* Journal of Nanomaterials, 2013. **2013**.

[249] Song, S., J. Tu, L. Xu, X. Xu, Z. He, J. Qiu, J. Ni, and J. Chen, *Preparation of a titanium dioxide photocatalyst codoped with cerium and iodine and its performance in the degradation of oxalic acid.* Chemosphere, 2008. **73**(9): p. 1401-1406.

[250] Show, B., S.F. Ahmed, A. Mondal, and N. Mukherjee, *Hierarchical copper oxide as efficient enzymeless amperometric biosensor and promising photocatalyst.* Journal of Environmental Chemical Engineering, 2021. **9**(2): p. 104748.

[251] Yang, D., X. Zhao, Y. Liu, J. Li, H. Liu, X. Hu, Z. Li, J. Zhang, J. Guo, and Y. Chen, *Enhanced thermal stability of solar selective absorber based on nano-multilayered AlCrSiO films.* Solar Energy Materials and Solar Cells, 2020. **207**: p. 110331.

[252] Shehayeb, S., X. Deschanels, J. Lautru, L. Ghannam, M. Odorico, I. Karamé, and G. Toquer, *Thin polymeric CuO film from EPD designed for low temperature photothermal absorbers.* Electrochimica Acta, 2019. **305**: p. 295-303.

[253] Vázquez-Vargas, D., P. Amézaga-Madrid, L. Jáuregui-Martínez, O. Esquivel-Pereyra, W. Antúnez-Flores, P. Pizá-Ruiz, and M. Miki-Yoshida, *Synthesis and microstructural characterization of cupric oxide and cobalt oxide nanostructures for their application as selective solar coatings.* Thin Solid Films, 2020. **706**: p. 138046.

[254] Márquez, A., G. Blanco, M.F. De Rapp, D. Lamas, and R. Tarulla, *Properties of cupric oxide coatings prepared by cathodic arc deposition.* Surface and Coatings Technology, 2004. **187**(2-3): p. 154-160.

[255] Shehayeb, S., *Electrophoretic deposition of nanoparticles for controlled optical properties*. 2017, Université Montpellier.

[256] Umar, A., A.A. Ibrahim, H. Ammar, U.T. Nakate, H.B. Albargi, and Y. Hahn, *Urchin like CuO hollow microspheres for selective high response ethanol sensor application: Experimental and theoretical studies.* Ceramics International, 2021. **47**(9): p. 12084-12095.

[257] Zoolfakar, A.S., M.Z. Ahmad, R.A. Rani, J.Z. Ou, S. Balendhran, S. Zhuiykov, K. Latham, W. Wlodarski, and K. Kalantar-Zadeh, *Nanostructured copper oxides as ethanol vapour sensors.* Sensors and Actuators B: Chemical, 2013. **185**: p. 620-627.

[258] Kim, Y.-S., I.-S. Hwang, S.-J. Kim, C.-Y. Lee, and J.-H. Lee, *CuO nanowire gas sensors for air quality control in automotive cabin.* Sensors and Actuators B: Chemical, 2008. **135**(1): p. 298-303.

[259] Ali, F.I., S.T. Mahmoud, F. Awwad, Y.E. Greish, and A.F. Abu-Hani, *Low power consumption and fast response H2S gas sensor based on a chitosan-CuO hybrid nanocomposite thin film.* Carbohydrate polymers, 2020. **236**: p. 116064.

[260] Poizot, P., C.-J. Hung, M.P. Nikiforov, E.W. Bohannan, and J.A. Switzer, *An electrochemical method for CuO thin film deposition from aqueous solution.* Electrochemical and solid state letters, 2002. **6**(2): p. C21.

[261] Wang, Y., T. Jiang, D. Meng, H. Jin, and M. Yu, *Controllable fabrication of nanowire-like CuO film by anodization and its properties.* Applied Surface Science, 2015. **349**: p. 636-643

[262] Emin, S., F. Abdi, M. Fanetti, W. Peng, W. Smith, K. Sivula, B. Dam, and M. Valant, *A novel approach for the preparation of textured CuO thin films from electrodeposited CuCl and CuBr.* Journal of Electroanalytical Chemistry, 2014. **717**: p. 243-249.

[263] Wang, Y., T. Jiang, D. Meng, J. Yang, Y. Li, Q. Ma, and J. Han, *Fabrication of nanostructured CuO films by electrodeposition and their photocatalytic properties.* Applied surface science, 2014. **317**: p. 414-421.

[264] Kim, S.H., A. Umar, and S.-W. Hwang, *Rose-like CuO nanostructures for highly sensitive glucose chemical sensor application.* Ceramics International, 2015. **41**(8): p. 9468-9475.

[265] Verma, N. and N. Kumar, *Synthesis and biomedical applications of copper oxide nanoparticles: an expanding horizon.* ACS Biomaterials Science & Engineering, 2019. **5**(3): p. 1170-1188.

[266] Grigore, M.E., E.R. Biscu, A.M. Holban, M.C. Gestal, and A.M. Grumezescu, *Methods of synthesis, properties and biomedical applications of CuO nanoparticles.* Pharmaceuticals, 2016. **9**(4): p. 75.

[267] Goyal, R., L.K. Macri, H.M. Kaplan, and J. Kohn, *Nanoparticles and nanofibers for topical drug delivery.* Journal of Controlled Release, 2016. **240**: p. 77-92.

[268] Rehana, D., D. Mahendiran, R.S. Kumar, and A.K. Rahiman, *Evaluation of antioxidant and anticancer activity of copper oxide nanoparticles synthesized using medicinally important plant extracts.* Biomedicine & Pharmacotherapy, 2017. **89**: p. 1067-1077.

[269] Sharmila, G., R.S. Pradeep, K. Sandiya, S. Santhiya, C. Muthukumaran, J. Jeyanthi, N.M. Kumar, and M. Thirumarimurugan, *Biogenic synthesis of CuO nanoparticles using Bauhinia tomentosa leaves extract: characterization and its antibacterial application.* Journal of Molecular Structure, 2018. **1165**: p. 288-292.

[270] Ayodhya, D. and G. Veerabhadram, *Green synthesis of garlic extract stabilized Ag@ CeO2 composites for photocatalytic and sonocatalytic degradation of mixed dyes and antimicrobial studies.* Journal of Molecular Structure, 2020. **1205**: p. 127611.

[271] Titus, D., E.J.J. Samuel, and S.M. Roopan, *Nanoparticle characterization techniques*, in *Green synthesis, characterization and applications of nanoparticles*. 2019, Elsevier. p. 303-319.

[272] Kumar, P.S., K.G. Pavithra, and M. Naushad, *Characterization techniques for nanomaterials*, in *Nanomaterials for solar cell applications*. 2019, Elsevier. p. 97-124.

[273] Vernon-Parry, K., *Scanning electron microscopy: an introduction.* III-Vs Review, 2000. **13**(4): p. 40-44.

[274] Tararam, R., P.S. Garcia, D.K. Deda, J.A. Varela, and F. de Lima Leite, *Atomic force microscopy: A powerful tool for electrical characterization*, in *Nanocharacterization techniques*. 2017, Elsevier. p. 37-64.

[275] Mourdikoudis, S., R.M. Pallares, and N.T. Thanh, *Characterization techniques for nanoparticles: comparison and complementarity upon studying nanoparticle properties.* Nanoscale, 2018. **10**(27): p. 12871-12934.

[276] Bréchignac, C., P. Houdy, and M. Lahmani, *Nanomaterials and nanochemistry*. 2008: Springer Science & Business Media.

[277] Dai, J., X. Wang, and G. Yuan. *Fourier transform spectrometer for spectral emissivity measurement in the temperature range between 60 and 1500° C*. in *Journal of Physics: Conference Series*. 2005. IOP Publishing.

[278] Theocharous, E., J. Ishii, and N.P. Fox, *Absolute linearity measurements on HgCdTe detectors in the infrared region.* Applied Optics, 2004. **43**(21): p. 4182-4188.

[279] Yuan, Z., J. Zhang, J. Zhao, Y. Liang, and Y. Duan, *Linearity study of a spectral emissivity measurement facility.* International Journal of Thermophysics, 2009. **30**(1): p. 227-235.

[280] Ren, D., H. Tan, Y. Xuan, Y. Han, and Q. Li, *Apparatus for measuring spectral emissivity of solid materials at elevated temperatures.* International Journal of Thermophysics, 2016. **37**(5): p. 51.

[281] Yuan, Z., T. Wang, X. Lu, W. Dong, C. Bai, X. Hao, and Y. Duan, *T 90 Measurement of Co-C, Pt-C, and Re-C High-Temperature Fixed Points at the NIM.* International Journal of Thermophysics, 2011. **32**(7-8): p. 1744.

[282] Song, X., W. Dong, Z. Yuan, X. Lu, Z. Li, and Q. Duanmu, *Investigation of the linearity of the NIM IR infrared spectral emissivity measurement facility by means of flux superposition method.* Infrared Physics & Technology, 2020. **109**: p. 103416.

[283] Basavaraju, U., H.C. Barshilia, and B. Basu, *On the origin of spectrally selective high solar absorptance of TiB2-based tandem absorber with double layer antireflection coatings.* Solar Energy Materials and Solar Cells, 2021. **220**: p. 110839.

[284] Lu, X., X. Luo, J. Zhang, S.Y. Quek, and Q. Xiong, *Lattice vibrations and Raman scattering in two-dimensional layered materials beyond graphene.* Nano Research, 2016. **9**(12): p. 3559-3597.

[285] Chirayil, C.J., J. Abraham, R.K. Mishra, S.C. George, and S. Thomas, *Instrumental techniques for the characterization of nanoparticles*, in *Thermal and Rheological Measurement Techniques for Nanomaterials Characterization*. 2017, Elsevier. p. 1-36.

[286] Adeoye, A.E., E. Ajenifuja, B.A. Taleatu, and A. Fasasi, *Rutherford backscattering spectrometry analysis and structural properties of thin films deposited by chemical spray pyrolysis.* Journal of Materials, 2015. **2015**.

[287] Fluch, U., V. Paneta, D. Primetzhofer, and S. Ott, *Uniform distribution of post-synthetic linker exchange in metal–organic frameworks revealed by Rutherford backscattering spectrometry.* Chemical Communications, 2017. **53**(48): p. 6516-6519.

[288] Mtshali, C., Z. Khumalo, G. Mocumi, K. Lebesana, N. Kheswa, S. Magogodi, F. Cummings, C. Pieters, and M. Nkosi, *Effects of argon thermal-annealing on microstructural and formation of Silicon-Titanium-Cobalt thin films.* Nuclear Instruments and Method in Physics B:, 445(2019) 18-25.

[289] Ohara, S., T. Adschiri, T. Ida, M. Yashima, T. Mikayama, H. Abe, Y. Setsuhara, K. Nogi, M. Miyahara, and K. Kaneko, *Characterization Methods for Nanostructure of Materials*, in *Nanoparticle Technology Handbook*. 2008, Elsevier. p. 267-315.

[290] Gajbhiye, M., J. Kesharwani, A. Ingle, A. Gade, and M. Rai, *Fungus mediated synthesis of silver nanoparticles and their activity against pathogenic fungi in combination with fluconazole.* Nanomedicine: Nanotechnology, Biology and Medicine, 2009. **5**(4): p. 382-386.

[291] Menon, S., H. Agarwal, S.V. Kumar, and S. Rajeshkumar, *Biomemetic synthesis of selenium nanoparticles and its biomedical applications*, in *Green Synthesis, Characterization and Applications of Nanoparticles*. 2019, Elsevier. p. 165-197.

[292] Ke, C., X. Zhang, W. Guo, Y. Li, D. Gong, and X. Cheng, *Solar selective coatings with multilayered structure based on thermal spraying WC-Co solar absorption layer.* Vacuum, 2018. **152**: p. 114-122.

[293] Öztas, M. and M. Bedir, *Thickness dependence of structural, electrical and optical properties of sprayed ZnO: Cu films.* Thin Solid Films, 2008. **516**(8): p. 1703-1709.

[294] Peng, W., L. Li, S. Yu, H. Zheng, and P. Yang, *Structure, binding energy and optoelectrical properties of p-type CuI thin films: The effects of thickness.* Applied Surface Science, 2020. **502**: p. 144424.

[295] Sakulaue, P., A.Y.Y. Swe, K. Benchaprathanphorn, T. Lertvanithphol, and K. Viravaidya-Pasuwat, *Improving cell detachment from temperature responsive poly (N-isopropylacrylamide-co-acrylamide) grafted culture surface by spin coatings.* American chemical society, (2018)b18181-18188.

[296] Mellbring, O., S. Kihlman Øiseth, A. Krozer, J. Lausmaa, and T. Hjertberg, *Spin coating and characterization of thin high-density polyethylene films.* Macromolecules, 2001. **34**(21): p. 7496-7503.

[297] Pang, X., F. Zhou, B. Li, J. Jiang, and J. Zhou, *Optical thermostability and weatherability of TiN/TiC-Ni/Mo cermet based spectral selective absorbing coatings by laser cladding.* Optical Materials, 2021. **117**: p. 111195.

[298] El Aakib, H., J. Pierson, L. Atourki, L. Nkhaili, A. El Kissani, A. Narjis, and A. Outzourhit, *Preparation and characterization of nanocomposites of Co/CuO by RS sputtering for solar selective absorber applications.* Thin solid films, 709(2020) 138199.

[299] Jana, S., S. Das, N. Das, and K. Chattopadhyay, *CuO nanostructures on copper foil by a simple wet chemical route at room temperature.* Materials Research Bulletin, 45(2010) 693-698.

[300] Thomas, T., K.R. Kumar, C.S. Kartha, and K. Vijayakumar. *Simple one step spray process for CuInS 2/In 2 S 3 heterojunction on flexible substrates for photovoltaic application*. Optics and Photonics, V*II*(2015) 2015.

[301] Kumar P., P. Kollu, R. Kalyani, U. Shameem, and S. Pammi, *Green synthesis of CuO nanoparticles using Aloe vera leaf extracts and its antibacterial activities against fish bacterial pathogens.* BioNanoScience, 5(2015) 135-139.

[302] Gunalan, S., R. Sivaraj, and R. Venckatesh, *Aloe barbadensis Miller mediated green synthesis of mono-disperse copper oxide nanoparticles: optical properties.* Spectrochimica Acta Part A: Molecular and Biomolecular Spectroscopy, 97(2012) 1140-1144.

[303] Welegergs, G., H. Gebretnisae, M. Tsegay, Z. Nuru, S. Dube, and M. Maaza, *Thickness dependent morphological, structural and optical property of SS/CuO nanocoatings as selective solar absorber.* Infrared Physics & Technology, 113(2021) 103619.

[304] Ning, Y., W. Wang, Y. Sun, Y. Wu, H. Man, C. Wang, S. Zhao, E. Tomasella, A. Bousquet, and Y. Zhang, *Tuning of reflectance transition position of Al-AlN cermet solar selective absorber coating by simulating.* Infrared Physics & Technology, 80(2017) 65-70.

[305] Shah, A.A. and M.C. Gupta, *Spectral selective surface for concentrated solar power receiver by laser sintering of tungsten micro and nano particles.* Solar energy materials and solar cells, 117(2013) 489-493.

[306] Ning, Y., W. Wang, Y. Sun, Y. Wu, Y. Liu, H. Man, M.I. Malik, C. Wang, S. Zhao, and E. Tomasella, *Effects of substrate film thickness and temperature on thermal emittance of Mo/substrate deposited by magnetron sputtering.* Vacuum, 128(2016) 73-79.

[307] Cao, J., C. Zhang, C. Li, D. Gao, X. Si, and J. Qi, *A facile method to synthesize Ag/CuO composite nanowire arrays for electrochemical detection.* Materials Letters, 288(2021) 129334.

[308] Kung, M.-L., M.-H. Tai, P.-Y. Lin, D.-C. Wu, W.-J. Wu, B.-W. Yeh, H.-S. Hung, C.-H. Kuo, Y.-W. Chen, and S.-L. Hsieh, *Silver decorated copper oxide (Ag@ CuO) nanocomposites enhances ROS-mediated bacterial architecture collapse.* Colloids and Surfaces B: Biointerfaces, 155(2017) 399-407.

[309] Nuru, Z., D. Perez, K. Kaviyarasu, A. Vantomme, and M. Maaza, *Annealing effect on the optical properties and interdiffusion of MgO/Zr/MgO multilayered selective solar absorber coatings.* Solar Energy, 120(2015) 123-130.

[310] Guo, X., D. Wang, B. Liu, Y. Zhou, and S. Li, *Quick design of high efficiency light trapping nanostructures for thin film silicon solar cells.* Optics Communications, 395(2017) 122-126.

[311] Weinstein, L.A., J. Loomis, B. Bhatia, D.M. Bierman, E.N. Wang, and G. Chen, *Concentrating solar power.* Chemical Reviews, 115(2015) 12797-12838.

[312] Fei Guo, C., T. Sun, F. Cao, Q. Liu, and Z. Ren, *Metallic nanostructures for light trapping in energy-harvesting devices.* Light: Science & Applications, 3(2014)161-161.

[313] Kondaiah, P., K. Niranjan, S. John, and H.C. Barshilia, *Tantalum carbide based spectrally selective coatings for solar thermal absorber applications.* Solar Energy Materials and Solar Cells, 198(2019) 26-34.

[314] Cao, F., D. Kraemer, T. Sun, Y. Lan, G. Chen, and Z. Ren, *Enhanced Thermal Stability of W-Ni-Al2O3 Cermet Based Spectrally Selective Solar Absorber with tungsten Infrared Reflector.* 2014.

[315] Wang, C., W. Li, Z. Li, and B. Fang, *Solar thermal harvesting based on self-doped nanocermet: Structural merits, design strategies and applications.* Renewable and Sustainable Energy Reviews, 134(2020) 110277.

[316] Mallik, A. and B. Ray, *Evolution of principle and practice of electro-deposited thin film: A review on effect of temperature, and sonication.* Electro-chemistry, 2011(**2011**).

[317] Tarditi, A., M. Bosko, and L. Cornaglia, *Electroless Plating of Pd Binary and Ternary Alloys and Surface Characteristics for Application in Hydrogen Separation.* 2017.

[318] Zheng, J., H. Chen, W. Cai, L. Qiao, Y. Ying, W. Li, J. Yu, L. Jiang, and S. Che, *Reaction mechanisms of copper electrodeposition from 1-hydroxyethylidene-1, 1-diphosphonic acid (HEDP) solution on glassy carbon.* Materials Science and Engineering: B, 224(2017) 18-27.

[319] Gao, M., C. Yang, Q. Zhang, Y. Yu, Y. Hua, Y. Li, and P. Dong, *Electrochemical fabrication of porous Ni-Cu alloy nanosheets with high catalytic activity for hydrogen evolution.* Electrochimica Acta, 215(2016) 609-616.

[320] Eugénio, S., T. Silva, M. Carmezim, R. Duarte, and M. Montemor, *Electrodeposition and characterization of nickel–copper metallic foams for application as electrodes for supercapacitors.* Journal of Applied Electrochemistry, 44(2014) 455-465.

[321] Majidi, M., K. Asadpour-Zeynali, and B. Hafezi, *Reaction and nucleation mechanisms of copper electrodeposition on disposable pencil graphite electrode.* Electrochimica Acta, 54(2009) 1119-1126.

[322] Yu, J., G. Liu, A. Liu, Y. Meng, B. Shin, and F. Shan, *Solution-processed p-type copper oxide thin-film transistors fabricated by using a one-step vacuum annealing technique.* Journal of Materials Chemistry C, 3(2015) 9509-9513.

[323] Afzal, N., M. Devarajan, and K. Ibrahim, *Effect of film thickness on the surface, structural and electrical properties of InAlN films prepared by reactive co-sputtering.* Materials Science in Semiconductor Processing, 43(2016) 96-103.

[324] Pal, S., D. Diso, S. Franza, A. Licciulli, and L. Rizzo, *Spectrally selective absorber coating from transition metal complex for efficient photothermal conversion.* Journal of materials science, 48(2013) 8268-8276.

[325] Fang, L., J. Liu, S. Ju, F. Zheng, W. Dong, and M. Shen, *Experimental and theoretical evidence of enhanced ferromagnetism in sonochemical synthesized BiFeO3 NPs.* Applied Physics Letters, 97(2010) 242501.

[326] Siddiqui, H., M. Qureshi, and F.Z. Haque, *Valuation of copper oxide (CuO) nanoflakes for its suitability as an absorbing material in solar cells fabrication.* Optik, 127(2016) 3713-3717.

[327] Akgul, F.A., G. Akgul, N. Yildirim, H.E. Unalan, and R. Turan, *Influence of thermal annealing on microstructural, morphological, optical properties and surface electronic structure of copper oxide thin films.* Materials Chemistry and Physics, 147(2014) 987-995.

[328] Purusottam-Reddy, B., K. Sivajee-Ganesh, K. Jayanth-Babu, O. Hussain, and C. Julien, *Microstructure and supercapacitive properties of rf-sputtered copper oxide thin films: influence of O2/Ar ratio.* Ionics, 21(2015) 2319-2328.

[329] Arfan, M., D.N. Siddiqui, T. Shahid, Z. Iqbal, Y. Majeed, I. Akram, Noreen, R. Bagheri, Z. Song, and A. Zeb, *Tailoring of nanostructures: Al doped CuO synthesized by composite-hydroxide-mediated approach.* Results in Physics, 13(2019) 102187.

[330] George, P. and P. Chowdhury, *Complex dielectric transformation of UV-vis diffuse reflectance spectra for estimating optical band-gap energies and materials classification.* Analyst, 144(2019) 3005-3012.

[331] López, R. and R. Gómez, *Band-gap energy estimation from diffuse reflectance measurements on sol–gel and commercial TiO2: a comparative study.* Journal of sol-gel science and technology, 61(2012) 1-7.

[332] Bouzidi, A., I.S. Yahia, W. Jilani, S.M. El-Bashir, S. AlFaify, H. Algarni, and H. Guermazi, *Electronic-conduction mechanisms and optical spectroscopy of Indigo carmine as novel organic semiconductor.* Optical and Quantum Electronics, 50(2018).

[333] Chen, Z., Q. Dong, Y. Liu, C. Bao, Y. Fang, Y. Lin, S. Tang, Q. Wang, X. Xiao, and Y. Bai, *Thin single crystal perovskite solar cells to harvest below band-gap light absorptions.* Nature communications, 8(2017) 1-7.

[334] Gülen, Y., F. Bayansal, B. Şahin, H.A. Çetinkara, and H.S. Güder, *Fabrication and characterization of Mn-doped CuO thin films by the SILAR method.* Ceramics International, 39(2013) 6475-6480.

[335] McClure, E.T., M.R. Ball, W. Windl, and P.M. Woodward, *Cs2AgBiX6 (X= Br, Cl): new visible light absorbing, lead-free halide perovskite semiconductors.* Chemistry of Materials, 28(2016) 1348-1354.

[336] Kulbak, M., D. Cahen, and G. Hodes, *How important is the organic part of lead halide perovskite photovoltaic cells? Efficient CsPbBr3 cells.* The journal of physical chemistry letters, 6(2015) 2452-2456.

[337] Park, J.Y., T.H. Kwon, S.W. Koh, and Y.C. Kang, *Annealing Temperature Dependence on the Physicochemical Properties of Copper Oxide Thin Films.* Bulletin of the Korean Chemical Society, 32(2011) 1331-1335.

[338] Wender, H., P. Migowski, A.F. Feil, S.R. Teixeira, and J. Dupont, *Sputtering deposition of nanoparticles onto liquid substrates: Recent advances and future trends.* Coordination Chemistry Reviews, 257(2013) 2468-2483.

[339] Maurya, D., A. Sardarinejad, and K. Alameh, *Recent developments in RF Magnetron sputtered thin films for pH sensing applications—an overview.* Coatings, 4(2014) 756-771.

[340] Prabaswara, A., J. Birch, M. Junaid, E.A. Serban, L. Hultman, and C.-L. Hsiao, *Review of GaN thin film and nanorod growth using magnetron sputter epitaxy.* Applied Sciences, 10(2020) 3050.

[341] Karthick Kumar, S., S. Murugesan, and S. Suresh, *Preparation and characterization of CuO nanostructures on copper substrate as selective solar absorbers.* Materials Chemistry and Physics, 143(2014) 1209-1214.

[342] Jana, S., S. Das, N.S. Das, and K.K. Chattopadhyay, *CuO nanostructures on copper foil by a simple wet chemical route at room temperature.* Materials Research Bulletin, 45(2010) 693-698.

[343] Zhang, X., F. Shi, J. Niu, Y. Jiang, and Z. Wang, *Superhydrophobic surfaces: from structural control to functional application.* J. Mater. Chem., 18(2008) 621-633.

[344] Kumar, S.K., S. Murugesan, and S. Suresh, *Preparation and characterization of CuO nanostructures on copper substrate as selective solar absorbers.* Materials Chemistry and Physics, 143(2014) 1209-1214.

[345] Du, G. and G. Van Tendeloo, *Cu (OH) 2 nanowires, CuO nanowires and CuO nanobelts.* Chemical Physics Letters, 393(2004) 64-69.

[346] Vázquez-Vargas, D., P. Amézaga-Madrid, L. Jáuregui-Martínez, O. Esquivel-Pereyra, W. Antúnez-Flores, P. Pizá-Ruiz, and M. Miki-Yoshida, *Synthesis and microstructural characterization of CuO and CoO nanostructures for their applications as selective solar absorber coatings.* Thin Solid Films, (2020)138046.

[347] Öztas, M., Bedir, Metin, *Thickness dependence of structural, electrical and optical properties of sprayed ZnO: Cu films.* Thin Solid Films, 516(2008) 1703-1709.

[348] Afzal, N., Mutharasu, and K. Ibrahim, *Effect of film thickness on the surface, structural and electrical properties of InAlN films prepared by reactive co-sputtering.* Materials Science in Semiconductor Processing, 43(2016) 96-103.

[349] Dan, A., K. Chattopadhyay, H.C. Barshilia, and B. Basu, *Angular solar absorptance and thermal stability of W/WAlN/WAlON/Al2O3-based solar selective absorber coating.* Applied Thermal Engineering, 109(2016) 997-1002.

[350] Valleti, K., D.M. Krishna, P.M. Reddy, and S.V. Joshi, *High temperature stable solar selective coatings by cathodic arc PVD for heat collecting elements.* Solar Energy Materials and Solar Cells, 145(2016) 447-453.

[351] Nuru, Z.Y., D.E. Motaung, K. Kaviyarasu, and M. Maaza, *Optimization and preparation of Pt– Al2O3 double cermet as selective solar absorber coatings.* Journal of Alloys and Compounds, 664(2016)161-168.

[352] Dwivedi, C., P. Bamola, B. Singh, and H. Sharma, *Infrared radiation and materials interaction: Active, passive, transparent, and opaque coatings.* 2020 33-56.

[353] Kumar, S.K., S. Murugesan, and S.P. Raj, *CuO thin films made of nanofibers for solar selective absorber applications.* Solar Energy, 94(2013) 299-304.

[354] Mandal, J., D. Wang, A.C. Overvig, N.N. Shi, D. Paley, A. Zangiabadi, Q. Cheng, K. Barmak, N. Yu, and Y. Yang, *Scalable, "Dip-and-Dry" Fabrication of a Wide-Angle Plasmonic Selective Absorber for High-Efficiency Solar-Thermal Energy Conversion.* Advanced Materials, 29(2017) 1702156.

[355] Dan, A. and B. Basu, *Understanding spectrally selective properties of solar absorbers.* 2020 133-151.

[356] López, R. and R. Gómez, *Band-gap energy estimation from diffuse reflectance measurements on sol–gel and commercial TiO2: a comparative study.* Journal of Sol-Gel Science and Technology, 61(2011) 1-7.